AN EXPERIMENTAL INVESTIGATION ON THE STATIC EQUILIBRIA AND DYNAMICS OF LIQUID BRIDGES

by

ANDREW HOWARD RESNICK

A DISSERTATION

Submitted in partial fulfillment of the requirements
for the degree of Doctor of Philosophy in
The Department of Physics
of
The School of Graduate Studies
of
The University of Alabama in Huntsville

HUNTSVILLE, ALABAMA

1997

DISSERTATION APPROVAL FORM

Submitted by Andrew H. Resnick in partial fulfillment of the requirements for the degree of Doctor of Philosophy with a major in Physics.

Accepted on behalf of the Faculty of the School of Graduate Studies by the Dissertation committee:

_____Committee Chair

(Date)

_____

_____

_____

_____

_____

_____ Department Chair

_____ College Dean

_____ Graduate Dean

ABSTRACT

School of Graduate Studies

The University of Alabama in Huntsville

Degree Ph. D. College/Dept Science/Physics

Name of Candidate Andrew Howard Resnick

Title: An Experimental Investigation of the Static Equilibria and Dynamics of Liquid Bridges

A liquid bridge is a volume of liquid held between two or more solid supports. In the case of small disk supports with a sharp edge, the contact line between the bridge and the support disk will be anchored along the edge of the disk. For these cases the solid presents a geometrical singularity and the contact angle is indeterminate within a given range. This dissertation presents research conducted on liquid bridges with anchored contact lines. The three major topics covered are: determining the role of support geometry on static equilibria, liquid bridge dynamical behavior, and forces exterted by a liquid bridge on a support structure. The work was primarily experimental and conducted in a "Plateau tank" that allowed for the simulation of equivalent low-gravity conditions. The main thrust of the experimental work involved the use of a high resolution optical measurement system for imaging the dynamic zone shape, measurement of the static and dynamic contact angles and non-invasive analysis of excited surface modes. The liquid bridge was manipulated by computer controlled linear actuators which allowed precise control over the physical characteristics of the bridge.

Experiments have been carried out to locate a bifurcation point along the maximum volume axisymmetric stability margin. Below the critical slenderness the bifurcation from an axisymmetric to a stable nonaxisymmetric configuration is supercritical. However, above this critical slenderness, the bifurcation is subcritical.

A series of experiments analyzed the effect on axisymmetric bridge stability by using support disks of different radii. The shape behavior as transition points were approached, as well as the limiting case of a vanishing support radius was investigated.

Experiments were performed to determine the resonant frequencies of axisymmetric bridges subject to lateral vibrations. Anomolous results led to a series of experiments to characterize nonlinearities present in the dynamic bridge shape.

Finally, an attempt was made to experimentally measure the force exerted by the bridge on the lower support disk. This was done through use of a force balance apparatus. Particular attention was paid to the behavior of the bridge as the minimum volume stability limit was approached.

Abstract Approval: Committee Chair _____

(Date)

Department Chair _____

Graduate Dean _____

TABLE OF CONTENTS

LIST OF FIGURES

LIST OF TABLES

LIST OF SYMBOLS

Symbol	Definition
Dimensionless Numbers:	
Bo	Bond number
$Bo_{max}(K)$	Maximum Bo such that there exists stable axisymmetric bridges
Ca	Capillary number
ε	Relative disk offset
K	Ratio of disk radii
Λ	Slenderness
Λ_c, V_c	Critical slenderness, volume
Λ_f, V_f	Final slenderness, volume
Λ_i, V_i	Initial slenderness, volume
Λ_{max}, V_{max}	Maximum slenderness, volume
Oh	Ohnesorge number
Re	Reynolds number
V	Relative volume
δV	Volume increment
We	Weber number
ξ	Dimensionless surface deformation
Ξ	Ratio of disk rotation rates

Contact Angles, Interfacial Energies:

a	Inner length scale (microscopic)
β_1	Contact angle (external) at lower disk support
β_2	Contact angle (external) at upper disk support
δ	Internal angle at a solid edge
f	Correction factor for hanging/pendant drops
L_s	Slip length
$l_i(\phi)$	Slip model-dependent function
ϕ_1	Contact angle (internal) at lower disk support
ϕ_2	Contact angle (internal) at upper disk support
ϕ	True contact angle
ϕ_a	Advancing contact angle
ϕ_C	Cassie contact angle
ϕ_W	Wenzel contact angle
ϕ_r	Receding contact angle
ϕ_e	Contact angle that satisfies Young's Equation
γ_l	Surface free energy of a liquid
γ_{lv}	Interfacial energy between a liquid and a vapor
γ_s	Surface free energy of a solid
γ_{sl}	Interfacial energy between a solid and a liquid
γ_{sv}	Interfacial energy between a solid and a vapor
γ	Interfacial energy
π_{lv}	Film pressure between a liquid and a vapor
π_{sl}	Film pressure between a solid and a liquid
π_{sv}	Film pressure between a solid and a vapor
Ω	Slip parameter

Mathematical Formalism:

$\frac{Dy}{Dx}$; $y_{\|x}$	Material derivative of y with respect to x
$\frac{\partial y}{\partial x}$; $y_{,x}$	Partial derivative of y with respect to x
$\langle x,y \rangle$	Inner product of x and y
[x]	Jump in quantity "x" across a surface of discontinuity
$\otimes$	Exterior product
∇	Gradient operator ("nabla")
∇_2, ∇_2^*	Surface gradient operators
Γ^i_{jk}	Cristoffel coefficients of the first kind
δ_{ij}	Kronecker delta
$\mathbf{E}^n$	Euclidean space in n dimensions
$\mathbf{e}_i$	Unit vectors
ε	Perturbation amplitude
Γ	Simple curve in $\Re^2$
g^{ij}, g_{ij}	Metric tensor
$\mathbf{I}$	Identity tensor
J	Jacobian
$\Re$	Real numbers
$\Re^2$	Space formed by $\Re \otimes \Re$
$\Re^2 \setminus \Gamma$	Complement of Γ in $\Re^2$
ω^i	Unit 1-forms
$\mathbf{X}$	Configuration vector

Differential Geometry:

$F(r,\theta,z,t)$	Liquid bridge surface $F = r - f(\theta,z,t) = 0$
$f(\theta,z,t)$	Difference between liquid bridge surface and a cylinder at $r = R$
J	Mean curvature
K	Gaussian curvature
κ_g	Geodesic curvature
κ_n	Normal curvature
$\mathbf{n}$	Surface normal
Σ	Surface element
s	Arclength
τ	Torsion
Ω	Volume element

Thermodynamical and Continuum Mechanical Quantities:

C_J	Mechanical bending moment for mean curvature
C_K	Mechanical bending moment for Gaussian curvature
C_{nj}	Mechanical bending moment for normal curvature
C_{gj}	Mechanical bending moment for geodesic curvature
$C_{\tau j}$	Mechanical bending moment for torsion
$C_{\phi jj'}$	Mechanical bending moment for three-phase contact line
$C_{\varphi ll'}$	Mechanical bending moment for vertex angle of two contact lines
d_{ij}	Rate-of-deformation tensor
ε	Energy density
E	Energy
E_Σ	Energy of a surface

h	Heat density
$\mathbf{j}$	Flux density
K	Kinetic energy
λ	Dilatational viscosity
M	Mechanical power
μ	Shear viscosity
μ_i	Chemical potential of phase "i"
M_i	Mass of phase "i"
Π	Thermodynamic pressure
p	Mean pressure
Q	Heat energy
ρ	Density
S	Entropy
σ	Line tension
$\mathbf{T}$	Surface traction
$\mathbf{t}_\theta$	Tangential stress in the θ-direction
$\mathbf{t}_z$	Tangential stress in the z-direction
U	Potential energy
u	Potential energy density
$U^{(\ell)}$, $S^{(\ell)}$, $\rho^{(\ell)}$	Potential energy, Entropy, Mass density on a line ℓ
$U^{(\Sigma)}$, $S^{(\Sigma)}$, $\rho^{(\Sigma)}$	Potential energy, Entropy, Mass density on a surface Σ
$U^{(\Omega)}$, $S^{(\Omega)}$, $\rho^{(\Omega)}$	Potential energy, Entropy, Mass density in a volume Ω

Miscellaneous Symbols:

A	True acceleration amplitude [cm/s^2]
A_{Nm}	Amplitude of N, m mode perturbation

a	Input acceleration amplitude [arb. units]
$\beta(s)$	Angle between tangent of F and the horizontal
d	Lateral offset between disk centers
d_e	Equatorial diameter
d_s	Secondary diameter
ε	Coefficient of expansion
$\mathbf{F}$	Body force
f	Correction factor
f	Input frequency of oscillation [arb. units]
$\varphi_{01}(s)$, $\varphi_{02}(s)$, $\varphi_1(s)$,	
$D(s)$	Stability functions
F_{cap}	Capillary force exerted by a bridge upon a support
F_{hydro}	Hydrodynamic force exerted by a bridge upon a disk support
F_{tot}	Total force exerted by a bridge upon a disk support
g	Gravitational acceleration
L	Axial distance between support disks
L_c	Scaling length
L_{max}	Maximum stable distance between disk supports
m	Azimuthal wavenumber
n	Index of refraction
ν	True frequency of oscillation [Hz]
ν_j	j^{th} frequency in a FFT decomposition
N	Axial wavenumber
R	Average disk radius
R_1, R_2	Lower, upper disk radius
$\mathbf{R}$	Position vector of a particle at time "t"
σ	Perturbation eigenvalue (complex)

$\mathbf{U}$	Displacement vector (Lagrangian coordinates)
$\mathbf{u}$	Displacement vector (Eulerian coordinates)
$\mathbf{V}$	Velocity (Lagrangian coordinates)
$\mathbf{v}$, v	Velocity (Eulerian coordinates)
V_0	True volume
$\mathbf{v}_b$, p_b,$f(\theta,z,t)_b$,$\mathbf{T}_b$	Base state quantities
$\mathbf{v}_p$, p_p,$f(\theta,z,t)_p$,$\mathbf{T}_p$	Perturbed state quantities
ω_0	Inviscid eigenfrequency of a liquid bridge
ω_1	First correction to ω_0.
ω_{Nm}	Eigenfrequency of N, m mode
Ω	Average rotation rate of support disks
Ω_1,Ω_2	Rotation rate of lower, upper supprt disk
Z_{Nm}	Axial term of N, m mode perturbation
$\mathbf{r}$	Position vector of a particle at time "t_0"

Chapter 1

INTRODUCTION

1.1 Introduction and background

A liquid bridge, or captive drop, is a mass of liquid held by surface tension between two or more solid supports (see Figure 1.1). Liquid bridges occur in a variety of physical and technological situations and a great deal of theoretical and experimental work has been done to determine axisymmetric equilibria for various disk configurations, bridge slenderness and rotations.

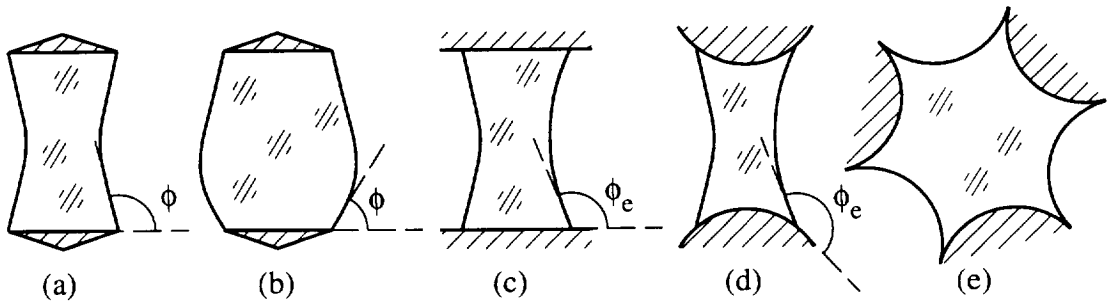

Figure 1.1. Equilibrium configurations of liquid bridges between solid supports. In (a) and (b) surfaces anchored to sharp disk edges are shown. In (c), (d), and (e) the contact angle takes on its equilibrium value ϕ_e.

There have also been numerous investigations of the dynamics of axisymmetric liquid bridges subject to different excitations (impulses, vibration, etc.). Some preliminary work has been performed on nonaxisymmetric bridge stability, forces exerted by

axisymmetric bridges, and dielectric liquid bridges. Orr *et al.* [1] cite a number of applications of the results of liquid bridge research. For example, volume is essential for calculations of water saturation [2] and connate water estimates in oil and gas reservoirs [3]. Capillary condensation and evaporation problems in porous media require knowledge of bridge curvatures [4,5]. Forces exerted by liquid bridges on solids are important in powder metallurgy during liquid phase sintering [6], in powder wetting problems [7], the deformation of moist porous and unconsolidated granular media [8,9], and in adhesion problems [10]. Liquid bridges and drops are also important factors when considering the positioning of liquid masses using surface tension forces and propellant management in liquid fuel tanks [11]. More recent applications of liquid bridges include the floating zone method of crystal growth [12-14]. Liquid bridge oscillation and decay properties can also be used for viscosity and surface tension measurements of molten materials at high temperatures [15]. Pendular liquid bridges occur widely in the powder technology industry and are a major influence on powder flow process and mechanical properties [16]. In porous media flow, liquid-liquid displacement can lead to evolution of pendant and sessile lobes or lenticular bridges. The formation of liquid bridges from the gel that coats lung micro-airways results in occlusion of the bronchioles and is a precursor to respiratory problems and lung collapse [17-19].

Although liquid bridges have many technological applications, they are also interesting from a basic science point of view. Axisymmetric bridges, essentially a one-dimensional physical system, can display a very rich and complex behavior. The experiments described in chapter 4 have been well documented previously, and were performed here primarily to test and calibrate system performance. The results of chapter 5 represent part of an ongoing study at the Center for Microgravity and Materials Research (CMMR) to analyze multiparametric stability of liquid bridges. In addition to verification of numerical calculations, a new method was found to measure the interfacial energy between isopycnic imiscible fluids, and the behavior of a bridge in the limit of a vanishing

lower disk support radius was observed. The results of experiments described in chapter 6 indicate that to properly model laterally oscillated dynamic liquid bridge behavior, a full non-linear treatment of the system is necessary. This has direct application to models of crystal growth in a g-jitter environment. In addition, a new method was used to visualize the spatial modes of an oscillating liquid bridge in real-time. Finally, the experiments described in chapter 7 shed insight into the behavior of a bridge as the minimum volume stability limit is approached. This experimental apparatus could be used to probe thin film statics and dynamics, as well as other dynamic fluid processes such as drop coalescence.

Using rigid sharp-edged disk supports, the bridge can be positioned so that the contact line between the liquid and the solid disk is anchored at the edge of the disk. For these cases where the solid presents such a geometrical singularity, the contact angle is indeterminate within a given range, and the contact line remains anchored to the edge. Supports without sharp edges, such as spheres or large flat plates, will allow the fluid to attain an equilibrium contact angle. This will persist provided the contact line does not move. However, since the contact line is not anchored, vibrations or other motion of the support can result in motion of the contact line in order to accommodate contact angle changes as the bridge deforms. Most theoretical and experimental work deals with liquid bridges with a pinned contact line. Slobozhanin and Tyuptsov [20], and later Dyson [21] showed that for a bridge anchored to a sharp edge, the contact angle ϕ can vary freely within the range $\phi_e \leq \phi \leq \phi_e + \pi - \delta$ where δ is the acute angle defined by the sharp edge (see Figure 1.2).

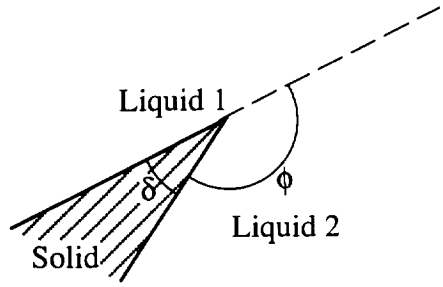

Figure 1.2. Contact angle ϕ at a sharp edge: $\phi_e < \phi < \pi - \delta + \phi_e$

This pinning or anchoring of the contact line is sometimes referred to as canthotaxis [22,23] and allows the bridge to admit a wider range of stable configurations than would be possible if the contact angle was restricted to be the equilibrium angle (as it would be for a flat or some other smooth surface). Other types of supports have been considered, including flat plates [24-29] plates and spheres [30] and spheres [16, 31-33].

The shapes and stability of liquid bridges are governed by the following dimensionless numbers (see Figure 1.3)

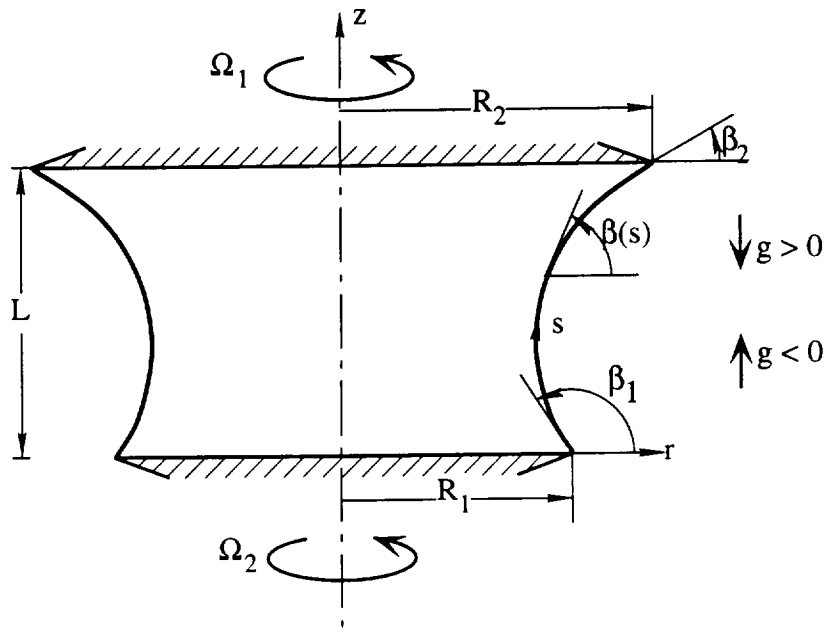

Figure 1.3. Equilibrium configuration of an axisymmetric liquid bridge. The gravity vector points toward the smaller disk if g > 0, and towards the larger disk if g < 0.

Bo	$= \Delta\rho R^2 g/\gamma$	≡ Bond number
V	$= V_0/\pi R^2 L$	≡ relative volume
Λ	$= L/2R$	≡ slenderness

We	$= \Delta\rho R^3\Omega^2/\gamma$	≡ Weber number
β_1, β_2		≡ lower and upper external contact angles
ϕ_1, ϕ_2		≡ lower and upper internal contact angles = 180 - β
K	$= R_1/R_2$	≡ ratio of disk radii
Ξ	$= \Omega_1/\Omega_2$	≡ ratio of disk rotation rates
ε	$= d/R$	≡ relative disk offset

Here $\Delta\rho$ is the density difference between the bridge and the surrounding fluid, R is the characteristic length associated with the bridge (usually the average radius of the supporting disks), g is the gravitational acceleration, γ is the surface energy or interfacial tension (see section 2.2.), L is the distance between the disks, d is the lateral offset between disk centers and Ω is the average angular rotation rate of the disks. Bo is a measure of the ratio of buoyancy to surface tension forces. The Weber number represents a balance between centripetal and surface tension forces.

For cases where the effective static and dynamic Bond numbers are small, the resulting dynamics of a bridge may differ considerably from the dynamics of bridges at large Bo. The roles of support geometry and contact angle dynamics in determining liquid bridge stability at low Bond numbers are investigated in this dissertation. The work was primarily experimental and was conducted in a "Plateau tank" to simulate low-gravity conditions. The main thrust of the experimental work involved the use of an high resolution Fourier optical measurement system for imaging the dynamic bridge shape, measurement of the static and dynamic contact angles and non-invasive analysis of excited surface modes. The liquid bridge supports were moved by computer controlled linear actuators. This allowed precise control of several physical characteristics of the bridge, specifically the volume and the slenderness, as well as vertical, lateral and rotational vibration rates. Other experimental approaches included the replacement of the lower

support disk with a thin disk attached to a cantilever arm to measure the force exerted by a bridge on the lower support disk.

The key concept in the present approach to imaging the bridge is the concept of optically frequency filtering the illuminating light, or apodization. The ability to perform image manipulations through alterations on the Fourier plane began with experiments by Abbe [34] and Porter [35]. However, the initial use of Fourier methods to alter optical images date from experiments by Maréchal [36] and Marquet [37], motivated by Duffieux [38]. Methods of Fourier analysis techniques applied to electrical signals and networks quickly became applied to optical systems [39-42]. The development and use of spatial filters to alter optical images, primarily to eliminate graining and aberrations followed [43-47]. It was also realized that optical manipulations of the Fourier transformation of an optical scene can correspond to what are otherwise time-consuming mathematical operations [48,49].

The Plateau or neutral buoyancy method [22] relies upon the principle that if two imiscible liquids of equal density are configured such that one envelops the other then the curvature of the equilibrium interface is a constant. That is, despite the fact that gravity creates a hydrostatic pressure gradient in each liquid, the interface between the two liquids behaves as if the gravitational acceleration is zero. For non-zero gravity, the density mismatch can be adjusted to cover a range of Bond numbers. In each liquid the pressure p_i, i=1,2, satisfies

$$\nabla p_i = -\rho_i g \mathbf{e_z} \tag{1.1a}$$

or

$$\nabla p_i^* = 0 \tag{1.1b}$$

where $p_i^* = p_i + \rho_i g z$, and ρ_i is the density of the i^{th} liquid phase. At the interface between the two fluids

$$p^*_1 - p^*_2 = (\rho_1-\rho_2)gz + 2\gamma J. \quad (1.2)$$

Here J is the mean curvature of the surface, fluid 1 is the inner (bridge) fluid, and fluid 2 is the outer (bath) fluid. When ρ_1 and ρ_2 are equal, the curvature is a constant, and zero-gravity conditions are obtained. Thus, the outer fluid compensates for the hydrostatic pressure gradient along the interface. To obtain a non-zero Bo, the outer bath density can be changed either by adjusting the composition or temperature [50].

Several scientific requirements had to be met to ensure accurate and precise results. The primary requirement is to produce accurate and stable Bond numbers over the range $10^{-1} \geq Bo \geq 10^{-4}$. This range is given by practical density differences between the bridge and bath liquids for the upper bound and measurement precision for the lower bound. This implies control over bath temperature, bath composition, and an accurate method to determine the densities and interfacial energies of the bridge and bath over various temperatures. Lower Bond numbers can also be obtained by using support disks with a smaller radius. The experimental observations include recording the static interface shape and dynamic contact angle behavior during dynamic processes. Features on the order of tens of microns must be viewed with light that passes through distorting media. Precise control of vibration frequency, amplitude, and direction of the support disks are also necessary. Frequencies range from tenths of Hertz up to a few Hertz, and vibration amplitudes from a fraction of a millimeter to a centimeter. During vibration or rotation, the disk supports must remain parallel, and not exhibit runout or wobble. They must also be easily accessible and replaceable, and the tank should be easy to clean. The bridge and bath fluids must be mutually imiscible, and neither should chemically react with the support disks. The experimental apparatus meets all of these requirements.

1.2 Summary of previous research on liquid bridges, contact angles and interfacial energies

1.2.1 Liquid bridges

Since the early days of research into the effects of low gravity on physical phenomena much attention has been focused on the equilibria and dynamics of liquid bridges and columns held between coaxial circular disks [15, 24-29, 51-134] . There has been a great deal of theoretical work to determine axisymmetric equilibria for various disk configurations, bridge slenderness and rotations [51-94]. The dynamics of axisymmetric liquid bridges subject to different excitations (impulses, vibration etc.) [95-133] has also been studied in some detail. There has been an equally healthy record of experimental work on the ground [51-57, 60-62, 113-116, 132], in sounding rockets [67-70] and in orbiting spacecraft [58, 59, 63-66].

Ground based studies have been made using the Plateau or neutral buoyancy method [51-54, 56-57, 60-62, 113, 115, 116] to simulate microgravity conditions. Small scale (millimetric) bridges have also been used to avoid gravitational effects [54]. The Plateau method involves surrounding a liquid bridge with a liquid which has the same density but with which it is imiscible. The effect of gravity can then be effectively examined by changing the Bond number. This is done by changing the density difference between the bridge and the surrounding fluid. While these methods produce useful results, they are limited either by the small zone size [22], or the presence of an outer fluid which limits the application of the results [22, 60, 134, 135].

1.2.1.1 *Liquid column shapes and stability limits*

Axisymmetric bridges held between coaxial and unequal disks have been studied extensively and are well documented. The shape of a liquid surface can be determined theoretically from the Gauss-Laplace equation [136] that represents a balance between the pressure difference across the surface and the capillary pressure (the product of the surface

tension and the mean curvature). For axisymmetric bridges the volume-, gravity-, rotation- and slenderness-dependencies of the stability limits of the family of surfaces that can exist between two circular disks have been examined theoretically and experimentally [52-61]. A summary of all possible liquid shapes between equal and unequal disks is found in references [84, 94]. Orr *et al.* [30] developed expressions for shapes of bridges between a sphere and a parallel plate for Bo = 0. These expressions can be readily extended to bridges between parallel plates.

For zero–gravity conditions, the equilibrium surface is a surface of constant mean curvature and, for the axisymmetric case, the bridge can have a cylindrical, spherical, catenoidal, unduloidal or nodoidal shapes. Typically, previous investigations of weightless bridge stability have assumed that the perturbations satisfy the constraints of constant liquid volume and fixed contact lines. Our experimental techniques, described in chapter 3, satisfies these constraints. We were concerned with the behavior of the bridge as it loses stability. We investigated the nature of the bridge shape near specific bifurcation and transition points that occur on the axisymmetric stability boundary. Previous work is summarized below.

Rayleigh [137] showed that a right circular cylindrical liquid jet will break up if its length exceeds its circumference. This stability limit is also observed by cylindrical liquid bridges contained between coaxial discs at zero Bond number. It has been established theoretically [138] and experimentally [52, 138] that a cylindrical bridge is stable if the slenderness $\Lambda < \pi$ and unstable if $\Lambda > \pi$. Here the critical perturbation is axisymmetric [137, 138]. It was suggested by Gillette & Dyson [76] that, when the relative volume V = 1, there are no stable non–cylindrical axisymmetric surfaces. Rivas & Meseguer [108] determined the linear dependence of Λ on V for critical unduloids that are close to a cylinder. Constant volume spherical bridges are always stable. This follows from Plateau's experimental results and is easily proved theoretically (see, for example, references [80, 136]). Plateau [138] determined the region of existence for catenoidal

bridges experimentally. A theoretical and experimental analysis of the stability of catenoidal bridges with respect to axisymmetric perturbations was later carried out by Erle, Gillette & Dyson [95]. Besides cylinders, spheres and catenoids, Plateau [138] also undertook experimental investigations of the stability of unduloidal and nodoidal bridge surfaces and qualitatively described the results. For axisymmetric perturbations and arbitrary values of Λ and V, the stability limits were first constructed by Gillette & Dyson [76] on the basis of Howe's theory [139] (outlined in [76, 95, 140]). They also proved that an axisymmetric bridge with no equatorial symmetry plane is always unstable. Furthermore, they later proved [140] that axisymmetric perturbations are the most dangerous for weightless bridges that are symmetric about the z-axis and have surfaces represented by single-valued functions $r = r(z)$. Slobozhanin [80] analyzed the stability of an axisymmetric bridge with respect to arbitrary (i.e., both nonaxisymmetric and axisymmetric) perturbations and constructed the general stability boundary in the (Λ, V)-plane. (These results are presented in English in [136], and the stability boundary is reproduced in [14, 119, 141].) Quantitative experimental data on the boundary of the stability region were obtained by Elagin, Lebedev, and Tsmelev [61] ("microzone" method), and by Sanz and Martínez [53] and Russo and Steen [142] (neutral buoyancy technique).

The conditions for which capillary surfaces with contact lines pinned to solid edges are most unstable to perturbations of the liquid surface, rather than to perturbations of the contact line, were obtained in a more general analysis by Slobozhanin & Tyuptsov [20] (see also [22]). This was also examined for the particular cases of liquid bridges held between disks and rods by Slobozhanin [20, 143].

If an axisymmetric equilibrium state is stable, then, for a small variation of the parameters Λ and V, it has a unique continuous extension and the stability of the state is preserved. However, if the equilibrium state lies on the stability boundary, the uniqueness of the continuous extension is violated and the equilibrium state bifurcates.

Methods for analyzing bifurcations of the equilibrium states of a capillary liquid mass and the possible bifurcation structures have been described in earlier work (see, for example, [22, 74, 141-147]).

To account for Plateau's experimental results, Michael [148] proposed possible bifurcation patterns that are plausible when the different axisymmetric equilibrium shapes of a bridge lose their stability. He further emphasized the need to study the corresponding bifurcation problem in detail. This problem has been solved for a critical cylinder. The solution is a particular case obtained by Brown & Scriven [144] and by Vega & Perales [95]. The dynamical behavior of an axisymmetric liquid bridge as it loses stability on the boundary segment along which axisymmetric perturbations are critical was studied in [99, 105]. Finally, a sophisticated analysis of the nature of the axisymmetric bifurcations along this boundary segment was made in a recent paper by Lowry and Steen [141].

The problem of stability under axial gravity has been examined for particular cases by several workers The stability of cylindrical volumes ($V = 1$) to axisymmetric perturbations has been examined by Coriell *et al.* [12], Meseguer [73], and DaRiva & Martinéz [83]. Vega and Perales [95] obtained analytical approximations in the small Bond number limit. Heywang [149] considered the stability to axisymmetric perturbations for fixed contact angles of 90°. Coriell and Cordes [82] also examined this case but allowed for arbitrary perturbations.

Slobozhanin [117] examined the stability of liquid bridges held between equidimensional coaxial circular disks and subject to steady axial gravity. In contrast to previous work, he considered both axisymmetric and non-axisymmetric perturbations. For $Bo > 3.06$, he showed that stability is always lost to non-axisymmetric perturbations. He also considered several contact angles at each disk and found that as $Bo \rightarrow 0$, the 90° case becomes singular. Russo and Steen [142] investigated the zero Bond number maximum volume limit theoretically (using an energy method) and experimentally (in a

Plateau chamber). They found that for rotund bridges (i.e. $V > 1$) an axisymmetric bridge is first unstable to non-axisymmetric disturbances. This confirmed the experimental results of Plateau who observed that axisymmetric rotund bridges lose stability when the tangent to the free surface at the disk edge is parallel to the flat upper surface of the disk.

Slobozhanin and Perales [118] recently extended these analyses to include the full range of possible contact angles and a wide range of Bo, V, and Λ. They showed that for a finite Bond number, the stability margin can be represented in the V-Λ parameter space as a curve defined by three segments (see Figure 1.4). The upper segment of the curve corresponds to the maximum volume stability limit. Between points O and C stability is lost to non-axisymmetric perturbations. At present no theory exists for the stability of these non-axisymmetric configurations [118] although recent experimental work [150] indicates that some of these configurations are stable (see Chapter 4).

For $Bo < 3.06$ the segment from D to C is characterized by loss of stability to axisymmetric perturbations. This leads to breaking of the bridge into a pendant and sessile drop. A small satellite drop is also created. The third segment of the stability margin corresponds to small volumes and slenderness ($V, \Lambda < 1$). When gravity is directed downward and the bridge liquid is denser than the surrounding medium, loss of stability occurs via dewetting from the upper disk. The experimental results of Bezdenejnykh et al. [55] are in good qualitative agreement with the theory of Slobozhanin and Perales.

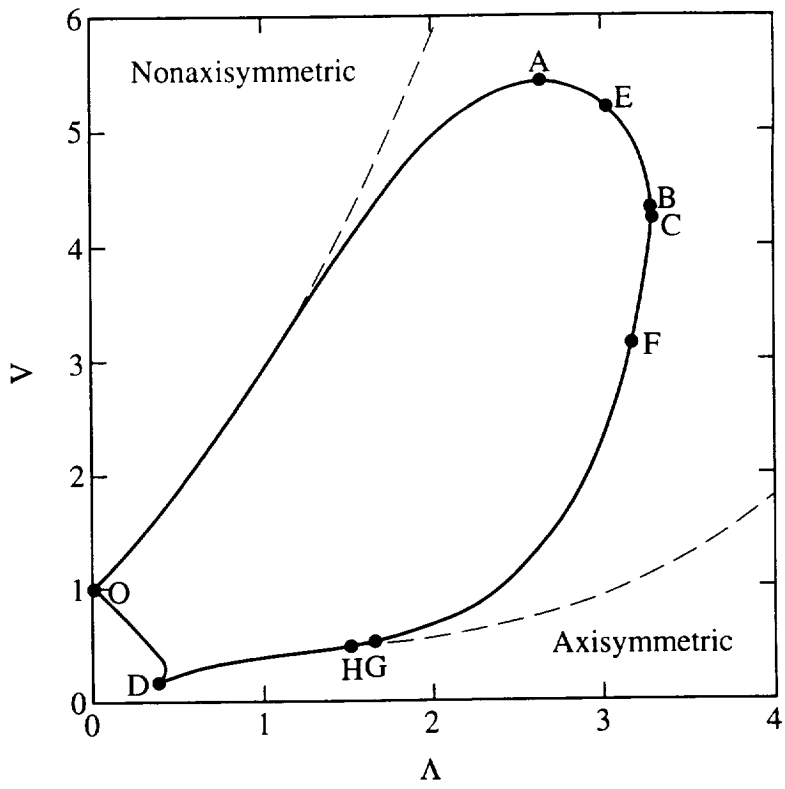

Figure 1.4. Stability diagram for bridges held between coaxial equal circular disks with axial acceleration. Bo = 0 (dashed line) Bo = 0.1 (solid line). A, maximum volume; B, maximum slenderness; C, nonaxisymmetric-axisymmetric transition; D, zero angle at the top disk; E, local pressure minimum; F, local minimum of upper contact angle; G, local maximum of upper contact angle; H, local pressure maximum. (After [118])

Vogel [25, 26] and Langbein [27] have examined the stability of bridges held between flat plates. Here the contact angle is constrained to a given value. Vogel considered zero Bo cases (constant mean curvature). He found that the liquid bridges are symmetric with respect to the plates if the contact angles at both plates are equal. He also showed that for a family of stable liquid surfaces, the capillary pressure increases as the actual volume decreases. The shapes are sections of nodoids, catenoids, and unduloids. A stable liquid surface cannot exhibit an inflection point between the plates. The unduloids become unstable whenever their inflection point coincides with the contact point. Langbein [27] examines the minimum volume stability condition by considering the liquid volume

as a function of the capillary pressure. When a family of solutions of the capillary equation have two neighboring solutions with equal volume, the energy is at a saddle point.

Shear stabilization of bridges has been examined theoretically and experimentally. [24, 113, 116, 151, 152]. Certain shear flows have been shown to be able to stabilize a cylindrical annulus of viscous liquid bounded and sheared by an ambient liquid. Shear applied to liquid columns damps the axisymmetric instability, but not to the extent that all wavelengths decay. Liquid columns with a central rod, however, can be completely stabilized by a shear flow. Lubyimov [153] has shown that for an annular liquid column surrounded by an ambient liquid contained in a cylindrical vessel, the columns can be stabilized through application of circularly polarized vibration.

There have been few theoretical studies of the stability limits and hydrostatics of initially non-axisymmetric liquid bridges. To date, work has been confined to studies of the effects of lateral gravity [96, 120-122] and eccentric rotation [74, 93] for bridges supported by coaxial and non-coaxial equidimensional disks. Perales [96] used an asymptotic method to study the bifurcation of a cylindrical bridge subject to lateral or transverse gravity. Later numerical studies [120-122] confirmed this result. Laveron and Perales [122] have undertaken a more general approach using computational techniques and obtained bifurcation diagrams for non-axisymmetric bridges subject to a transverse, inclined gravity vector. Their work is restricted to the minimum volume limit and gives a detailed analysis of the nature of the bifurcations. They find that for lateral gravity, cylindrical volume bridges with $\Lambda > 2.38$ will lose stability at a subcritical bifurcation for which the associated eigenfunction is antisymmetric. It is speculated that this will lead to a configuration of two nonsymmetric drops. This has been confirmed recently by Alexander *et al.* [121], who also find a satellite drop following the first bifurcation. For $\Lambda < 2.38$ stability is lost at a turning point with an associated symmetric eigenfunction; breaking is symmetric. For a given Bond number the minimum volume stability margin with lateral gravity corresponds to the minimum volume limit for the zero Bond number stability

margin for axisymmetric bridges. Laveron and Perales have also investigated the stability of a gravity vector slightly inclined from the lateral. They show that for these cases, loss of stability occurs at a turning point.

Apart from unpublished work using microzones [154], experimental investigations of the stability of non-axisymmetric bridges under simulated or actual low gravity conditions have been restricted to investigations of the C-mode rotational instability [57, 69].

1.2.1.2 *Oscillations and vibration*

Mason [51] found standing waves could be formed on liquid bridge surfaces by vibrating one of the supports. During the early 1990's there was renewed interest in the study of liquid bridge oscillations. To date, theoretical analyses have involved inviscid bridges [61, 62, 104, 124, 28, 131, 133], one-dimensional models [53, 55, 87, 89, 98, 99, 100, 104-106, 125, 127, 132] boundary layer analyses [128], linearized models and some full numerical simulations. Oscillations have been examined in the limits Oh << 1, Oh = 1 and Oh >> 1 [155]. (Here Oh is the Ohnesorge number, $Oh = \mu/(\rho\gamma R)^{1/2}$ where μ is the dynamic viscosity.) For Oh << 1 Tsamopolous *et al.* [15] found that damping rate and oscillation frequency increased with axial and azimuthal wavenumber. For small bridges, gravity did not appear to affect the eigenfrequency despite distortion of the static and dynamic shapes. In the small Oh limit the eigenfrequency is given by $\Omega_1 = \omega_0 + \omega_1 Oh^{1/2}$ [155] where the first correction to the inviscid mode ω_o depends only on Λ and the mode being perturbed. Borkar and Tsamopolous [128] used a boundary layer analysis for Oh >> 1 and calculated oscillation frequencies and damping rates for bridges undergoing small amplitude oscillations. Damping was found to be due to either the viscous boundary layer or the restrained motion of the three phase contact line. Higueras *et al.* [155] extended

analyses to O(Oh)* valid for weakly dissipative bridges. Our experiments into the behavior of bridges vibrating near resonance focused on the nonlinear behavior of both the eigenfrequency and the eigenmode.

1.2.1.2.1 Axisymmetric oscillations

Meseguer and Perales [125] used the linear Cosserat model to study the effects of step changes in low magnitude steady acceleration and later [132] carried out an experimental study and linear analysis of the vibration of axisymmetric viscous bridges. Transfer functions for both disks were calculated. Zhang and Alexander [106] examined the sensitivity of liquid bridges to axial acceleration for the case of simultaneous excitation of both disks.

Langbein [29] has determined the resonant frequencies of axisymmetric bridges for V =1 by first calculating oscillations of infinite liquid columns. For each frequency an infinite set of oscillations is obtained. These are then superposed to find solutions for finite columns. Explicit dependencies between the eigenfrequencies and Λ and Oh are obtained. Ahrens *et al.* [156] have measured the resonance curves of small liquid columns using stroboscopic illumination and pressure sensors attached to the disks. Recently, Morse *et al.* [157] have measured the resonance curves by exciting the bridge with ultrasonic acoustic radiation.

Non-linear oscillations have been simulated by Chen and Tsamopolous [130] using the full Navier-Stokes equations. Other analysis of non-linear mechanical oscillations are in recent papers by Nicolás and Vega [158], Alexander and Zhang [129], and Meseguer *et al.* [127]. Experimental studies of nonlinear effects during oscillation of small bridges have also been carried out [114, 159]. It was observed that the

---

* $f(\varepsilon)$ is $O(\varepsilon)$ when $\lim_{\varepsilon \to 0} \frac{f(\varepsilon)}{g(\varepsilon)} = 0$

eigenfrequencies decrease as the oscillation amplitude is increased. A similar "softening" effect was reported by Eidel [133].

Meseguer *et al.* [87, 105, 107, 108] and Zhang and Alexander [106] used 1D models to analyze the oscillation of bridges to the point of breaking. Shulkes [134] used a finite element to solve the velocity-potential equations governing the progression of an axisymmetric inviscid liquid bridge toward breakage. He compared his results to 1D Cosserat and slice models. It was concluded that 1D models do not adequately represent the dynamics when the bridge is close to breaking.

1.2.1.2.2 Non-axisymmetric oscillations

Experimental and theoretical studies of non-axisymmetric oscillations are limited. Small amplitude inviscid non-axisymmetric oscillations have been examined theoretically by Gañán and Barrero [97] for small free inviscid oscillations and included the effect of the outer fluid. They calculated the first natural frequency for both axisymmetric and transverse modes (nonaxisymmetric modes) as a function of slenderness and Bond number for cylindrical volume bridges (V = 1). They also located the locus of points in Bond-number frequency space at which both axisymmetric and transverse modes have the same first frequency. It was also found that at critical slenderness Λ_c both modes have zero frequency. This point was found to be a bifurcation point corresponding to the axisymmetric-nonaxisymmetric transition described earlier.

Experimental work with lateral oscillation of the lower disk was also carried out by Sanz and Lopez-Diez [62]. They examined free frequencies, deformation modes, velocity fields and the influence of the surrounding viscous bath. For density matched conditions, i.e., Bo << 1, they found that only the azimuthal mode m = 1 case could be excited. It was found that, due to viscous effects, only the lower longitudinal modes could be obtained. Tsamopolous *et al.* [15] examined small viscous oscillations caused by lateral oscillation of the lower support disk in the absence of an encapsulating fluid and for

V = 1 and Bo = 0. They examined the first five non-axisymmetric modes for azimuthal wavenumbers m = 1 and 2. Their calculated results agreed with those obtained in [63]. They also found that the bridge remained stable to non-axisymmetric disturbances even when the bridge slenderness was increased beyond the Rayleigh limit. This is in accord with the static stability results of Slobozhanin and Perales [118] described earlier (and also results for liquid jets [137] and annular core flows [160]).

1.2.1.3 *Rotation*

Although not discussed in detail in this dissertation, for completeness and comparison, previous work is presented. For rotating bridges, the Weber number, which is the ratio of centripetal to surface tension forces, is the important parameter governing surface shapes whenever Bo << We, i.e. when the centrifugal acceleration greatly exceeds the gravitational acceleration. For coaxial disks, the bridge may be subject to rotation which can result in a C-mode deformation or jump-rope instability of the bridge as observed by Carruthers *et al.* on Skylab [58]. Rotation also modifies the stability limits. For example, the maximum stable slenderness, Λ_{max}, of a cylindrical column rotating with a circular frequency Ω is inversely proportional to the square root of the Weber number, i.e. $\Lambda_{max} = \pi /(1 + We)^{1/2}$.

If B = 0 and We > 0, the relation between critical values of Λ and We is also defined analytically [145, 161] (see also [136, 162-164]). For We = 0 and B > 0, the bridge stability to axisymmetric perturbations was studied in [12] and, if B << 1, in [95, 98]. The stability with respect to arbitrary (rather than only axisymmetric) perturbations was analyzed in [117, 165] (see also [118, 136]). It was found both theoretically (for We > 0 and Bo << 1 [74, 95]) and experimentally [66, 135] that even weak gravity may considerably narrow the stability region for an isorotating liquid bridge with V = 1. The effect of gravity and isorotation on the stability to axisymmetric perturbations for a bridge with V = 1 and Λ close to π ($2.75 \leq \Lambda \leq \pi$) was studied in [74, 66, 166]. An analysis of

the bifurcation problem for the case V = 1, We > 0, 0 ≤ Bo << 1 [74, 81, 95] showed that the loss of stability results in breakage of a liquid bridge.

For the case of a prescribed value of β_1, the stability problem has previously been considered only for the limiting cases of zero-gravity and isorotation, or non-zero gravity and no rotation. For an isorotating weightless liquid bridge (Bo = 0, We ≥ 0) with β_1 = 90°, only cylindrical surfaces may be stable and any other surfaces are either critical or unstable [117, 165]. The dependence of Λ and V on We for neutrally stable surfaces with $\beta_1 = 80°$ and $\beta_1 = 75°$ was obtained in [79, 167]. For any fixed value of β_1 in the interval $0 < \beta_1 < 90°$, it has been shown that an isorotating weightless bridge loses stability with respect to nonaxisymmetric perturbations [168]. The related stability problem for arbitrary values of Bo was first solved in [82] and later in [136]. In addition to $\beta_1 = 90°$, the cases $\beta_1 = 80°$ and $\beta_1 = 75°$ have also been considered [117, 137, 165]. The shape of the molten zone during growth of silicon and germanium crystals ($\beta_1 = 79°$ and 77°) was analyzed in [91].

1.2.1.4 *Force measurements*

There are several papers devoted to the calculations and experimental measurement of the forces exerted by liquid bridges on their supports [16, 30-33]. These are mainly for bridges held between spherical supports. Previous work has concentrated on characterizing pendular bridges between spheres in terms of their volume, curvature and force of adhesion between the spheres. Static and dynamic situations have been analyzed. Mazzone *et al.* [32] found that the force required to separate two moving particles is sometimes two orders of magnitude higher than for the static case due to the viscous resistance to motion in the dynamics case. We were interested in performing accurate measurements of the force exerted by a bridge on a disk support, when the contact line is pinned, especially near static stability limits.

1.2.1.5 *Electric fields*

Although not discussed in detail in this dissertation, for completeness and comparison, previous work is presented. The first studies of the effects of electric fields on liquid bridges were undertaken by Gonzalez *et al.* [56]. Since then interest in these effects has increased [153, 169-173]. The electric field always plays a stabilizing role in the dielectric limit and lowers the minimum volume stability limit. By increasing the electric field and simultaneously decreasing the volume, the symmetry of the breaking process in the presence of a gravitational field can be changed such that two equal volume drops rather than two unequal drops are formed [169].

1.2.2. Contact angle and interfacial energy

In cases where Bo << 1, the physics are dominated by the interfacial energy. The theory of interfacial energy, also called surface tension (see [174, 175] for important differences) is briefly reviewed. The subjects of contact angle, contact line motion (wetting), and interfacial energy are entire fields of inquiry in themselves, and only a passing reference to relevant overlapping portions will be made here.

Of special importance are the basic theory of an interface (especially in terms of a material dividing surface), experimental techniques used to measure the interfacial energy, and the wetting of fluids on a rough substrate. In order to properly calculate Bo, accurate measurements of the interfacial energy had to be performed. The support disk surfaces were rough, and thus the wetting behavior of the oil needed to be studied in order to make a proper materials selection.

There has been a great deal of research on the theory of interfacial energy (see [176-184] for a few major texts) as well as different methods of interfacial energy measurement [185-202]. The concept of interfacial energy as the energy of a surface of division between separate phases of materials has been applied to a diverse group of objects [203-206].

Finally, there has been a great deal of work applied to fluid flow problems involving a moving three-phase line [211-232].

The problem begins with an attempt to mathematically describe and experimentally measure an infinitesimally thin interface. Historically, aside from superficial observations by Aristotle [233] and Galileo [234], the beginning of serious inquiry into the nature of interfacial energy and contact angle began with Young in 1805 [235] with the development of Young's equation:

$$\gamma_{sv} - \gamma_{sl} = \gamma_{lv} \cos \phi_e \tag{1.3}$$

where γ_{sl} is the interfacial energy between the solid and the liquid, γ_{sv} is the interfacial energy between the solid and the vapor, γ_{lv} is the interfacial energy between the liquid and the vapor, and ϕ_e is the equilibrium contact angle. This equation is a simple balance of force at a three-phase contact line. The physical assumptions made in this model are that the solid surface is ideal (nondeformable) in the region of the contact line, and that the three-phase line has little or no curvature. In 1869, Dupré [236] introduced the concepts of the work of adhesion and the work of cohesion in an effort to place the theory of capillarity on a thermodynamic foundation. However, it was Gibbs [181], in 1878, who made the first major advance in the theory of dividing surfaces. Gibbs rigorously derived Laplace's equation relating the local pressure difference across a dividing surface to the local curvature of the surface by minimizing the thermodynamic free energy E - TS of the system when a dividing surface of small curvature is varied. In analyzing the equilibrium of two fluids and a solid, Gibbs allowed the contact line to move off the surface. Although this does not affect the result if the fluids and the solid meet at a continuous (flat) part of the solid, it does if the fluids and the solid meet at a corner of the solid. Gibbs found that there is an equilibrium contact angle at the corner of the solid, where in reality, a range of contact

angles is allowed. This was proven later [20,21]. Gibbs then made an unsuccessful attempt [181] to incorporate the strain of a solid into his calculations.

The overwhelming majority of Gibbs work effectively placed theory well beyond experimental verification, and little theoretical work was carried out for several decades. Bangham and Razouk [237] recognized that in a three phase system, the equilibrium interfacial free energies γ_{sv} and γ_{lv} are related to the pure surface energies of the solid with a vacuum γ_s, and the liquid with its own saturated vapor γ_l, by the equilibrium film pressures π_{sv} and π_{lv}. Simply put, $\gamma_{sv} - \gamma_s = \pi_{sv}$, and $\gamma_{lv} - \gamma_l = \pi_{lv}$. Thus Young's equation is modified to be:

$$\gamma_s - \pi_{sv} - \gamma_{sl} = (\gamma_l - \pi_{lv}) \cos \phi_e \qquad (1.4)$$

In addition, a term π_{sl} can be added which represents adsorption in the solid-liquid interface. For most systems, the film pressures π_{sl} and π_{lv} can be neglected, and only π_{sv} is given consideration. Good, in [184], points out that ignoring the film pressure entirely may produce incorrect results, as some systems may have γ_{lv} much lower than γ_l. Fox and Zisman [238] used an empirical method to determine γ_s, which is to plot γ_l linearly against ϕ for a series of liquids having a decreasing γ_l. This empirical method will only work for pure substances. Also, this method will not work when more than two materials are present at an interface. Good [177, 178, 179] was the next pioneer in surface science, and his collaborations with Girifalco [177, 178], van Oss, and Chaudhury [239-241] were the next significant attempts at understanding the ideas of wetting, contact angles, and solubility. In 1957 and 1960, Good and Girifalco published several papers introducing the "geometric mean rule" [177, 178]. Through use of the geometrical mean rule, Good and Girifalco were able to eliminate γ_{sl} from Young's equation and give support for Fox and Zisman's approach of a limit approaching the critical surface energy that is a measure of the pure surface free energy of the solid. Later developments incorporated the effects of

acids and bases [239-241]. In addition, the theory of capillarity has recently been generalized to include surfaces of moderate or large curvature [181-183].

A major thrust of contact angle research attempted to resolve the phenomenon of contact angle hysteresis. Freundlich [242] was the first to experimentally establish the existence of contact angle hysteresis. In fact, there is a range of contact angles that can exist between the so-called "advancing" contact angle ϕ_a and the "receding" contact angle ϕ_r. The accepted theoretical basis for contact angle hysteresis is that the substrate is non-ideal. That is, the surface is not smooth, rigid or homogeneous.

Wenzel [243] recognized that Young's equation may only hold locally, not over the entire surface, especially if the surface is rough. By defining ξ to be the ratio of actual surface area to the geometrically smooth area, Young's equation is modified to:

$$\xi(\gamma_{sv} - \gamma_{sl}) = \gamma_{lv} \cos \phi_W \tag{1.5}$$

Where ϕ_W is the Wenzel contact angle, which approaches the equilibrium contact angle as the surface roughness increases, as derived rigorously by Good [244].

Neumann [176] carried out a thorough analysis of menisci, and derived Young's equation by varying the Helmholtz free energy as a function of the contact angle. It was necessary to distinguish between ϕ, the phenomenological contact angle, ϕ_e, the (unique) contact angle that solves Young's equation, ϕ_a and ϕ_r, the advancing and receding contact angles, ϕ_W, the Wenzel contact angle, and ϕ_C, the Cassie contact angle. Cassie [245] proposed that for a heterogeneous surface, with intrinsic contact angles ϕ_{e1} and ϕ_{e2}, and fractional surface areas Σ_1 and Σ_2, the apparent contact angle ϕ_C is given by

$$\cos \phi_C = \Sigma_1 \cos \phi_{e1} + \Sigma_2 \cos \phi_{e2} \tag{1.6}$$

Note that ϕ_C and ϕ_W do not constitute Young contact angles, because they do not apply to smooth, homogeneous solid surfaces. Neumann also carried out a systematic computational analysis of piece-wise heterogeneous surfaces. He concluded that most, if not all, contact angle hysteresis can be explained by considering the effect of a heterogeneous surface with patches of differing free energies, and corresponding different equilibrium contact angles. His computations showed that the patchwork of heterogeneities causes the free energy of the interface to have several metastable states, and this leads to different equilibrium contact angles. Neumann showed that the hysteresis effect can be removed by making the grains smaller than the thickness of the liquid/vapor interface, approximately 0.1 μm. If the grain size is smaller than this, the surface appears homogeneous to the interface and the hysteresis effect will disappear.

Neumann then went on to discuss surface roughness [176], by idealizing a rough surface as a sawtooth pattern with symmetric deviations about 90 degrees (the smooth normal). In this case metastable states of the contact angle exist as well. Neumann postulated that the contact angle will fall to the lowest possible angle, zero degrees, but did not continue this line of inquiry. In fact, several methods [246] of determining surface tension, including capillary rise methods, drop weight methods, the du Nouy ring method, and the Wilhelmy plate method demands a zero degree contact angle to obtain maximum accuracy. Good and Neumann [200] even suggest that the Wilhelmy plate be roughened using ground glass or sandblasted to make sure the angle is zero degrees. We observed that the best experimental conditions were obtained when the disks were slightly roughened, allowing the oil to completely wet the surface.

When discussing contact angles, it is imperative to be absolutely clear as to which contact angle is being referred to. There is ϕ, the true (microscopic) contact angle that may or may not be measurable (see section 2.2.2), ϕ_a and ϕ_r, the advancing and receding contact angles, ϕ_e, the contact angle that satisfies Young's equation, given all the assumptions implicit in the equation, and ϕ_W and ϕ_C, contact angles that refer to rough or

heterogeneous solid substrates. In general, the current investigation attempted to measure ϕ. As seen below in section 1.2.3, what was actually measured was a local slope (the "macroscopic" contact angle) which is related to ϕ (the "microscopic" contact angle) in a complex way. This problem can be addressed by measuring the slope in a consistent location from one experiment to another, at similar magnifications.

1.2.2.1 *Experimental techniques to measure the interfacial energy*

Adamson [246] comprehensively lists over 20 different experimental techniques to measure the interfacial energy between two fluids. These can be broken down into three broad types of measurements: shape analysis of a drop, a balance of gravitational and interfacial energies, and dynamical flow-type measurements. We tried many different methods, as each has its own set of assumptions and limitations.

1.2.2.1.1 Shape analysis

Shape analysis is an "inverse" method that involves fitting an observed shape to a computed profile. This includes the bubble shape, pendant drop, and the method of curvature. This method is also used in some liquid bridge research, in that the digitized profile of the bridge is fitted to a model by allowing the Bond number (interfacial energy) to vary. In all of these cases, the interfacial energy is calculated from a set of parameters measured from an image. We have used the hanging drop method. It is a simple method, and gives good accuracy. Shape parameters are measured from a pendant drop, which is the largest stable drop that remains attached to a round support, (Figure 1.5) and the interfacial energy is given by [246]:

$$\gamma = \frac{\Delta\rho g d_e^{\,2}}{H} \tag{1.7}$$

where 1/H is a function of d_s/d_e and can be found in a look-up table, such as [197, 247]. It is important that the drop be as large as possible yet remain stable.

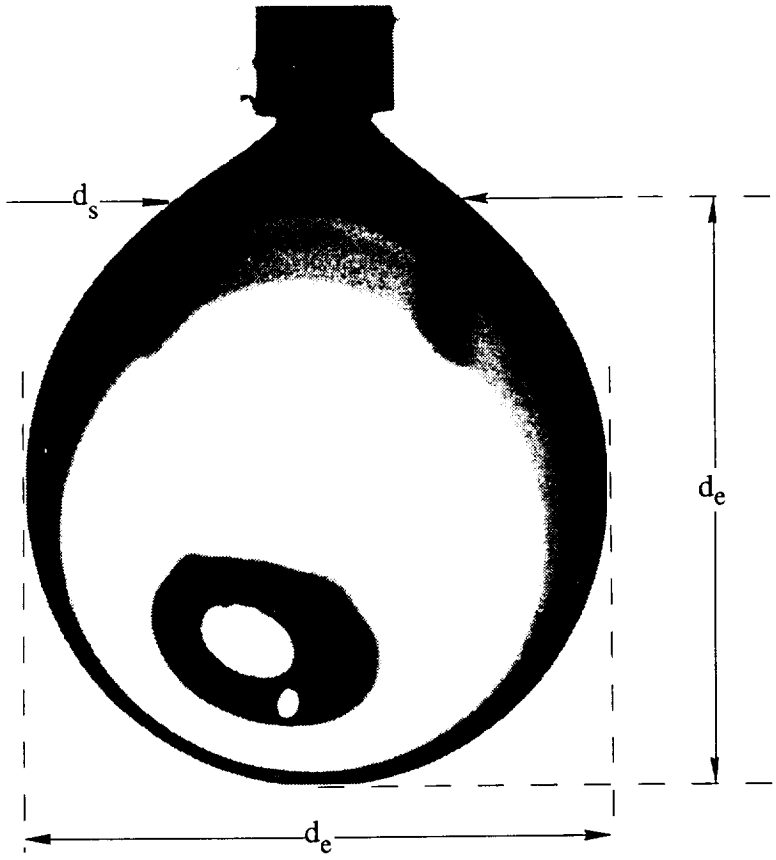

Figure 1.5. Image of a hanging drop.

1.2.2.1.2 Balance of gravity and interfacial energy

These methods include the capillary rise, drop weight, du Nouy tensiometer, Wilhelmy plate, maximum bubble pressure, sessile drop, wire, capillary pull, and film balance methods [246]. All of these methods rely on the balance of gravitational potential energy and interfacial energy. These methods, with the exception of the drop weight, sessile drop, capillary rise, and maximum bubble pressure methods require use of an electrobalance to measure the small value of γ. It is usually necessary to satisfy the perfect

wetting condition (in the sessile drop method, perfect non-wetting) to provide an accurate result. It is also important in this method to have a circular dropping tip. Some of these methods can still be used if the condition of $\phi = 0°$ or $180°$ is not met, but then the contact angle must be accurately measured as well. We have used the drop weight method. It requires a minimum of equipment, is fairly accurate and the contact angle does not need to be measured. In the drop weight method, a drop is slowly created and allowed to detach from the dropping tip. It is assumed that this is a quasi-static process, and that the detached drop is the theoretical maximum in weight. The interfacial energy is given by [246]:

$$\gamma = \frac{\Delta\rho g V_0}{2\pi r f} \tag{1.8}$$

where f is a correction factor that accounts for the fact that not all of the drop detaches from the dropping tip. The values of 'f' for mercury in air are tabulated in [197, 247].

1.2.2.1.3 Dynamical methods

This category includes the falling column of liquid method, flow method, levitated or oscillating drop, oscillating jet, rotating drop, capillary wave and liquid sheet methods [246]. These all require a large investment in time and equipment to accurately perform a measurement. The interfacial energy is related to the eigenfrequency of the drop. The capillary wave method can be used as part of a light scattering experiment. Microscopic surface waves are always present, and the interfacial energy is related to the period and wavelength of these oscillations. The liquid sheet method uses colliding jets of fluid to create a stable circular sheet, the radius of which is related to the interfacial energy. The oscillating jet and flow methods require flow out of a non-circular orifice, and the interfacial energy is related to the slenderness of the orifice and the wavelength of the exiting jet of liquid.

1.2.3 Contact line motion

Although this problem was not studied in detail, it is a relevant issue regarding materials selection (Chapter 3) and contact angle measurements (Chapter 6). The majority of pioneering work on the theory of contact line motion has been made by Dussan [212, 216, 217, 228-230] in collaboration with others, in terms of identifying the appropriate boundary conditions of contact line motion to solve the Navier-Stokes equation for the shape of the fluid interface. The application of the no-slip boundary condition to a moving fluid boundary introduces a non-integrable singularity at a three-phase line [229, 239]. In response to this, several models incorporating slip have been introduced [225, 229, 231, 232] resulting in surprisingly good agreement between experiment and theory [213]. In 1989 Ngan and Dussan [217] showed that the formulation of the boundary-value problem relies only upon one parameter Ω:

$$\Omega \equiv \phi + Ca\left\{\frac{2\sin\phi}{\phi - \cos\phi\,\sin\phi}\left[\ln\frac{a}{L_s} + 1\right] + l_i(\phi)\right\}, \tag{1.9}$$

which is a combination of the true contact angle ϕ, the capillary number $Ca = \mu v/\gamma$, the length scale "a" associated with the inner (microscopic) region of the fluid and the slip length L_s, and a function that depends on the specific slip model $l_i(\phi)$. If in fact a slip model is appropriate, the contact angle as a function of distance "r" from the contact line obeys: (see Figure 1.6)

$$\phi(r) \approx \Omega + Ca\frac{2\sin\Omega}{\Omega - \cos\Omega\,\sin\Omega}\ln\frac{r}{a} \tag{1.10}$$

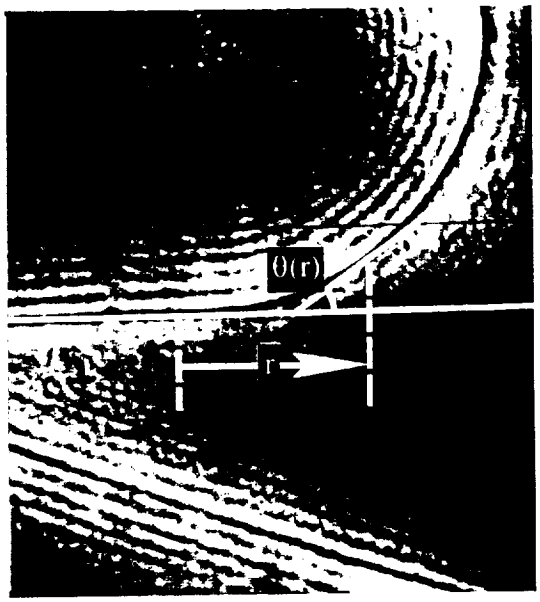

Figure 1.6. A moving fluid interface under high magnification.

Dussan was primarily concerned by determining under what conditions the inner region determines the behavior of the bulk region. In contrast to this approach are the molecular dynamics simulations of Koplik [221, 222] in which the no-slip boundary condition arises naturally as a result of a dense liquid interacting with a solid wall. It appears (in the simulations) that the individual molecules absorb a high but finite amount of shear at the expense of some slip. The main thrust of the articles is that a simulation involving only a few thousand molecules is enough to display continuum (i.e. no-slip) behavior. What all of the various slip models and models incorporating moving contact lines share is the insistence that the contact angle be measured as close to the contact line as possible.

Although progress over the years has produced much insight into understanding how a fluid behaves in the vicinity of a three-phase line, many questions still need to be answered. There has not, as yet, been a definitive statement on how the dynamic or static apparent contact angle and the true contact angle are related, or even how to define the

apparent contact angle. Neither has there been a satisfactory method of characterizing rough or chemical inhomogeneous surfaces, other than some rudimentary statistical methods [184]. The applicability of the geometric combining rule needs to be explored further, particularly for solutions. The surface free energy of a strained solid has not been given satisfactory treatment.

1.3. A brief summary of experimental results

In this section, the experimental results obtained during the course of this research project are briefly presented. Details are presented in later chapters.

A series of experiments studied the static stability limits of axisymmetric liquid bridges (chapters 4 and 5). Other experiments followed the dynamic behavior of liquid bridges whose supports underwent sinusoidal motion (chapter 6). Finally, a series of experiments measured the force exerted by the liquid bridge on the lower support disk (chapter 7).

1.3.1 Static stability limit results

This can be divided into two different groups: $K = 1$ and $K \neq 1$.

For $K = 1$ (chapter 4), the axisymmetric stability limits at $Bo = 0.002$, 0.054, and 0.089 were measured (Figure 4.8). The transition point between axisymmetric and nonaxisymmetric breaking modes was found for $Bo = 0.089$. Agreement with theory was good for the lower limit, but the upper experimental limit was consistently 5-10% below the theoretical limit at large values of Λ. It was found that all transitions to a nonaxisymmetric state lead to a stable nonaxisymmetric bridge except for the transition point between axi- and nonaxisymmetric states. The nature of the bifurcation across the maximum volume stability limit was studied and was found to transit between a supercritical bifurcation and a subcritical bifurcation at an slenderness between 0.40 and 0.60. Bridges with slenderness 0.2, 0.3, 0.4, 0.6, 0.8 and 1.0 pulled near Bond number 0

and as small injections of oil were added, the change in shape of the bridge was monitored under high magnification. The rate of change of shape to volume increment, $d\xi/dV$, was plotted and the curves (Figure 4.12) show a rounded appearance for slenderness greater than 0.60 and a peaked appearance for slenderness less than 0.40. This agrees with theory.

For $K \neq 1$ (chapter 5), the stability limits of axisymmetric bridges at $Bo = \pm 0.1$ for $K = 0.09$, 0.2, 0.4, 0.6 and 0.8 were measured (Figure 5.2). Agreement with theory was good for the lower limit and the upper limit was again consistently 5-10% below the theoretical limit at large values of Λ. The transition of the neck location for $Bo = 0.1$ was found and was used to measure the interfacial energy of silicone oil and the bath fluid (Figure 3.12). The transition on the upper stability boundary from nonaxisymmetric to axisymmetric states was found for $K = 0.2$ (Figure 5.4). The behavior of a bridge near the lower stability limit as $K \rightarrow 0$ was investigated for $K = 0.09$ (Figures 5.6, 5.7).

1.3.2 Dynamics

Several experiments were performed in an effort to measure the resonant frequencies (chapter 6). The values of $N = 1,2,3$; $m = 1$ resonances were estimated for bridges of slenderness 2.0, 2.6, and 3.0 (Figure 6.2) (V = 1, 100 cs oil). The ratio of maximum bridge displacement relative to disk displacement was measured for a bridge of slenderness 2.6 from 0.86 to 0.973 Hz at amplitudes of $6.3*10^{-3}$, $3.16*10^{-2}$ and $6.3*10^{-2}$ g (Figure 6.4). Contact angle motion was measured (Figure 6.5) for bridges of slenderness 2.6 and 3.0 (V=1, 5 cs oil) in the neighborhood of $N = 1$, $m = 1$ for the following conditions:

slenderness 2.6: frequency from 0.65 to 0.75 Hz, increment = 0.01 Hz, acceleration = $1*$, $2*$, $3*$ and $4*10^{-4}$ g, static $Bo < 10^{-4}$.

slenderness 3.0: frequency from 0.52 to 0.66 Hz, increment = 0.01 Hz, acceleration = $2*10^{-4}$ g, static $Bo < 10^{-4}$.

The contact angle was measured many times during one complete cycle to ensure the maximum and minimum were measured. The gain curves show evidence of saturation. The range of contact angle motion shows a small dip at the resonant frequency. For slenderness 3.0, the dip occurs on the opposite side of the resonance peak than slenderness 2.6. The resonance frequency shows a positive drift with increasing acceleration (slenderness 2.6) The Fourier plane was imaged during lateral vibration of a bridge slenderness 2.6 at 0.68 Hz for accelerations 0, 2*, 4*, $8*10^{-5}$ and 1*, $2*10^{-4}$ g (Figure 6.10). The spatial frequency components are visible. The filtered bridge images for the same accelerations were subjected to FFT analysis as well (Figures 6.11, 6.12). These show the presence of higher-order spatial modes in a bridge oscillated at the fundamental resonant frequency.

1.3.3 Force balance data

Paths in Λ-V space were traced by keeping V_0 constant and changing Λ (chapter 7, Figure 3.14). This was done at various values of Bo. The static force exerted by the bridge on the lower disk was measured and graphed as force versus slenderness (Figure 7.4). For low slenderness bridges, the force curve exhibits a maximum before breaking. At larger slenderness, the force curve does not exhibit a maximum. The force was calculated by numerically solving the equation for the bridge profile (Figures 7.5, 7.7). The experimental paths are given below in Table 1.1:

Table 1.1. A list of initial and final bridge configurations.

Bo	Λ_i	V_i	Λ_f	V_f
0.015	0.314	2.02	0.966	0.658
	0.712	1.786	1.804	0.705
	1.30	2.45	3.02	1.05
	1.70	4.11	3.40	2.05
	2.89	5.94	4.41	3.89
0.009	0.338	1.88	1.27	0.523
	0.219	1.16	0.577	0.441
	0.134	0.946	0.224	0.568
0.016	1.555	1.622	2.423	1.00
	2.4097	1.885	2.912	1.559
	2.845	2.702	3.420	2.316
	2.561	4.083	3.440	3.039
	2.50	4.52	3.445	3.28
0.0012	1.687	2.89	2.888	1.689
	2.232	4.458	3.984	2.497
	2.403	5.897	3.984	3.557
0.056	0.50	1.004	0.694	0.723
	0.677	1.367	1.268	0.730
	0.928	1.448	1.576	0.855
	1.067	2.056	2.168	1.011
	1.398	2.173	2.452	1.238
	1.451	2.676	2.525	1.537
	1.815	3.72	2.518	2.549
-0.063	0.103	2.05	0.211	1.00
	0.252	1.505	0.431	0.880
	0.707	1.732	1.18	1.038
	1.955	2.506	2.835	1.728

The lower stability limit was approached, but not the upper stability limit because the bridge would slip over the edge of the force balance disk.

Chapter 2

THEORETICAL DEVELOPMENT

In this chapter the theoretical basis for the liquid bridge research described in this dissertation is presented. First, a short history of the problem of Plateau will be presented. Next, without proof, the governing equations for liquid bridge statics and dynamics are presented, as well as a short description of typical solution methods.

1. Plateau's Problem

The problem of Plateau is to prove the existence of a minimal surface bounded by a given contour Γ. This was first suggested by Plateau in 1863 [248]. The complete solution to this problem remains unsolved. Of primary difficulty in the solution is the fact that this problem is represented by a system of non-linear differential equations with the additional non-linear constraint that the area of the surface is minimal. The problem was first linearized by a reparameterization and a method was developed to solve the linear problem in the most general form based on ideas of Reimann, Weierstrass and Schwarz [249]. The first proof of existence given the most general type of contour, an arbitrary Jordan curve Γ in n-dimensional Euclidean space $\mathbf{E}^n$, was presented by Douglas [250] and simultaneously by Radó [251]. The Jordan curve theorem states that if Γ is a simple closed curve in $\Re^2$ then $\Re^2 \setminus \Gamma$ has exactly two components, a bounded component (the inside) and an unbounded component (the outside), each with Γ as a boundary. Douglas's

work is in a sense more general that the original problem of Plateau. Douglas considered a minimal surface bounded by k Jordan curves and which additionally has a prescribed topological structure, e.g. orientable or non-orientable, one-sided or two-sided, and to have a prescribed genus. The existence theorem of Douglas reads: let Γ be an arbitrary Jordan curve in $\mathbf{E}^3$. Then there exists a regular, simply-connected minimal surface bounded by Γ. Douglas accomplished this task by departing from the classical variational problem into a different method not using derivatives. The problem of Plateau was solved in the classical variational method by Courant [252], who claimed that his method yields solutions not available by the method of Douglas. Plateau's problem continues to be an active area of mathematical research [253-261]. Recently answered is whether the surface can exist without self-intersections. It should be stated that the original problem of Plateau, the existence of a regular, simply-connected minimal surface in $\mathbf{E}^n$ bounded by an arbitrary Jordan curve Γ, is as of yet still unsolved [253]. In general, the surface is not a unique solution. Also unsolved is the related question of whether solutions to the problem are stable to perturbations.

The liquid bridge problem is a subset of the original problem of Plateau. The liquid bridge problem requires the existence of a minimal surface with a constrained volume and fixed boundaries, in the case of contact line anchoring.

2. Governing equations for liquid bridge equilibria and dynamics

The governing equations will be presented without proof. For more detailed derivations, please refer to the appropriate reference or appendix. The general inviscid equations, following [62, 68, 118] are first discussed. The equation for the static interface is defined as $F = r - f(\theta,z) = 0$ where f is the deviation of the interface from a cylinder of radius r. The shape of the interface is defined by the pressure jump across the interface $\Delta p = p^{in} - p^{out}$:

$$\Delta p = 2\gamma J = \nabla \cdot \frac{\nabla F}{|\nabla F|} \cdot 2\gamma \tag{2.1}$$

which is written explicitly as:

$$\Delta p = 2\gamma \frac{F\left(1+F_z^2\right)\left(F_{\theta\theta}-F\right)+FF_{zz}\left(F^2+F_\theta^2\right)-2F_\theta\left(F_\theta+FF_zF_{z\theta}\right)}{\left[F^2\left(1+F_z^2\right)+F_\theta^2\right]^{3/2}} \tag{2.2}$$

where subscripts indicate partial derivatives with respect to the subscripted variable. See Appendix E for a detailed derivation of Equation 2.2.

For calculating the shapes of axisymmetric bridges, a common method used is the "shooting" method of numerical solution. The results of these calculations are used for determinations of stability limits (Chapters 4 and 5) and for force calculations (see Chapter 7). When using the shooting method, the interface is reparameterized in terms of r(s) and z(s) where s in the arclength as measured from a support surface. All quantities are made dimensionless with the parameter $L_c = \sqrt{\gamma/\Delta\rho \cdot g}$. In the shooting method, boundary conditions at s = 0 and s = s_f are replaced by conditions only at s = 0. r(s) and z(s) are functions of Λ, V and Bo. Numerically integrating the following equations:

$$\begin{aligned} r''(s) &= -z'(s)\beta'(s) \\ z''(s) &= r'(s)\beta'(s) \end{aligned} \tag{2.3}$$

with the following boundary conditions:

$$\begin{aligned} r(0) &= r_0 \\ r'(0) &= \cos(\beta_1) \\ z(0) &= 0 \end{aligned} \tag{2.4}$$

$$z'(0) = \sin(\beta_1)$$

where primes indicate a derivative with respect to arclength, and $\beta = \beta(s)$ is the angle between the tangent to the shape and the horizontal, provides solutions. Equation 2.3 can be derived by noting that $r' = \cos\ \beta$ and $z' = \sin\ \beta$. $\beta'(s)$ can be calculated from: $\beta'(s) = \varepsilon z(s) + \frac{\Delta p}{\sqrt{|\Delta\rho \cdot g| \cdot \gamma}} - \frac{z'(s)}{r(s)}$, where ε indicates the direction of the effective gravity: $\varepsilon = -\text{sign}(\Delta\rho \cdot g)$. The volume preservation constraint is:

$$V = \frac{\int_0^{s_f} z'(s) r^2(s) ds}{LR^2}. \tag{2.5}$$

An axisymmetric equilibrium configuration of a liquid bridge is stable only if it is stable with respect to both axisymmetric perturbations (the normal to equilibrium surface component N of such perturbation is $\varphi_0(s)$) and the most dangerous nonaxisymmetric perturbations. The latter correspond to the first harmonic in the polar angle θ and have the form $N = \varphi_1(s) \cos\theta$. We use the method described in [136] to study the stability to perturbations satisfying fixed contact line and constant volume perturbations. An equilibrium bridge is stable to axisymmetric (to nonaxisymmetric) perturbations if the function D(s) (function $\varphi_1(s)$),

$$D(s) = \varphi_{01}(s)\int_0^{s_f} r\varphi_{02}(s)ds - \varphi_{02}(s)\int_0^{s_f} r\varphi_{01}(s)ds \tag{2.6}$$

does not vanish on the interval $0 < s \le s_f$. Here the functions $\varphi_{01}(s)$, $\varphi_{02}(s)$ and $\varphi_1(s)$ are the solutions of the following initial-value problem:

$$L\varphi \equiv \varphi'' + \frac{r}{r'}\varphi' + \left(br' + 2prz' + \frac{z'^2}{r^2} + \beta'^2 \right)\varphi \tag{2.7}$$

If there is at least one point s, $0 < s < s_f$, at which D(s) or $\varphi_1(s)$ vanishes (in practice, changes sign), then the bridge is unstable.

We define the point $s = s^*$ as the first point on the solution of Equation (2.6) and (2.7) at which one of the functions D(s) or $\varphi_1(s)$ vanishes. For a neutrally stable surface, axisymmetric (nonaxisymmetric) perturbations are critical when D(s) ($\varphi_1(s)$) first vanishes at $s = s^*$. To find the profile of a neutrally stable surface with a prescribed value of β_1 and a chosen r_0, we vary the parameter $q = \frac{\Delta p}{\sqrt{|\Delta\rho \cdot g| \cdot \gamma}}$ until the conditions of $r(s^*) = r_0$ and constant volume are satisfied within the required accuracy. For the construction of a general boundary of the stability region, this procedure is performed for a sequence of possible values of the angle β_1.

Now examine the governing equations for viscous oscillations of liquid bridges, following [15] are presented. The dimensionless conervation of mass and momentum equations are: (see appendix B for a detailed derivation)

$$\nabla \cdot \mathbf{v} = 0 \tag{2.8}$$
$$\frac{D\mathbf{v}}{Dt} = \mathbf{F} - \frac{1}{\rho}\nabla p + \frac{1}{Re}\nabla^2 \mathbf{v}$$

with the following boundary conditions:

Tangential stress vanishes: $\mathbf{t}_\theta \cdot \mathbf{T} = \mathbf{t}_z \cdot \mathbf{T} = 0$, $r = f(\theta,z,t)$ (2.9)

Balance of normal stress: $\mathbf{T} \cdot \mathbf{n}/Re + 2J\mathbf{n} = 0$, $r = f(\theta,z,t)$

Kinematic boundary condition: $\mathbf{n} \cdot \frac{\partial F}{\partial t} = \mathbf{n} \cdot \mathbf{v}$

Where Re is the Reynolds number $\rho vR/\mu$, $\mathbf{n}$ is the surface normal, $\mathbf{T}$ is the surface traction (see appendix B) and $\mathbf{t}_\theta$, $\mathbf{t}_z$ are the unit surface tangents. The kinematic boundary condition equates the velocity of the surface to the fluid flow velocity. When axisymmetric

perturbations are considered, the radial velocity and its derivative with respect to $\mathbf{e}_r$ are zero at the centerline, and the azimuthal velocity is zero everywhere. Therefore, given a divergence-free velocity field, the axial velocity must be zero at the centerline as well. For nonaxisymmetric disturbances, the axial velocity at the centerline must be independant of θ, which is satisfied only if it is equal to zero. The condition of the radial and azimuthal velocities depends on the wavenumber m (from [15]):

$$\begin{aligned} &m = 1: && v_r + v_\theta = v_z = 0,\ r = 0 \\ &m \geq 2: && v_r = v_\theta = v_z = 0,\ r = 0. \end{aligned} \tag{2.10}$$

In addition, the contact line remains fixed, and all velocity components are periodic in θ:

$$\begin{aligned} f(z,t) &= 1,\ z = \pm\Lambda \\ f(\theta,z,t) &= f(\theta+2\pi,z,t) \end{aligned} \tag{2.11}$$

as well as the usual volume constraint.

In order to calculate the eigenmodes and eigenfrequencies, the equations are linearized around a steady state. Small volume-preserving perturbations of amplitude ε are made for all dependent variables:

$$\mathbf{v} = \mathbf{v}_b + \varepsilon\mathbf{v}_p,\ p = p_b + \varepsilon p_p,\ f = f_b + \varepsilon f_p,\ \mathbf{T} = \mathbf{T}_b + \varepsilon\mathbf{T}_p. \tag{2.12}$$

The base states are calculated for a static case. Finally, the usual decompositions are made for the variables:

$$
\begin{aligned}
v_{r,p}(r,\theta,z,t) &= \hat{u}_r(r,z)e^{im\theta}e^{-\sigma t} \\
v_{\theta,p}(r,\theta,z,t) &= \hat{u}_\theta(r,z)e^{im\theta}e^{-\sigma t} \\
v_{z,p}(r,\theta,z,t) &= \hat{u}_z(r,z)e^{im\theta}e^{-\sigma t} \\
p_p(r,\theta,z,t) &= \hat{p}(r,z)e^{im\theta}e^{-\sigma t} \\
f_p(r,\theta,z,t) &= \hat{f}(r,z)e^{im\theta}e^{-\sigma t}
\end{aligned}
\tag{2.13}
$$

where m is the azimuthal wavenumber, and σ is the (complex) eigenvalue.

Chapter 3

EXPERIMENTAL APPROACH

In this chapter the experimental apparatus, physical measurements and calibrations, any general experimental techniques that were used for the different experiments will be discussed in depth. Finally, the error sources in the system will be presented.

3.1. Experimental Apparatus

3.1.1 Plateau tank apparatus

The experimental apparatus consists of a neutrally buoyant, or Plateau tank (see Figure 3.1) containing 3.8×10^4 cm^3 of bath liquid. The tank is a rectangular glass-walled box with a machined aluminum base-plate. The base-plate has a 5 cm diameter hole for the lower support mechanism and a 0.95 cm hole for a drainage tube. The apparatus support structure (not shown) consists of 5 cm diameter cast iron pipes filled with sand to reduce vibration. The support structure is securely anchored to a 1.22 x 2.44 m optical bench fitted with vibration-damping legs. There are two sets of motors. The lower set are attached to a large aluminum plate that can be adjusted to precisely align the upper and lower support disks. The upper disks are rigidly attached to the support structure. All metal has been painted flat black to reduce reflective interference with the optical systems. The top of the tank is covered with a Styrofoam® slab to reduce evaporative loss of the

bath liquid. Bridge supports are threaded onto upper and lower support rods. A wide variety of sharp-edged disk supports of various materials, sizes and receding angles were machined along with spherical caps of various materials, wire rings, and disks mounted on cantilever arms. The support structures are easy to fabricate, and new supports are machined as needed for experiments. For most experiments 1 cm stainless steel sharp-edged disk supports are used, although a cantilever arm was used for force measurements and spherical caps used to study moving contact lines.

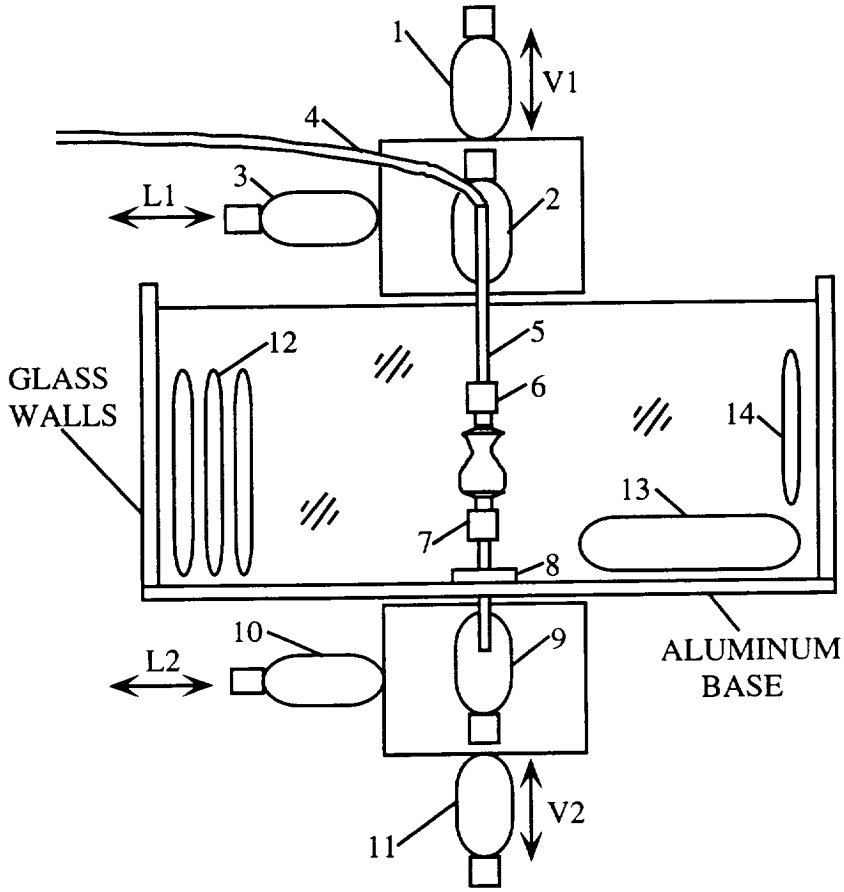

Fig. 3.1. Plateau Tank Apparatus: (1) upper vertical displacement motor V1 (2) upper rotational motor (3) upper lateral displacement motor L1 (4) oil injection line (5) upper spindle (6) upper feed disk (7) lower feed disk (8) slip-ring gasket (9) lower rotational motor (10) lower lateral displacement motor L2 (11) lower vertical displacement motor V2 (12) cooling coils (13) bath circulator (14) heating coil

3.1.2 Temperature control

A small heater was used for increasing the bath temperature, and a copper coil attached to a cold water source was used to lower the bath temperature. Temperature measurements showed that the temperature of the bath could be held steady to 0.05 °C over an 8 hour period, and 0.01 °C over a 30 minute period (see Figure 3.2). The temperature was measured with a platinum resistance thermometer with a precision of 0.001 °C. Typical experiment times were 2 hours or less. A filtering pump was used to both stir the bath and to remove any foreign material in the bath solution. All three (pump, heater and cooling coils) were turned off during experiments. A circulator was not used as it was impractical and unnecessary for the large volume of bath liquid. The temperature was selected to be near the ambient temperature of the room, approximately 22°C, and schlieren images showed that bath temperature nonuniformity is negligible. If the temperature drifted out of the allowed range ($\Delta T = 0.01°C$) during an experiment, the experiment was stopped and the bath brought to the correct temperature before resuming the experiment. A change in temperature of $\Delta T = 0.01°C$ corresponds to a Bond number change of $\Delta Bo = 1.5 \times 10^{-4}$.

The stepper motors draw large amounts of electrical current, and correspondingly, tend to generate large amounts of heat. The lower support rod is directly coupled to one of the lower stepper motors, and heat generated by this motor will rapidly conduct up into the bath. The other motors are not as well coupled to the bath, and do not greatly contribute to the heat flux. The heat will cause the bath fluid in the vicinity of the support rod to expand, generating both convective flow in the bath fluid centered around the liquid bridge, as well as changing the overall temperature of the bath. Thus it is important to monitor the generation of heat by the motors. The change in density of the bath can be easily visualized with schlieren imaging. When schlieren fringes appear, the experiment must be stopped and the motors allowed to cool down, a process that can take several hours. A circulation fan or small blower placed near the lower motors would help alleviate this problem.

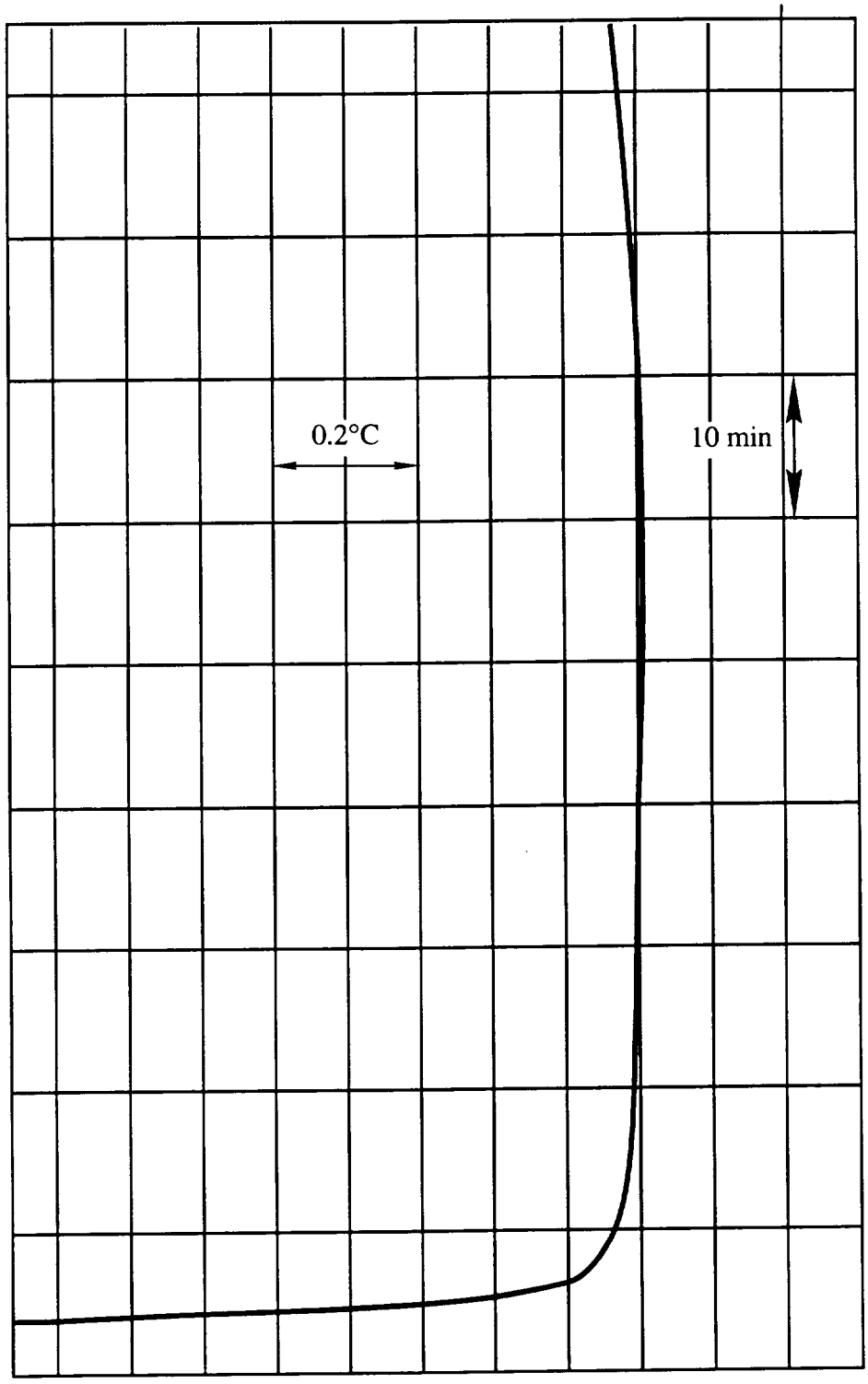

Figure 3.2. Time variation of bath temperature.

3.1.3 Liquid bridge manipulation

The liquid bridge was formed and manipulated using computer control. The system involves a PC (133 MHz), which communicates with indexers for the motors (Compumotor®, series AT 6400). The indexers communicate with the AC power supply encoders for the motors, which drive linear tables (Parker® systems, Daedal division). Our system has 2 AT6400 cards, one driving 4 motors and the other driving 2 motors from a separate indexer. The execution time between consecutive commands is approximately 2 milliseconds according to the manufacturer. The combination of the motor resolution and the screw thread in the linear tables provides a resolution of 125000 steps/inch. In addition, there is a joystick interface which can control up to 4 motors simultaneously. The stepper motors and linear tables were found to have completely repeatable motion, i.e. no measurable backlash. Liquid bridges are created by manual injection of silicone fluid (nominally) with a microsyringe (Hamilton Gastight® series, 50μl and 500 μl) while the stepper motors separate the support disks. Typical bridge volumes are of the order 2 cm^3. Past attempts to automate the syringe failed for various reasons. A glass syringe offers precision, but small angular misalignments between the barrel and plunger caused sticking and the potential for breakage. A plastic syringe could accommodate misalignment, but the rubber-tipped plunger initially deforms instead of travels, resulting in inaccurate volume injection.

Quasi-sinusoidal motion for a fixed period and acceleration is performed by suitable adjustment of velocity rate as well as distance traveled (see Figure 3.15). The particular frequency and amplitude of vibration chosen depend on the particular experiment being performed. Either upper or lower or both support disks may oscillate axially or laterally, in or out of phase, depending on the experiment.

3.2. Coherent Fourier Imaging Optical System

A coherent imaging optical system that operates on the Fourier transform of the image of a liquid bridge silhouette has been developed. By blocking the zero frequency, or dc component of the optical scene, only the high-frequency components corresponding to edges are passed through the system. This approach was used because one of our objectives was to investigate the importance of contact line and angle dynamics on the characteristics of dynamic liquid bridges. Optical techniques allow a higher measurement precision. In many cases, certain real-time measurements needed to be automated. By performing some of the image processing optically, the need for expensive and specialized image processing hardware is eliminated. Finally, in experiments involving liquid bridges undergoing periodic time-dependent deformations, vibrational mode information can be directly obtained from the transform plane.

Because the liquid bridge is elevated from the surface of the optical bench by at least 20 cm, the optics are mounted on elevated optical platforms which are rigidly bolted to the optical bench. This increases the stability of the optical components. The optics are mounted on Data Optics optical rails and 3-axis carriages. The bridge is viewed in 2 orthogonal directions (Figure 3.3). In each case, the bridge is viewed by a CCD camera (Burle®, model TC351A) equipped with a 18-105 mm zoom lens. In one view, a HeNe laser is used as the light source, and in the other, an incoherent white light source with a diffuser is used as the light source. The coherent view consists of the laser (15 mW Spectraphysics Stabilite®) and a 8 micron pinhole in a spatial filter. The light is collimated before passing through the Plateau tank. The light is then subjected to high pass frequency filtering [267,268] to pass only edge information from the bridge silhouette. Light refracted by the liquid bridge is allowed to escape and does not substantially interfere with the image. Magnification is supplied by a plano-convex lens and a telephoto lens system attached to the CCD.

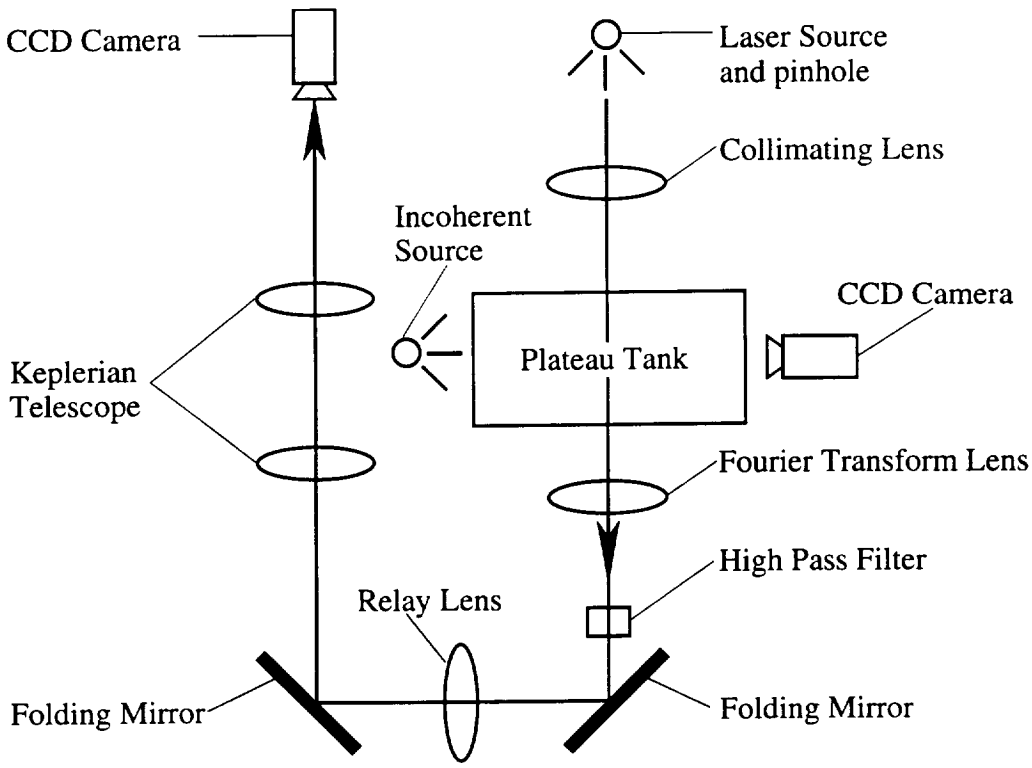

Figure 3.3. Optical layout (top view)

The images from the cameras are digitized by a frame grabber (Coreco TCX). The frame grabber can capture up to 1024 x 1024 x 8 bits for each frame. The images are currently stored and manually processed using a computer program to measure relevant parameters. Upgrading the data acquisition system will allow for real-time automatic data acquisition and image processing. The magnifications range from 10x to 700x for the coherent view, and 4x to 11x for the incoherent view.

In order to fully exploit the capabilities of the Plateau tank, it is desirable to design an optical system that can resolve features at least on the order of tens of microns. The optical system chosen is similar to a so-called "4-f system," with a few minor differences. In a 4-f system, the object plane is located a focal length in front of a convex lens, which produces the Fourier transform of the object a focal length behind the lens. This Fourier plane is located a focal length in front of a second convex lens, and it retransforms the

transform plane, producing a filtered image, a focal length behind the lens. This system, while conceptually simple, was not sufficient to meet current needs. Spherical aberration is large unless special lenses are used. Because all focal lengths are equal, there is no magnification of either the transform plane or the final image. The layout of the 4-f system has been altered to reduce these problems. By splitting each convex lens into 2 plano-convex lenses, spherical aberration is suppressed. By making the front and back focal lengths different, the transform plane can be magnified. The second half of the optical system was used to magnify the object plane. Resolution is ultimately limited by aberrations present in the Plateau tank itself. Fortunately, aberrations can be reduced to an acceptable level without expensive modification of the tank walls (e.g. using optically flat windows).

3.2.1 Alignment procedure

The complete optical system contains approximately 14 surfaces, including the two walls of the glass tank that deform due to hydrostatic pressure. In order to align so many surfaces it is necessary to eliminate all mechanical reference surfaces, i.e. optical mounts. The first step is to define the optical axis. The optical axis was true to ± 0.5 mm at 5 meters ($\theta = \pm 0.012$ seconds). The next step centers the mirrors to the optical axis.

Once the mirrors have been centered, the optical elements can be aligned. The first object to be aligned is the Plateau tank itself. The tank is the source of most of the aberrations due to the fact that it is not a precision piece of optical equipment. However, with care, the aberrations can be reduced to an acceptable level. Alignment of the tank is achieved by observing both the portions of the laser beam reflected from each surface and the deviations of the transmitted beam. By adjusting the tank, the reflections are moved until they closely coincide with the incident beam. Adjustment is achieved by (1) gross placement of the tank, including rotation perpendicular to the optical axis, (2) "shimming" the tank to adjust rotation along the optical axis, and (3) adjusting the walls of the tank to

account for non-parallel sides. A c-clamp was constructed to compensate for the sag caused by the hydrostatic pressure of the bath liquid on the walls of the tank.

When the tank is properly aligned, the optical elements are placed in the beam line, one at a time, and adjusted until reflections from the surfaces are coincident with the incident beam. Primary adjustments include translation in the X-Y plane (perpendicular to the optical axis), rotation and tilt. Usually, a small "shim" is placed to hold the desired tilt, either of the optical element, or of the entire mount. By bringing the reflections and refractions of the laser into coincidence, error due to misalignment is minimized. After the system has been aligned, the optical elements are locked in place.

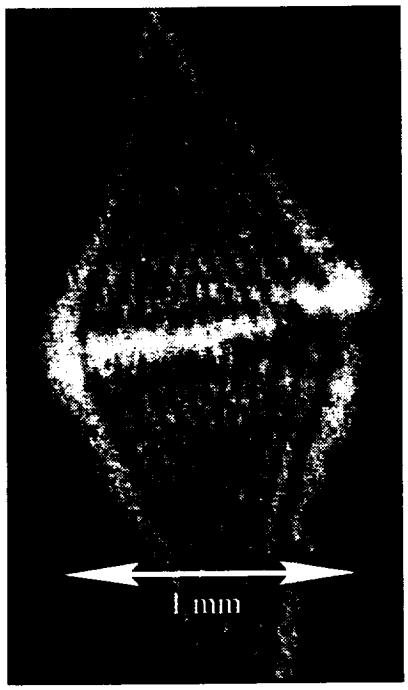

Figure 3.4. Focal spot at Fourier plane before alignment (no bridge present). Scale is approximate.

An image of the Fourier plane before aligning the tank and without a liquid bridge present is shown in Figure 3.4. This is an aberrated image of the pinhole. There is clearly some residual astigmatism and coma present. To locate the source of the aberrations, we

constructed a Michaelson-Morley interferometer to individually test each optical element. By placing either a lens or an optical flat in one of the arms, while leaving the other arm empty, the resulting interference fringes show how many waves of different aberrations are present in the optical element. A reflective ball, the center located in the focal plane of the optical element, replaces a flat mirror when a lens is in an optical path. This method of lens testing is called autoreflection, as opposed to retroreflection, which places a reflective surface at the focal plane. Autoreflection is preferred because non-rotationally symmetric errors will be preserved in the wavefront. Each lens has been quantitatively labeled and none show signs of coma or astigmatism, which are the primary non-symmetric errors. Figure 3.5 is an example of the interferogram obtained. Spherical aberration will always be present, but by carefully choosing two complementary lenses, the spherical aberration can be suppressed. Therefore, the primary source of aberrations is astigmatic and comatic curvature of the glass walls of the tank due to the hydrostatic pressure of the bath liquid. An image of the wavefront with the system elements properly aligned is shown in Figure 3.6. The astigmatism and coma have been greatly reduced. An image of the Fourier plane after all the elements have been aligned is shown in Figure 3.7. A typical image of the bridge supports is shown below in Figure 3.8. Features on the order of several tens of microns can be resolved. The edge of the support structures is clearly delineated by the dark stripe running through the bright region. This stripe is actually composed of very high spatial frequency alternating light and dark strips which the system cannot resolve.

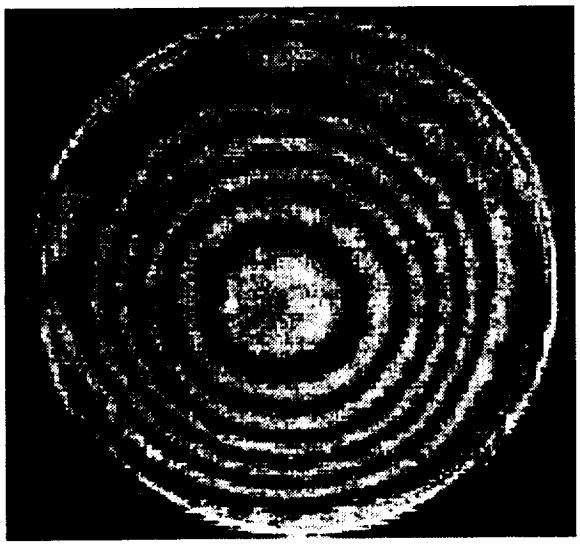

Figure 3.5. Interferogram of a lens in the optical system

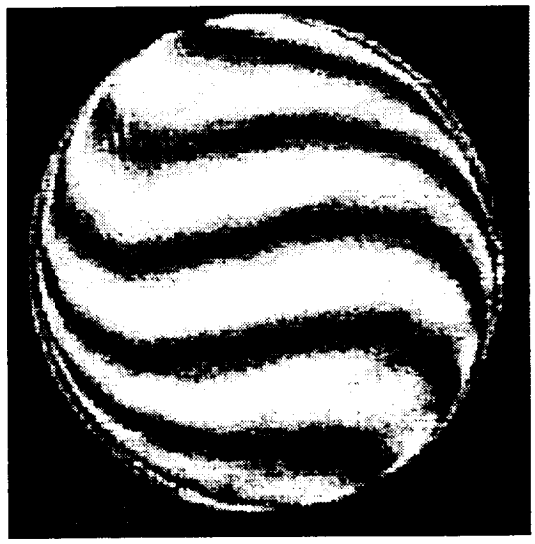

Figure 3.6. Shear interferogram of wavefront after alignment

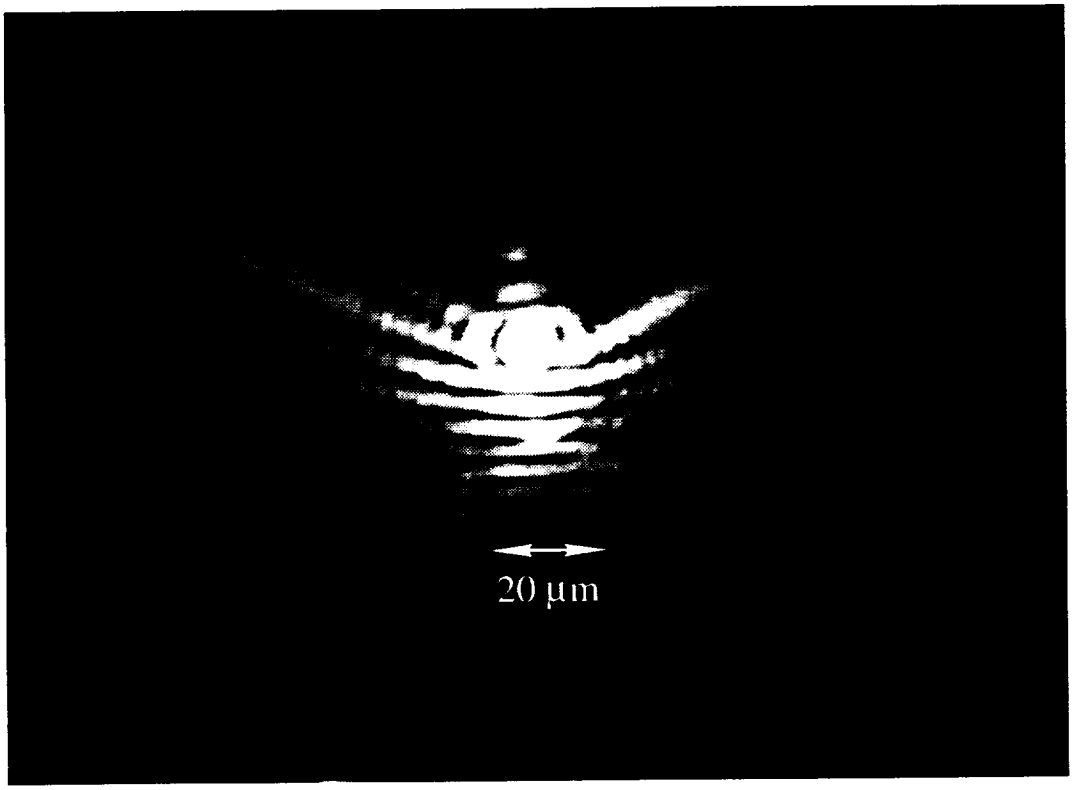

Figure 3.7. Focal spot at Fourier plane after alignment (no bridge present). Scale is approximate.

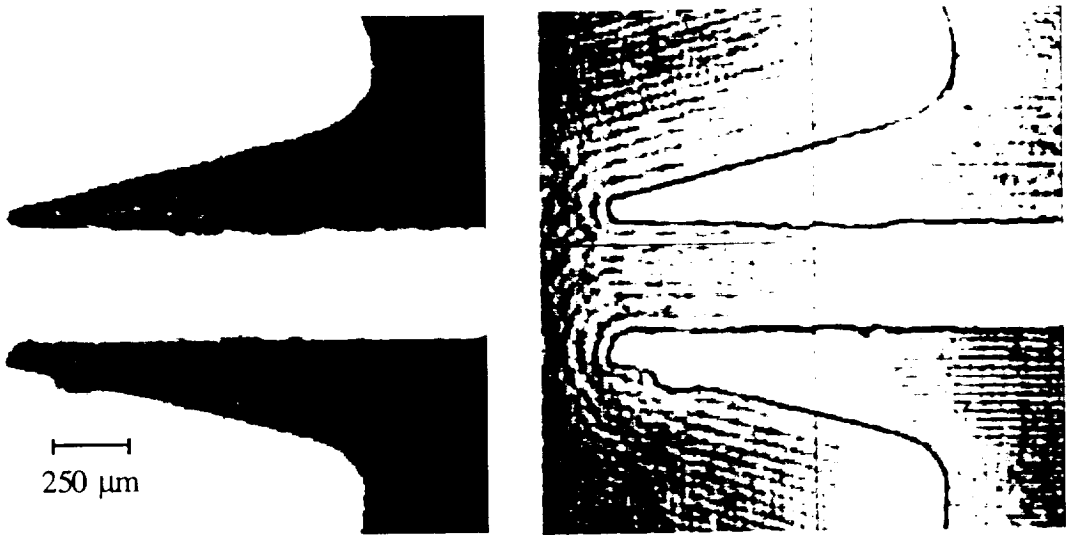

Figure 3.8. Effect of frequency filtering (no bridge present)

3.3. Materials

Table 1: materials properties. s.g. = specific gravity at 25°C, n = index of refraction at 25°C (sodium line, 589.3 nm), γ = surface tension (dyn/cm), ε = coefficient of expansion (cc/cc/°C). Sources: [1]Dow Corning, [2]3M, [3]CRC Handbook of Chemistry and Physics. *γ of 0.1 g FC-171/100 g distilled water. Note: CRC data at 20°C.

Material	s.g.	n	γ	ε
5cs silicone fluid[1]	0.913	1.3960	19.7	0.00105
100 cs silicone fluid[1]	0.965	1.4030	20.6	0.00096
Fluorad (FC-171)[2]	1.4	–	20*	–
Fluorad (FC-721)[2]	1.5	1.36	11	–
Fluorad (FC-723)[2]	1.7	–	11	–
Methanol[3]	0.7931	1.3290	22.61	–
Water[3]	0.99823	1.33335	72.75	0.00483

The materials used for the liquid bridge and the surrounding bath needed to satisfy the several constraints. Most importantly, the two liquids must be immiscible. In order to avoid issues involving hazardous materials, organic liquids such as benzene and chemical solvents such as xylene were avoided. For practical reasons we chose water and methyl alcohol as one fluid phase (see [51] for some other suggested bath liquids]). Other liquid bridge experiments have used Dow Corning series 200 fluids, a series of hydrophobic polydimethylsiloxanes available in various viscosities. These fluids have several advantages. They are, non toxic, and stable. We found, however, that silicone fluid in contact with air and a water-methanol solution for extended periods of time (for example oil floating on the surface of the bath) will polymerize. Because the interfacial energy is a difficult physical quantity to measure accurately, it is an advantage to have a value that does not appreciably change from one experiment to another. Because the silicone fluids readily adhere to any surface they come in contact with, the silicone fluid was used as the bridge fluid, rather than the surrounding bath fluid. This way the silicone is contained, and in the case of the bridge breaking, the drops of oil will adhere to the glass walls of the tank and not interfere with subsequent experiments.

The only decision left to resolve was the viscosity of the silicone oil. Because the water-methanol solution has a viscosity close to 1 cs, a silicone fluid with a viscosity of 100 cs, and another with a viscosity of 5 cs was selected. In this way regimes where the relative viscosity is large or small [62] can be investigated.

Although the silicone oil came provided with a materials data sheet from Dow Corning, much time was spent studying the behavior of the silicone fluid in contact with various materials. Because control over how the oil wet the support disks was important, disks were machined out of many different plastics, as well as aluminum (T6061), free-machining brass and stainless steel (303A). The long term behavior of the silicone oil in contact with polymethylmethacrylate (PMMA), polycarbonate, nylon 6/6, nylon 6/12, polytetraflouroethylene (Teflon), high-density polyethylene, polystyrene, polyurethane,

polyvinylchloride and Delrin was investigated. In all cases, the surface of the plastic in contact with the oil degraded over time until the oil no longer wet the surface in the presence of the water-methanol solution. The time for this to occur ranged from hours (polycarbonate) to weeks (Teflon). Concerning the metals, the brass turned the water-methanol solution cloudy in a day, and the aluminum had the tendency to polymerize the oil, transforming it into a gel-like substance in the presence of the water and methanol. Although the oil exhibited wetting problems when in contact with the stainless steel after an extended period of time (several months), the fact that the steel could be machined to a much sharper edge than the plastics led to our decision to select stainless steel as the material for the support disks. The top surface of the steel can be coated with a surfactant (FC-171) and the underside with an anti-spread fluid (FC-721 or FC-723) to enhance the contact line pinning. Alternatively, by gently abrading the surface of the support disk, the oil is exposed to a fresh surface and again preferentially wets the surface of the support disk.

3.4. Physical measurements/ calibrations

3.4.1 Calibration of a density hydrometer at various temperatures

Accurate and precise knowledge of the bath and bridge density is crucial if we are to control the Bond number at low magnitude ($Bo < 0.1$). Therefore, an experiment was undertaken to calibrate our density hydrometer over a range of temperatures. Although a pycnometer would provide much higher accuracy and precision, it is only calibrated for one specific temperature. Silicone oil was used as a density standard, and the condition of neutral buoyancy used to compare measured densities of the bath with independently measured densities of the oil. Use of the hydrometer over a temperature range (20 °C - 30 °C) is the primary concern. The hydrometer was an Ertco® density hydrometer, 13" long, with 0.0005 gradations. The rated accuracy is 2% at the standard temperature, but a substantially greater accuracy over a large temperature range was required. To take a

reading, the hydrometer was placed in a 500 ml graduated cylinder. A platinum resistance thermometer was placed in the Plateau tank. Although the lower limit of resolution of the thermometer is 0.001 °C, local temperature fluctuations forced a practical resolution of 0.01 °C.

The temperature dependence of the silicone fluid was measured independently from the hydrometer, using the Archimedes method to weigh an aluminum block submerged in the oil at various temperatures. This method gave the coefficient of expansion for silicone oil as $\Delta\rho/\Delta T = -9.56 \times 10^{-4}$ g cm^{-3} K^{-1} (see Figure 3.9). This result is less than a 0.1% difference from the published result by Dow Corning®. The Archimedes method was not used to calibrate the hydrometer directly because the hydrometer was too large for the apparatus. The Plateau tank is kept to a given temperature, within 0.01 °C, and the density of the bath is adjusted by adding either deionized water or methanol until a pulled bridge of slenderness 3.12 is stable. The bridge slenderness was chosen to be as close to the Rayleigh limit as practical. At this point, the density of the bath is nearly equal to the density of the oil, and a density measurement of the bath is taken and compared against the calculated density of the oil (see section 5.1 for more detail). The bath mixture was mixed continuously, except when pulling a bridge. Homogeneity was checked using schlieren coherent imaging. Any inhomogeneities in the bath composition create inhomogeneities in the local index of refraction, and thus, create a local lensing effect, which can easily be observed. The graduated cylinder was first filled with bath liquid, then the liquid was expelled as waste to eliminate compositional differences between the fluid in the bath and the fluid in the drain tube, or residual fluid in the cylinder. The graduated cylinder was again filled, and a density measurement taken. The ratio of calculated to measured density over a range of temperatures is shown in Figure 3.10. Within the precision of the hydrometer, the variation of temperature did not affect the accuracy of the hydrometer. The data taken by comparing the measured density of the oil

to the measured density of the bath is used to increase the accuracy of the hydrometer. Consequently, the density of the bath is known to better than 0.1%.

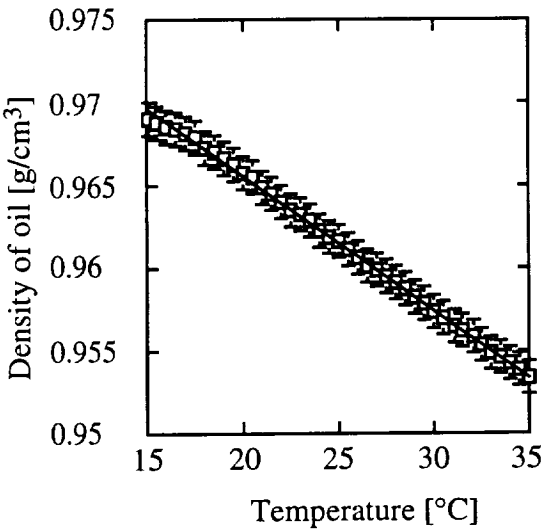

Figure 3.9. Temperature dependence of silicone oil density

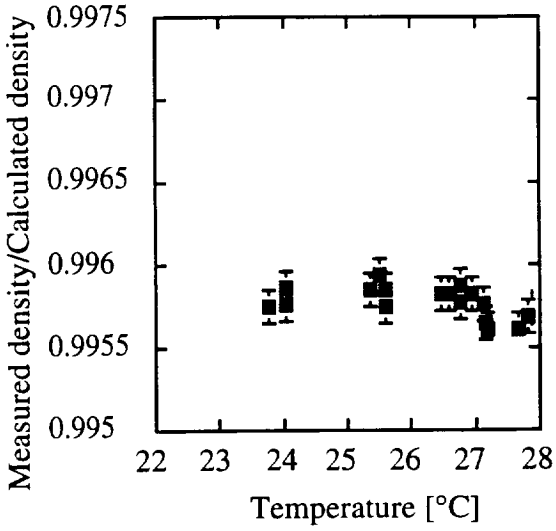

Figure 3.10. Ratio of measured and calculated density

Because the conditions for neutral buoyancy require a density difference of exactly zero, the time required to achieve exact neutral buoyancy is unacceptably long. In addition, the limit of precision of the hydrometer places a lower limit on how close to neutral buoyancy can actually be measured. Equal numbers of readings were taken with the oil slightly lighter than and slightly heavier than the bath. In this case it was found that the density difference was equal to the precision of the hydrometer. In order to ensure that the temperature of the measured fluid stayed constant over the period of the experiment, the temperature of the bath was kept close to the ambient temperature of the room. If many schlieren fringes appeared when the solution was poured back into the bath, the trial was repeated. This guaranteed that the temperature of the graduated cylinder did not significantly affect the temperature of the bath portion being measured.

3.4.2 Evaporation rates of silicone oil and bath liquid

Because the bath liquid contained a large fraction of alcohol, it was necessary to determine if the evaporation rate was large enough to significantly alter the bath density over the course of an experiment. We also wished to know if the silicone oil was volatile. In addition, we desired to know if the silicone oil was partially miscible with the bath liquid. To measure the evaporation rates of the various viscosity silicone oils, we merely filled beakers with the fluids and periodically weighed them. We measured the mass, then placed the sample in a vacuum, and weighed the sample again (see Figure 3.11). This would tell us if any water had dissolved into the silicone oil, as the water and any other volatile liquids would boil off under a vacuum. Only the lowest viscosity silicone fluid ($\mu = 0.65$) had any appreciable evaporation rate. The amount of dissolved water decreases extremely rapidly with increasing viscosity, and the silicone fluid itself does not evaporate.

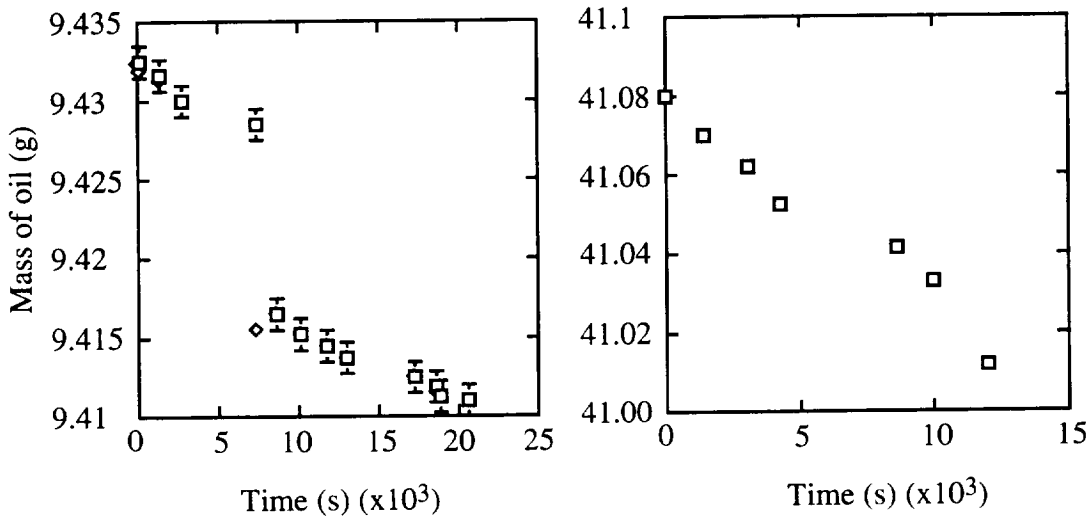

Figure 3.11. Change in mass of sample over time. (□)- before applied vacuum, (◇)- after applied vacuum

For measuring the evaporation rate of the bath fluid, the fluid was brought to a desired density, close to typical experimental values, and the tank left to sit overnight. The next day, the amount of liquid necessary to bring the bath to the density it had been previously was determined. It was found that it was necessary to cover the top of the tank.

By covering the tank with Styrofoam®, covering the through holes with plastic sheeting, and lowering the temperature of the bath, only 200-300 ml of methanol per day was needed to re-adjust the density. This represents a fractional volume change of $7.5*10^{-3}$. Thus, frequent density measurements during the course of an experiment were necessary to ensure the composition of the bath remained within acceptable ranges.

3.4.3 Interfacial tension measurements

The importance of obtaining an accurate value for the interfacial energy as possible cannot be overemphasized. The largest contribution to the error in Bond number arises from the interfacial energy. In addition, because the interfacial energy is small (roughly 15 erg/cm^2), even small values of $\delta\gamma$ produce a large error. Because the interfacial energy changes with composition (density) and temperature, it was necessary to obtain, in addition to an accurate value of γ at neutral buoyancy, the relationship between the interfacial energy and the bath density (composition).

A variety of techniques are available for surface tension measurements which vary in both accuracy and complexity [246]. There is no standard method for isopycnic liquids. We selected those methods that require a minimum of apparatus while still providing accurate values of the interfacial energy. Three methods involved the balance of gravitational and interfacial energies. These methods are the drop weight method, the pendant drop shape method, and a method utilizing the deflection of a cantilever arm in response to the interfacial energy. A fourth method compared experimental values of bridge stability to numerical computations of the stability limits of axisymmetric bridges between unequal concentric disks to obtain γ [265]

The drop weight method is perhaps the simplest method to carry out in a laboratory. Tate's law [266] is used: $W = 2\pi r\gamma f$, where f is a correction factor that accounts for the fact that not all the drop will detach from the dropping tip. The correction factor f is a function of tip radius divided by drop radius, or, since the drop volume is more

conveniently measured, $V_0^{1/3}$. In our case W, the weight of the drop, was $\Delta\rho V_0$. Correction factors for mercury in air were given by Wilkinson and Aronson [197].

The pendant drop technique is slightly more complex, but still requires a minimum of apparatus. In this case, a static hanging drop was photographed, and shape parameters directly measured from the picture. Instead of numerically fitting the entire shape, we used correction factors given by [197, 246]. In this case the surface tension is given by $\gamma = \Delta\rho g(d_e)^2/H$ where d_e is the equatorial diameter, and H is the correction factor, a function of d_s/d_e (see Figure 1.5).

The force balance method is the only method of the three that can directly measure the value of interfacial energy. A detailed explanation of the force balance apparatus is in chapter 7. By assuming the cantilever arm acts as a weak spring, measuring the deflection of the arm due to the presence of the bridge serves to measure the interfacial energy (see Figure 7.1).

The fourth method relies upon numerical calculations of the stability limits of liquid bridges held between unequal coaxial circular disks (see Chapter 5). On the lower stability boundary there is a cusp point. The value of Λ, Λ_c, at the cusp point depends sensitively upon Bo. For $\Lambda > \Lambda_c$, the bridge will neck down near the upper support disk. If $\Lambda < \Lambda_c$, the bridge will neck down near the lower disk (Figure 3.12). By adjusting the bath density until the measured value of Λ_c matches the numerically calculated value for a given Bo. The value for the interfacial energy can be then be found from the Bond number.

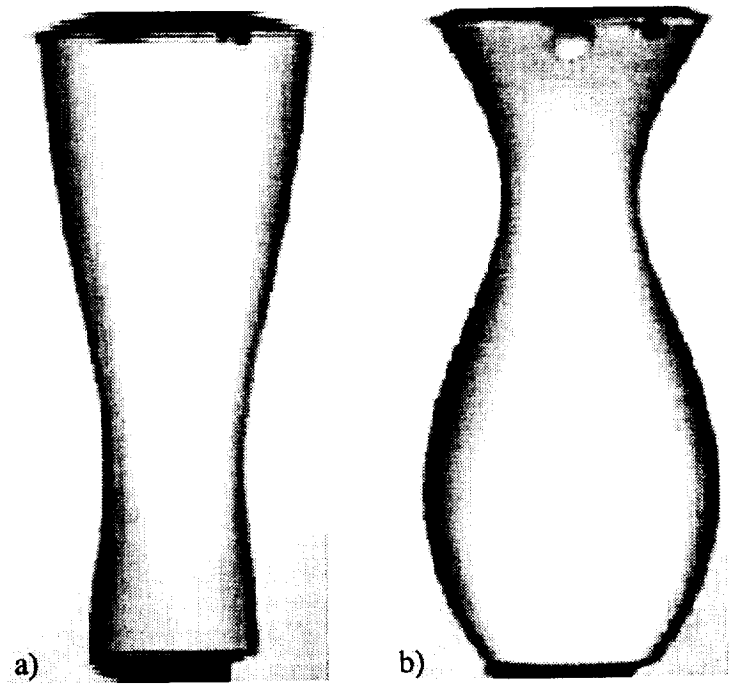

Figure 3.12. Difference in necking behavior. (a) $\Lambda < \Lambda_c$, (b) $\Lambda > \Lambda_c$.

3.4.3.1 Procedure

3.4.3.1.1 Drop weight

The same procedure was used when the silicone was heavier than or lighter than the water-methanol solution. First, a 100g solution of methanol and water was prepared by weight percent utilizing an electronic scale accurate to 0.1 mg, producing a solution accurate to 0.001%. Later, the weight percent would be converted to mol fraction, as well as a density [g/cm^3]. The receptacle, a rectangular cuvette, was first thoroughly washed with Tergazime® detergent, followed by purified water, and lastly, copious amounts of acetone. The cuvette was allowed to dry, then filled and covered with a cap which contained a small hole through which the needle could be inserted. The evaporation rate of the solution was measured over a 3 minute interval. The dropping tip was a 20 gauge needle (diameter 0.09 cm) with the end cut square to the sides. Hole integrity was ensured by inserting a wire into the hole at the time of cutting, to prevent distortion. Injection was achieved

manually via a syringe attached to a screw drive. By turning a long threaded rod, the syringe would inject fluid through plastic tubing into the needle. The syringe, tubing, and needle were connected with Luer Lock®. The needle was anchored in place by a clamp, which was attached to a sturdy base to eliminate unwanted vibration or movement. With careful manipulation, dropping times of up to 5 minutes could be achieved, ensuring maximum drop weight. Although no temperature control device was used, ambient temperature variation was small enough (approx. 0.5 °C) to ensure that the interfacial tension did not vary appreciably over the time of the experiment. The dropping tip was aligned by eye, to be near vertical. The needle was lowered into the solution, several drops were formed and weighed. The time of the procedure was noted, and evaporation rates were accounted for in the final weight. This was repeated several times to obtain a statistical average. Depending on the relative density between the silicone fluid and the methanol-water solution, either silicone fluid or solution was injected into the container. If the methanol-water solution was to be injected, The injecting syringe and tubing were emptied, the apparatus filled with a new solution which was then expelled as waste, and more solution introduced into the injection system.

3.4.3.1.2 Pendant drop

The photographs were taken using a standard 35 mm manual camera with an 85mm *f*#/1.2 lens. Image distortion was checked by imaging a grid, and was found to be negligible over the field of view occupied by the drop. Enlargements were done "in-house," with end magnifications on the order of 40x. Shape parameters were measured, and the interfacial tension calculated.

3.4.3.1.3 Cantilever arm

We examined the forces exerted by right circular cylindrical bridges with different slenderness, and measured the displacement of the lower disk from its initial position.

Silicone oil was manually injected, and the upper feed disk moved until the bridge was a right circular cylinder. The slenderness was measured directly from the viewing monitor with a set of calipers, and the displacement of the lower disk measured directly from the chart recorder. For right circular cylinders, after accounting for buoyancy, the total force on the lower disk reduces to a linear dependence upon the radius of the disk and the interfacial energy. Because the radius of the disk is a constant, the displacement of the lower disk is proportional to the interfacial energy only. This also allows us to measure the value of interfacial tension at very low Bond numbers, which otherwise must be measured by more involved techniques such as the Wilhelmy plate method, or optical methods based of eigenfrequency excitations [246].

3.4.3.1.4 Stability limits method

The density of the bath was adjusted until the experimental value of Λ_c corresponded with the known theoretical value. When the proper slenderness was reached, the density was measured with the calibrated hydrometer, and the value of interfacial energy was adjusted until the calculated Bond number was equal to +0.100. For Bo = -0.100, A slightly different method was used. Because there is no Λ_c, an slenderness near the maximum stable slenderness was used to adjust the density of the bath. Care was taken to be in a region where the value $dV/d\Lambda$ was not large, as small errors in slenderness would then cause large errors in minimum stable volume.

3.4.3.2 Results

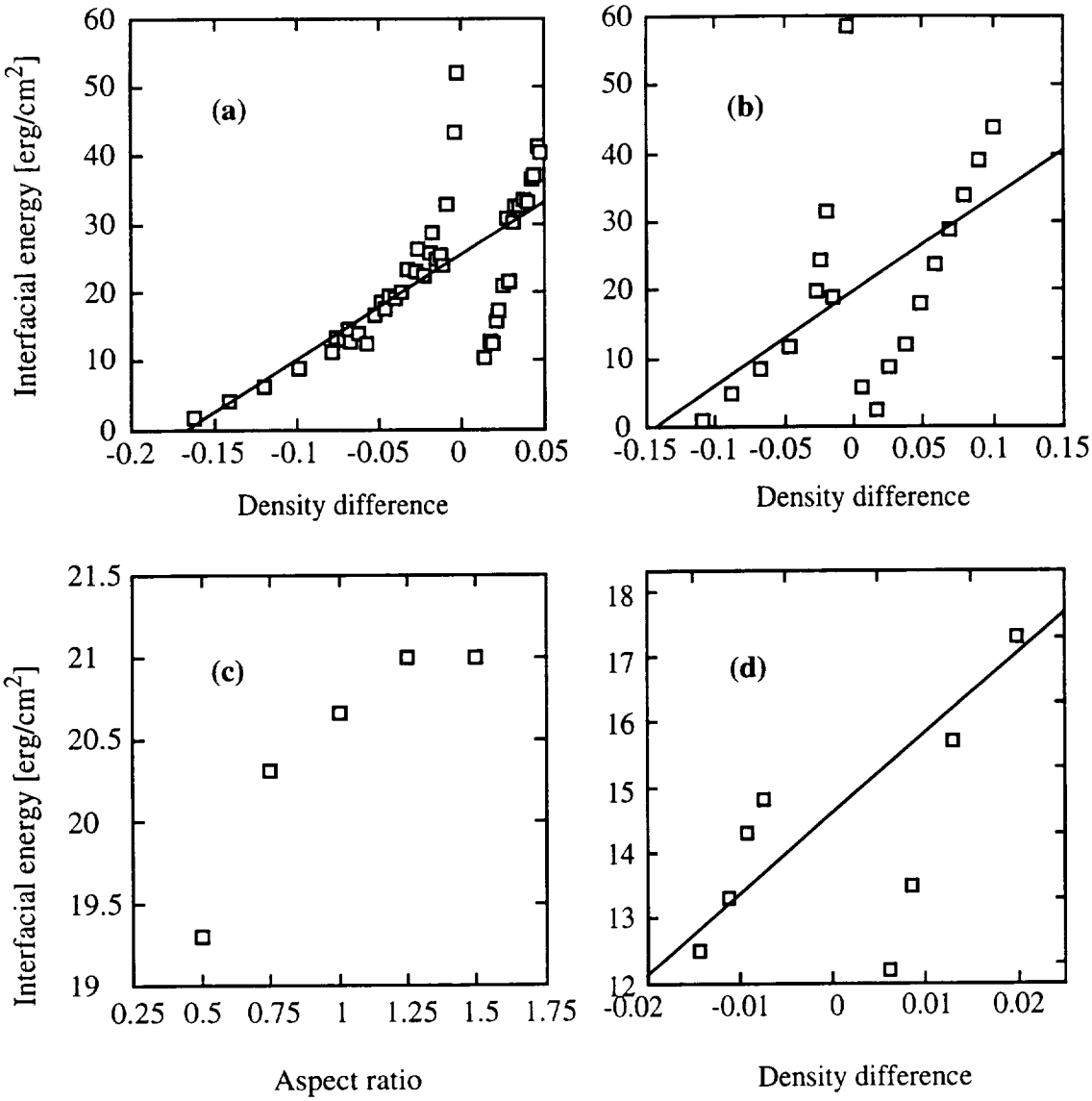

Figure 3.13. Measurements of the interfacial energy between silicone oil and a water-methanol bath. (a) 100 cs oil, hanging drop and drop weight methods. (b) 5 cs oil, hanging drop and drop weight methods. (c) 100 cs oil, force balance method. (d) 5 cs oil, liquid bridge stability method.

Results of the measurements at various concentrations of methanol are shown in Figure. 3.13 a-d. Figure 3.13 a and b shows the measured value of the interfacial energy between 100 cs and 5 cs silicone fluid and various concentrations of methanol in water

using the drop weight and hanging drop methods. Note the apparent divergence centered around $\Delta\rho = 0$. Most data points were taken using only the drop weight method. However, pendant drops were measured at various concentrations (0%, 50%, and 100% water), and the values matched those given by the drop weight methods, agreeing to within 7%. To obtain a value for the interfacial energy, a linear interpolation was used through neutral buoyancy and the affected points ignored. This gives a value of $\gamma = 14.5 \pm 0.5$ dyn/cm at Bo = 0, T = 22.0 °C for the 5 cs oil and 25.6 ± 0.5 dyn/cm at neutral buoyancy for the 100 cs oil.

Note that these methods fail near the neutral buoyancy point. This is because these methods use a balance of gravitational and interfacial energies. This is not a physical effect. Approaching neutral buoyancy, the drop size increases exponentially, with a corresponding increase in dropping times. The extreme points, those closest to neutral buoyancy, correspond to drop volumes on the order of 10 cm^3.

Figure 3.13 c shows data taken for 100 cs fluid using the cantilever arm method. Note that the data trends to an asymptotic value as the slenderness increases. This is because small errors in bridge shape at small slenderness produce large changes in the pressure as the radii of curvature are small. This method produces an interfacial energy of 21±0.5 dyn/cm (see chapter 7 for a detailed error analysis).

Figure 3.13 d shows data taken for 5 cs fluid using the method of bridge stability. Again, the data diverges around the neutral buoyancy point. This method produces an interfacial energy of 14.5 ±0.5 dyn/cm

3.5. General experimental techniques

There are three basic experimental procedures that were used for all of the experiments performed, with the exception of the force balance, which will be discussed in chapter 7. The first step in every experiment is to create a desired Bond number. The second is to create a bridge with a desired slenderness and volume. Finally, methods used

to detect when the bridge crosses a static stability limit will be discussed, as well as methods used to oscillate the supports disks for dynamical experiments.

3.5.1 Bond number control

There were different procedures employed for creating a specific non-zero Bo, and for creating a Bo as close to zero as possible. In order to create a given non-zero value for Bo, all that needed to be done was to adjust the density and/or temperature of the bath until it reached a suitable value. The values for disk radius and gravitational acceleration were constant. Previous measurements were made of the temperature dependence of the density of the silicone oil, calibration of the hydrometer, and the dependence of the interfacial energy upon composition of the bath. A Mathcad® routine was used to calculate the Bond number given a measured density and temperature of the bath, using all of the correction factors. The density was adjusted until the desired value of Bo was produced. In general, the temperature was only adjusted if it was much different from the ambient room temperature. However, adding different liquid to the bath would slightly change the temperature, so it was necessary to keep the temperature at a constant value during this procedure. After the desired (measured) density was determined, methanol and/or water were added until the density as measured by the calibrated hydrometer was correct. This method works very well for large values of Bo, $Bo > 0.01$. It is helpful to realize that if the bath solution were removed, leaving the disks in air, $Bo = 13$.

If we desired to create a Bo as close to zero as possible, it was not possible to do this by simply measuring and adjusting the density of the bath. This is because due to measurement error, the smallest directly measurable $\Delta\rho$ is 0.00025, corresponding to a Bo of 10^{-2}. (see below). To create smaller values of Bo, we used the fact that a $V = 1$ bridge of slenderness π is stable to axisymmetric perturbations only if $Bo = 0$. This allows us to be limited by the (much smaller) error of the stepper motors and a microsyringe, rather than a hydrometer and interfacial energy measurements. However, the time necessary to

create a density difference of exactly zero is unacceptably long. As a compromise, a V = 1 bridge of slenderness 3.12 was used to adjust the density difference. the density of the bath was adjusted until the bridge was stable and nearly cylindrical. This places an upper limit of Bo at $2.5*10^{-4}$. The fact that the bath volume was so large facilitates this procedure, as density adjustments on the order of one part in 10^7 are possible.

3.5.2 Creating a bridge of known Λ, V

Once the bath was brought to the desired density and the temperature stabilized by adjusting the heating element or cooling coils, a bridge of desired slenderness and volume was created. A Mathcad® routine would determine the number of steps each upper and lower support disk stepper motor would need to take, and the volume in milliliters was calculated as well. The bath stirrer, heating coil and cooling coil were turned off. This would occasionally cause the temperature to drift. The effect of a temperature change on Bond number could be calculated with the Mathcad® routine. If the change in temperature was small, a few hundrethds of a degree, the Bond number would not measurably change given the error in density measurement. The computer controlled motors would output the distance traveled (in steps), the velocity (in steps/s) and the acceleration, in steps/s^2. This information was displayed on the computer screen as part of an interface program. Each motor was capable of independently moving a certain distance at a certain velocity and acceleration. The choice of velocity is a trade-off between time taken to form a bridge and fluid flow perturbations caused by the disks moving within a viscous bath liquid. To start, the support disks were slightly separated from each other to ensure that oil was in fact flowing out of the feed disk. This small separation was measured to be on average 0.002 cm. A V = 1 bridge of slenderness 0.002 has a volume of 15 μl. Originally, oil was injected by a motorized syringe as the support disks were separated, but it was found that the deformation of the rubber tip of the plunger caused an incorrect amount of oil to be injected. Therefore, injection was performed manually with a calibrated microsyringe.

Once the bridge was created, other values of slenderness and volume could be created by moving the support disks and/or injecting or withdrawing oil. The Mathcad routine would calculate the new slenderness and volume given an input separation distance of the support disks (in steps) and a volume of oil in microliters. Figure 3.14 shows a sample path that was followed to create a bridge of an initial configuration (Λ_i, V_i) in a solid line, and the dashed lines indicate possible paths to approach the stability limit (See chapter 4).

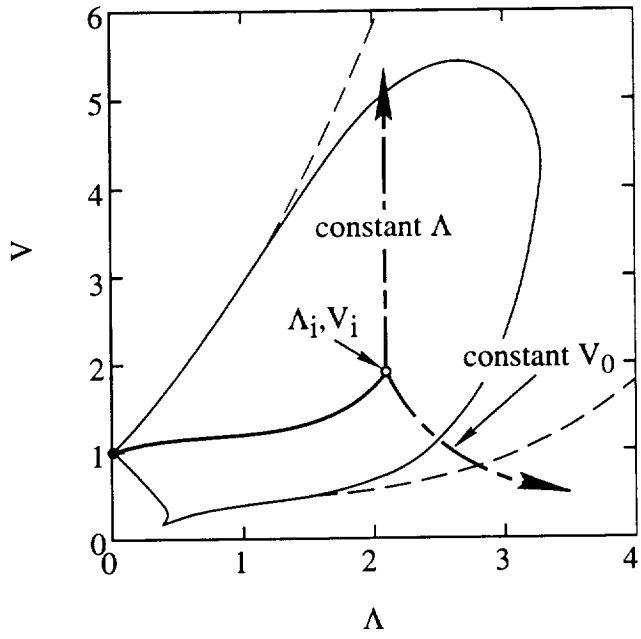

Figure 3.14. A sample path followed in Λ-V space. Thin solid line: Bo = 0.1. Dashed line: Bo = 0.

3.5.3 Dynamical procedures

The main procedure involved a sinusoidal lateral or axial oscillation of the disk supports. A computer program controlled the oscillation of the disks approximately sinusoidally by adjusting the amplitude and velocity of the rate of travel to achieve a constant acceleration at different frequencies.

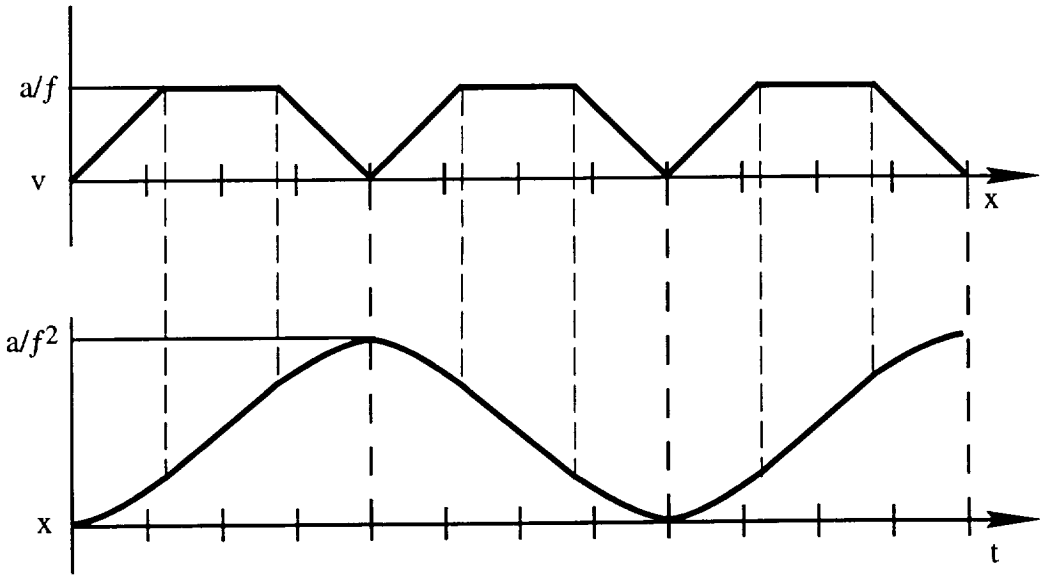

Figure 3.15. Schematic plot of motor motion. Top: velocity versus distance. Bottom: Distance versus time.

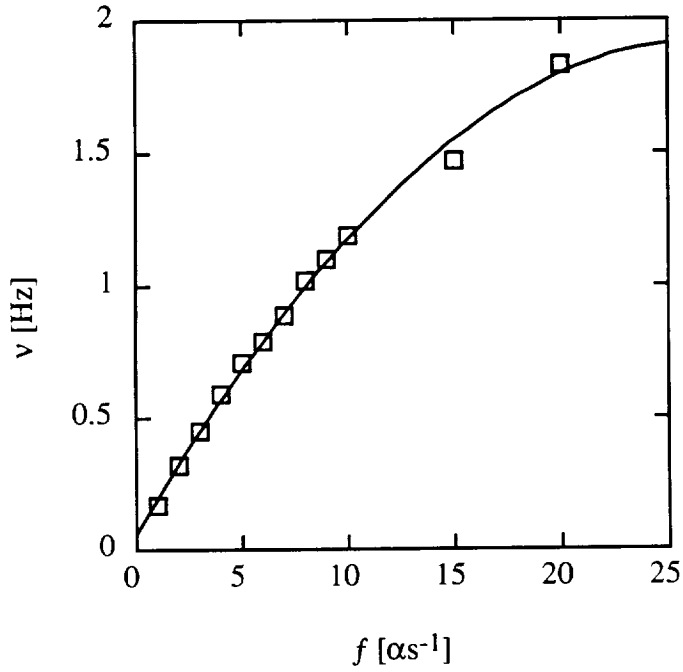

Figure 3.16. Plot of ν against f for a fixed A.

It was necessary to first calibrate the stepper motors. This is a 4-dimensional problem: given a "frequency" f and an "acceleration" a as input, calculate the true frequency ν and true amplitude A. Given input values of f and a, travel distance in units of steps and velocity in units of steps/s were calculated, $d = \alpha a/f^2$, $\nu = a/f$. The scale factor α is used to control the overall displacement range, and is held constant. The values of distance and velocity passed to the indexers. The indexers would command the encoders to move the motor a specified number of steps with a specified maximum velocity using the default acceleration/deceleration. Schematic velocity versus distance and distance versus time plots, for clarity, are shown in Figure 3.15. Calibration runs were performed by keeping either the input acceleration fixed and varying f or by keeping f fixed and varying a. Given a constant input acceleration, the relationship between f and ν is shown in Figure 3.16. Four different f's were chosen, and the true frequency measured as the acceleration varied (Figure 3.17 a-d). The frequency dependence of $d\nu/dA$ was measured as well (Figure 3.18). Lastly, the true acceleration was calculated for different input accelerations as f was fixed (Figure 3.19). Three features stand out. First, given a constant acceleration, ω tends to an asymptotic limit around $\nu = 2$ Hz. A quadratic fit of the data was used with the understanding that the fit does not apply at frequencies close to this limit. Thus, we were limited to a study of the fundamental frequency, although a first harmonic may be generated if the resonance occurs at a low enough frequency. The next feature is that the frequency does depend upon the acceleration. This dependence is weak enough to assume a linear dependence at small accelerations. We assumed the following form of the true frequency and acceleration:

$$\begin{aligned} \nu &= \nu(a, f) \approx m_1(a) * \nu(f) + c_1 \\ A &= A(a, f) \approx m_2(\nu) * A(a) + c_2 \end{aligned} \tag{3.1}$$

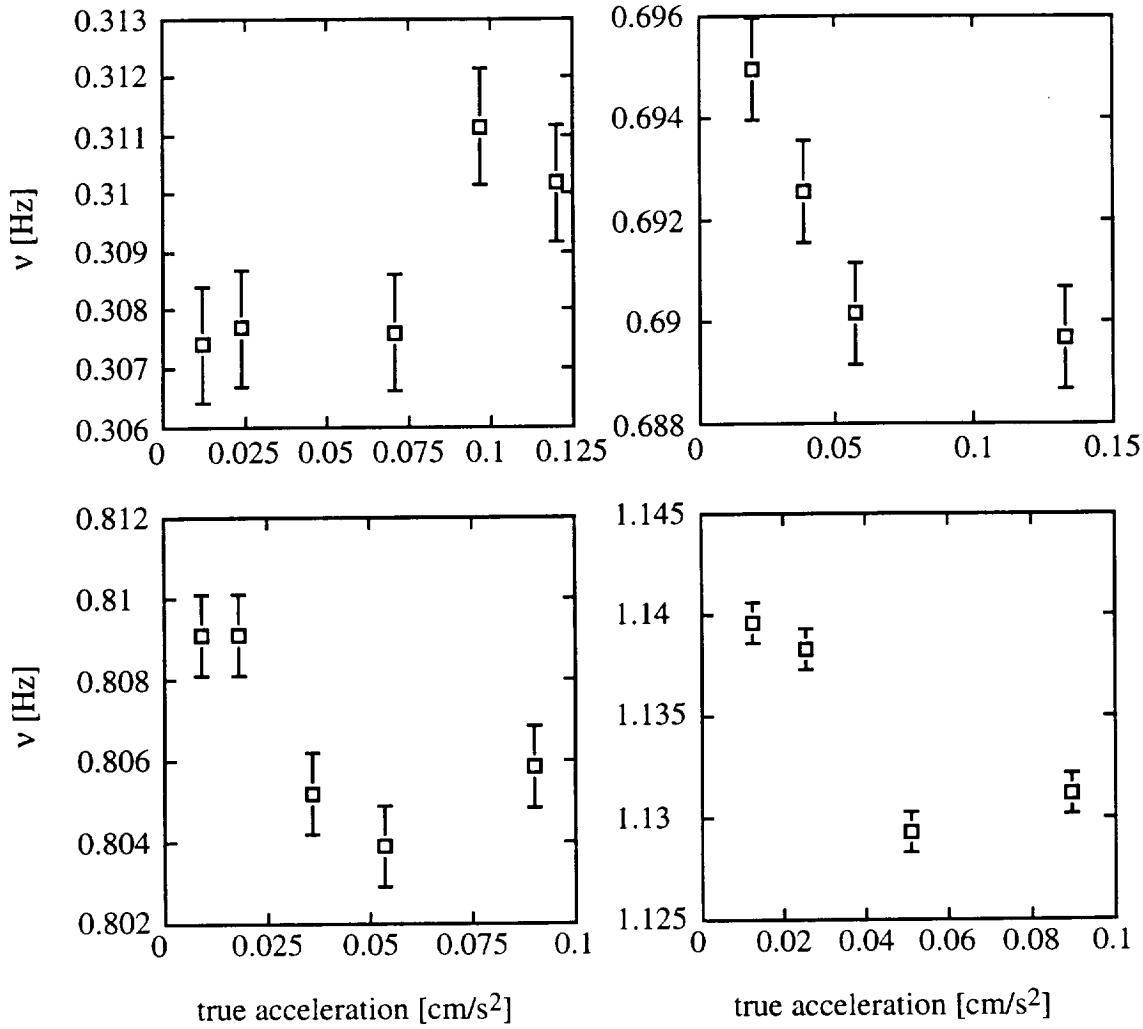

Figure 3.17. Change in ν with acceleration

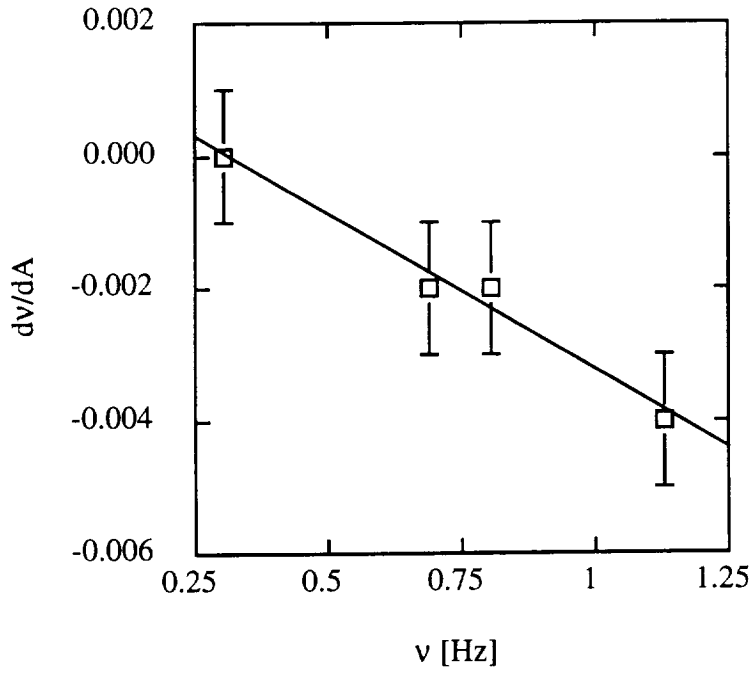

Figure 3.18. Change in dv/dA versus ν

which gives the following formulae for the true frequency and acceleration in terms of the input frequency and acceleration:

$$\nu = (-4.742*10^{-3}a + 1.488*10^{-3})[-2.509*10^{-3}f^2 + 1.369*10^{-1}f + 5.554*10^{-2}] \quad (3.2)$$

$$A = (-1.2295*10^{-3}\nu + 2.743*10^{-2})a + 3*10^{-4}$$

These can be inverted to give an input set (f,a) to create a desired (ν,A). Note that it is more important to have accurate and precise values for ν than for A for purposes of measuring the eigenfrequency.

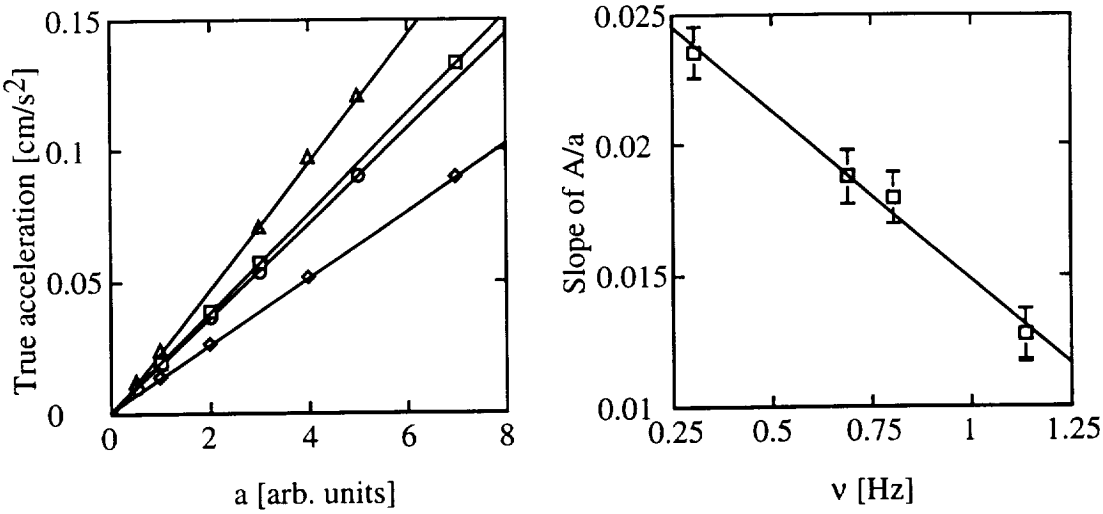

Figure 3.19. Variation of A with a and ν.

3.6. System error

Here an analysis of the systematic error present in our apparatus is presented. Some of the sources of random error are discussed as well, and the magnitude estimated. The error sources affect physical measurements/calibrations, Bond number calculations, and static and dynamic parameters of liquid bridges.

3.6.1 Density

The calibration procedure produced a calibrated instrument accurate to ± 0.00025 g/cm^3, the precision of the instrument. This corresponds to $\delta\rho/\rho = 2.5 * 10^{-4}$ at typical values of density.

3.6.2 Disk radius

The calipers used to measure the disk radius are precise to 0.02 mm. Therefore, for 1 cm radius disks, $\delta R/R = 2*10^{-3}$.

3.6.3 Interfacial energy

To check our measurement technique, the pendant drop and hanging drop methods were performed on pure silicone fluid in air. Both methods agreed well with data provided by Dow Corning. The pendant drop method tended to give a lower value of the surface tension, while the drop weight method tended to give a slightly higher value. For silicone in air, the hanging drop methods gives a surface tension value of 18.06 ± 0.54 dyn/cm for different measurements of the same drop, and 17.17 ± 0.39 dyn/cm for measurements of different drops. The drop weight method gives 21.29 ± 0.33 dyn/cm for measurements of different drops, and there is negligible error due to angular displacement. The needle tip was cut square to within 2 degrees, as measured by enlarged photographs. The eccentricity of the inner diameter of the needle was measured to be exactly zero, and the eccentricity of the outer diameter of the needle was measured to be 0.011 ± 0.007 (see Figure 3.20). Note the outer perimeter of the needle is not exactly circular. Error as a result from drop-to-drop variations is 2.28%, and error due to measurement of a single drop is 3%.

The values of γ measured in the Plateau tank were used instead of the hanging drop and drop weight values as they were representative of the actual experimental environment. For 5 cs oil, the measurement error corresponds to $\gamma = 14.5 \pm 0.5$ dyn/cm. For the 100 cs oil, the measurement error corresponds to $\gamma = 25.6 \pm 0.5$ dyn/cm.

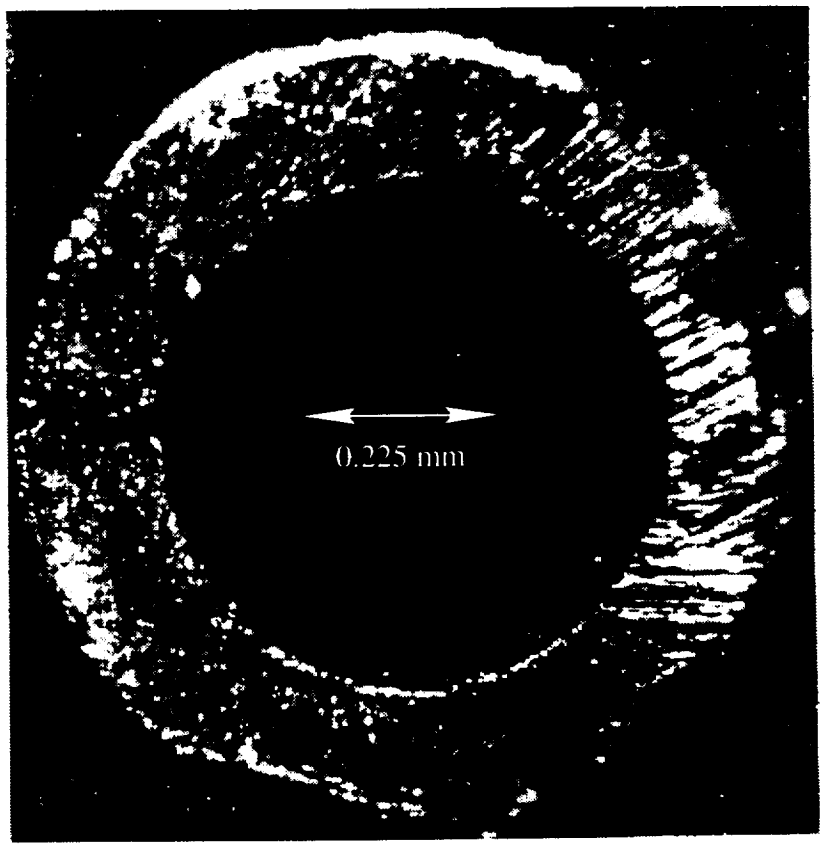

Figure 3.20. Magnified image of dropping tip.

3.6.4 Error in "g"

The accepted error for "g" is 0.5 cm/s^2, which corresponds to $\delta g/g = 5.4*10^{-4}$.

3.6.5 Bond number

The uncertainty of the Bond number is the most important to know. The error is calculated with two independent methods. The first method uses the uncertainty in density, disk radius, interfacial energy, and "g" to calculate the uncertainty in Bond number.

$$\frac{\delta Bo}{Bo} = \left[\left(\frac{\delta\Delta\rho}{\Delta\rho}\right)^2 + \left(\frac{\delta g}{g}\right)^2 + \left(\frac{2\delta R}{R}\right)^2 + \left(\frac{\delta\gamma}{\gamma}\right)^2\right]^{1/2} \tag{3.3}$$

This gives $\delta Bo/Bo = 3.45x10^{-2}$. The largest error is in interfacial energy, followed by error in disk radius, then density, and uncertainty in "g" is last. Note that this error is in many cases larger than typical experimental values of Bo. The importance of using the method of Rayleigh length bridges becomes apparent.

The method of determining the error present in this case uses the relation between maximum slenderness of a right circular cylindrical bridge as a function of Bond number to calculate the error in Bo.

$$\Lambda_{max} = \pi\left[1 - \left(\frac{3}{2}\right)^{4/3} Bo^{2/3}\right] \tag{3.4}$$

For $\Lambda_{max} = 3.12$, $Bo = 2.4x10^{-4}$. To calculate the error in Bo with this method, we need to calculate the error in Λ and V.

3.6.6 Error in Λ, V

The stepper motors provide a 48750 steps/cm displacement. Thus, the primary uncertainty in Λ is due to the error in disk radius and the error due to an initial disk separation. The initial disk separation was measured to be, on average, 0.02 mm. The stepper motors had repeatable motion as verified under high magnification. However, the smallest repeatable distance we were able to resolve, under a combination of extremely high magnification and a significant amount of post-processing with an image processing program (Matrox Inspector®), was a distance produced by 10 steps, corresponding to an error of $2.5*10^{-4}$ cm. The combined errors produce

$$\frac{\delta\Lambda}{\Lambda} = \left[\left(\frac{\delta L}{L}\right)^2_{inital} + \left(\frac{\delta L}{L}\right)^2_{motors} + \left(\frac{\delta R}{R}\right)^2\right]^{1/2} \tag{3.5}$$

which is equal to $\delta\Lambda/\Lambda = 1.72 * 10^{-3}$ for $\Lambda = 3.12$. The uncertainty in oil injection depends on which syringe was used. For the small (50 µl) syringe, the uncertainty is 0.5 µl, which corresponds to $\delta V/V = 2.04 * 10^{-4}$ for a $\Lambda = 3.12$, V = 1 bridge. For the larger (500 µl) syringe, $\delta V/V = 2.04 * 10^{-3}$. From Equation 3.4, this corresponds to an error of $\delta Bo/Bo \approx 7x10^{-5}$. Thus, by forgoing measurement of the density, reliable Bond numbers approaching zero can be created.

3.6.7 Optical aberrations

Figure 3.21. Magnified portion of a 1956 EIA resolution target. Approximate magnification of 35x.

A complete measurement of the MTF of the optical system was not performed. However, some rudimentary information can be extracted from the wavefront and from two resolving power tests performed on an EIA resolution target 1956 (Figure 3.21) and an electroformed sample from Metrigraphics® (Figure 3.22). The focal spot and

wavefront indicate the presence of coma and astigmatism. At 1 λ of defocus, the system was able to resolve up to approximately 800 TV lines of the EIA target. The electroformed sample from Metrigraphics® provided arrays of round holes, ranging in diameter from 0.254 mm to 0.00254 mm, and a 38.1 line per mm scale. The optical system was able to clearly resolve an array of 0.0254 mm diameter holes as well as the linear scale. It should be mentioned that the hole spacing is many times greater than the hole diameter.

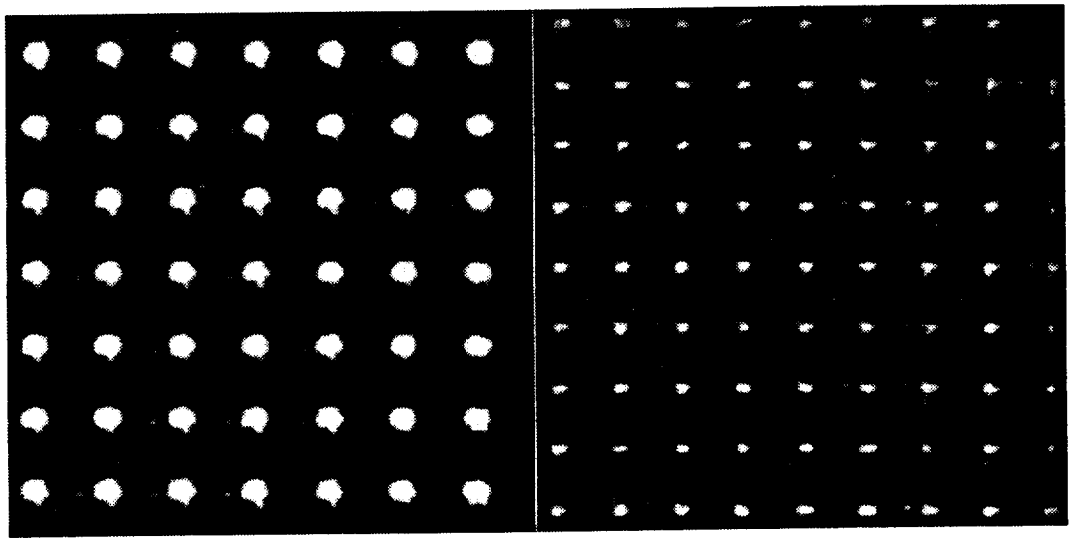

Figure 3.22. Images of electroformed holes. Left, hole diameter d = 0.0508 mm. Right, d = 0.0254 mm. The "missing hole" in the upper right corner is a hole of d = 0.00254 mm, beyond the resolution of the system.

We can estimate system performance from the above information. The diffraction-limited cutoff frequency for the transform lens is given in [267] by

$$f_c = \frac{l}{2\lambda d} \tag{3.6}$$

where l is the lens diameter, d is the focal length, and λ is the wavelength. The cutoff frequency is 133.79 cycles/mm. The first zero of the Hankel transform corresponding to a

hole diameter of 0.0254 mm is at 48 cycles/mm, and the second zero is located at 87.8 cycles/mm.

3.6.8 Error in dynamic variables

There are two quantities that need to be assessed: the disk support motion and the contact angle measurement.

To obtain the true information about disk support motion , it would be necessary to place a small accelerometer on the disk supports. As an alternative, we examined the output from the encoder, which may or may not directly correspond with the actual disk support motion. The disk supports are assumed to be rigidly coupled to the linear tables. A sample Fourier transform of encoder data is shown as an example in Figure 3.23. Although there are some higher frequency components, the effect is negligible on the experiments.

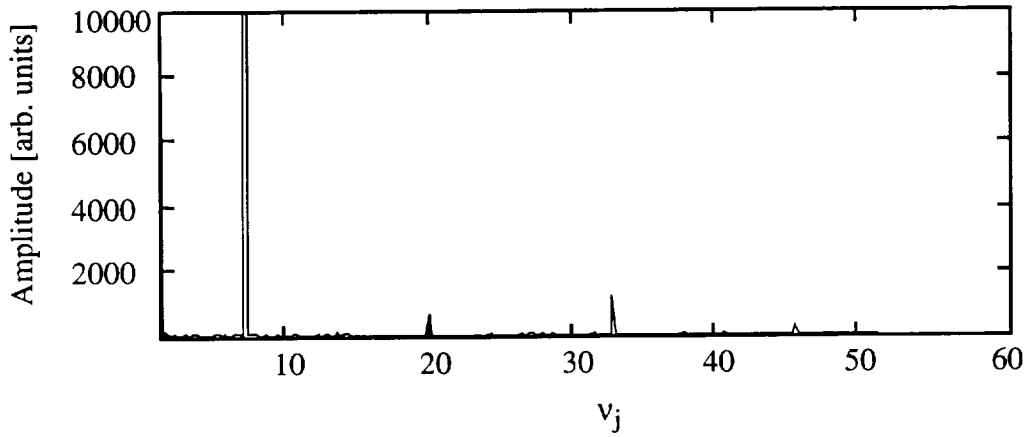

Figure 3.23. FFT of encoder output data

Error in the frequency was assessed by comparing predicted true frequencies to actual true frequencies. The timing circuit of the computer would output the amount of time taken per one-half period. This was determined from communication between the

motor and the encoder. The encoder would give a time interval between successive motor stops. The FFT of encoder output indicates that this corresponds well to a measure of one-half of a period. The predicted and measured frequencies corresponded exactly, within the resolution of the timer. This comparison gives an upper bound of the frequency error at ±0.001 Hz, the resolution of the timer mechanism.

The contact angle measurements were performed many times to minimize the amount of measurement error. By measuring the angle manually, with a protractor, the error in contact angle $\delta\phi/\phi = 6.25*10^{-3}$ for typical values of ϕ. By measuring the angle with an image processing program (Matrox Inspector®), the error can reduced to $\delta\phi/\phi = 1.11*10^{-3}$.

Chapter 4

DETERMINATION OF THE STABILITY LIMITS OF LIQUID BRIDGES HELD BETWEEN EQUAL COAXIAL SUPPORT DISKS

Axisymmetric bridges with pinned contact lines are perhaps the best studied subset of the general class of liquid bridge problems (see [15, 24-29, 51-134, 173]). In this chapter experiments that were performed using coaxial disks of equal radii (K = 1) will be discussed, and in chapter 5 experiments involving coaxial disks of unequal radii ($K \neq 1$) will be discussed.

The first series of experiments measured the static stability limits of axisymmetric bridges held between coaxial disks of equal radii for various values of Bo. Then the bifurcation that results as a weightless bridge crosses the maximum volume limit was investigated in more detail. These experiments, and the experiments in the next chapter, were performed to analyze the influence of support geometry on liquid bridge stability.

4.1. Introduction

One of the first experiments performed was a verification of the stability limits of axisymmetric liquid bridges held between equal coaxial circular disks. These limits have been most completely determined theoretically by Slobozhanin and Perales [118] for axisymmetric, nonaxisymmetric, and contact line perturbations. There are two major reasons why this experiment was chosen first. Firstly, verification of such a well-

established theoretical study allowed the accuracy of the apparatus to be measured. Secondly, this relatively simple experiment serves as a first step toward more complex experiments, such as a determination of the eigenfrequencies of axisymmetric bridges (see chapter 6). The theoretical foundations for the experimental work will be briefly reviewed.

Figure 1.4 shows a portion of the stability region for Bo = 0 (dashed line) and the entire stability region for Bo = 0.1 plotted in the Λ-V plane. A bridge lying on segment OC of the stability limit is most susceptible to nonaxisymmetric perturbations of the bridge shape. On the segment CD, the bridge is susceptible to axisymmetric perturbations of the bridge shape, and on segment OD, the bridge will lose axisymmetric stability by contact line depinning [118]. As Bo increases, the region of stability covers a smaller region of the plane, but the regions are nested within each other, and there are no intersections between curves of different Bo (Figure 4.1). Behavior of the bridge in a neighborhood of the point C, the transition point from axisymmetric to nonaxisymmetric critical perturbations, and the behavior of the bifurcation as a bridge crosses the maximum volume limit (segment OC) are the topics studied here.

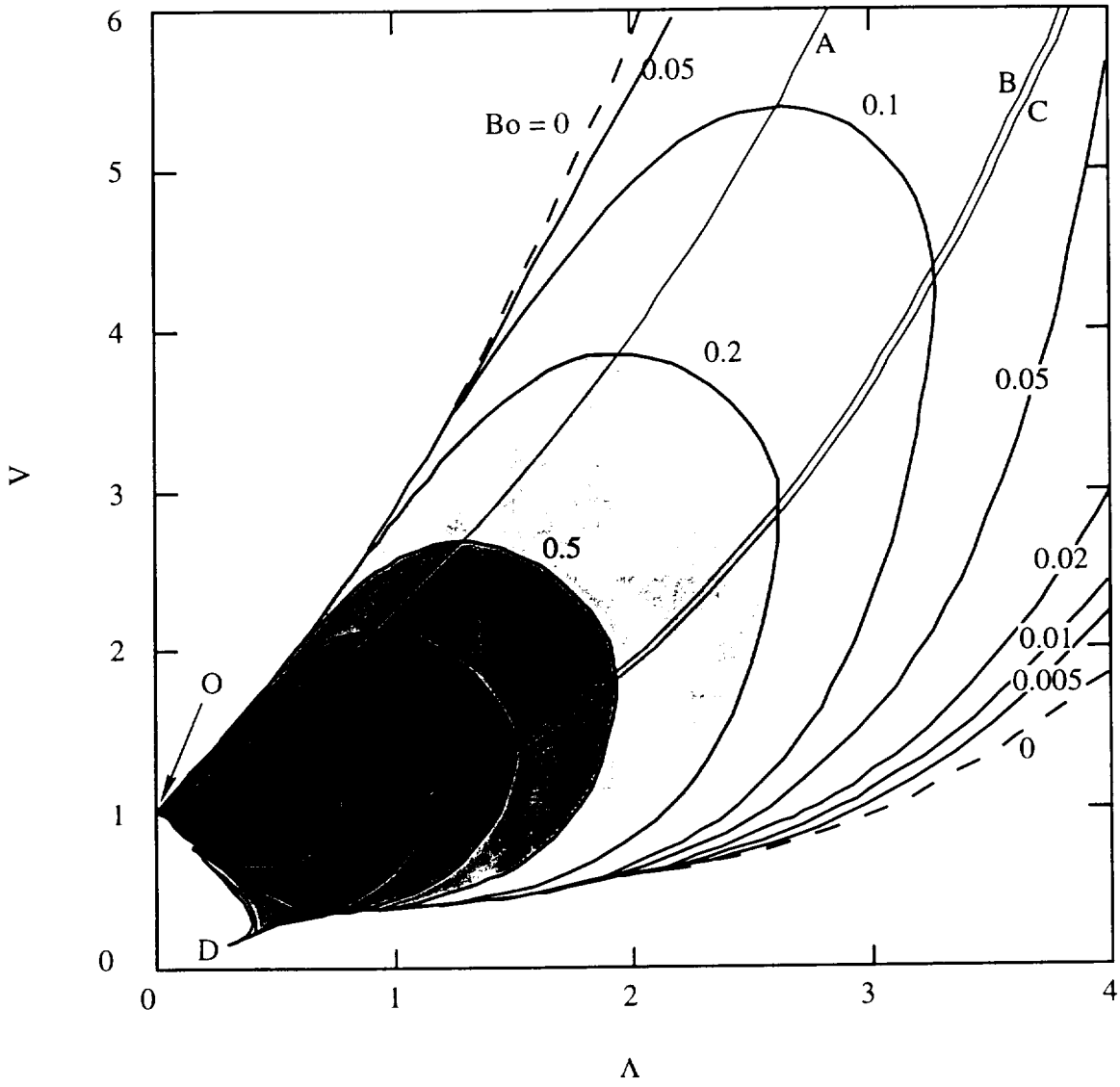

Figure 4.1 Stability regions for different values of Bo (from [118]). The curve C shows the locus of the transition points between axisymmetric breakage and nonaxisymmetric deformation of a neutrally stable bridge.

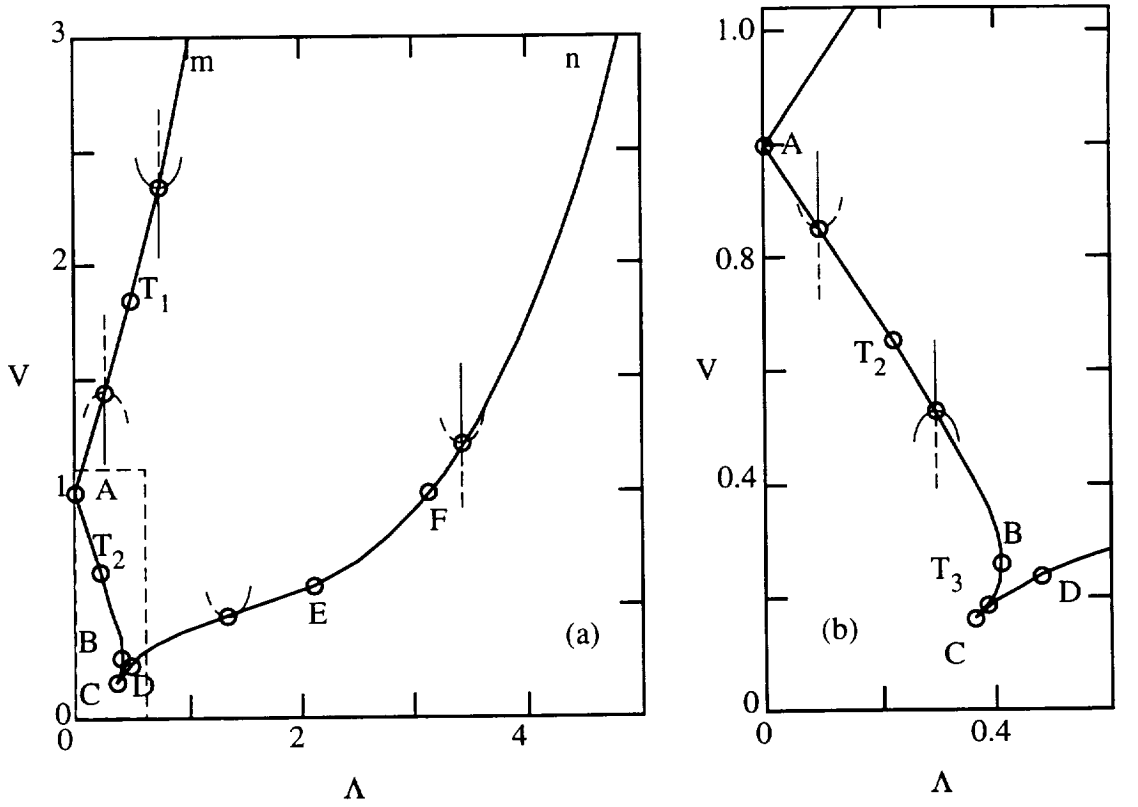

Figure 4.2. Bifurcation diagram for weightless liquid bridges (from [265]). Stability boundary for axisymmetric states (a) and detail (b). Inserts show typical bifurcation diagrams. An exit from the stability region results in: breaking (across the boundary branch CDEFn); continuous transition to stable nonaxisymmetric states (across the segments T_1m and T_2BT_3); discontinuous transition (across the segments T_1AT_2 and T_3C) .

The bifurcation of the solutions of the nonlinear equilibrium problem of a weightless liquid bridge with a free surface pinned to the edges of two coaxial circular disks of equal radii has been examined (see Figure 4.2). Recall that given a stable axisymmetric configuration, small changes in either Λ or V will in general provide a unique, continuous extension into another axisymmetric stable state. However, if the initial state lies on the stability boundary, the uniqueness of extension is violated and the equilibrium state bifurcates. Previous work has analyzed the bifurcation along the boundary segment corresponding to axisymmetric critical perturbations (segment Cn) [74, 99, 105, 136, 142, 146]. The bifurcation behavior in the neighborhood of the stability

boundary for axisymmetric equilibrium states with emphasis on the maximum volume boundary segment (segment Am) corresponding to nonaxisymmetric critical perturbations [265] has been studied. Along the maximum stability limit, depending upon the slenderness, the loss of stability with respect to nonaxisymmetric perturbations for weightless liquid bridges results in either a jump or a continuous transition to a stable nonaxisymmetric shape. If $\Lambda < \Lambda_c$ (segment AT_1), the bifurcation is subcritical (jump transition). If $\Lambda > \Lambda_c$ (segment T_1m), the bifurcation is supercritical (continuous transition). The numerically calculated value of the slenderness where this occurs is $\Lambda_c = 0.4946$ [265].

4.2. Experimental

4.2.1. Locating the static stability limits

To determine the stability limits a bridge was created with an initial slenderness Λ_i and volume V_i (see section 3.5.2). Then either V_0 or Λ of the bridge was changed in a quasi-static way until the stability limit is reached (see Figure 3.14). This method was used for numerous starting configurations, as well as different Bond numbers. In this way, the stability region for a given Bond number was mapped out point by point. The Bond numbers chosen were Bo = 0.002, 0.054, and 0.089. In addition, for a particular Bond number, it was desired to investigate the behavior of a bridge in a neighborhood of the transition point between axisymmetric and nonaxisymmetric critical perturbations. A Bond number of 0.089 was chosen.

It is necessary to understand that these stability limits are static stability limits. That is, the bridge is stable to infinitesimal perturbations only. Injecting a finite amount of oil does not always meet this criteria, and neither does finite movement of the support disks. However, the bridge cannot be initially created at the stability limit. Therefore, a bridge well inside the stability region would be created, and the bridge slowly brought to the limit. More specifically, starting from $\Lambda = 0.002$, $V = 1$, a path in the region of stability far from

the margin would be followed to create a bridge with the approximate slenderness and volume. This bridge would still be stable against perturbations that can be large. Then, Λ and V_0 would be changed in decreasing finite amounts to bring the bridge as close to the stability limit as possible. As the bridge approached the limit, the time taken between successive changes in Λ or V_0 increased to approximately 3 minutes, to allow the perturbation caused by deforming the bridge to decay. Smaller and smaller increments of disk displacement and smaller and smaller amounts of oil were added or subtracted until the bridge lost stability. The final $\delta\Lambda/\Lambda$ was approximately 0.1% and $\delta V/V$ was approximately 0.5%.

Locating the maximum volume stability limit was significantly more difficult than locating the minimum volume limit. It is not trivial to observe the loss of stability to a stable nonaxisymmetric shape (see Figure 4.3 a-j). The change in shape from a rotund axisymmetric shape to a rotund nonaxisymmetric shape is very slight, and there is no guarantee that the axis of maximum deformation will occur in a convenient plane of observation. In order to compare one bridge to another, the bulge must be in a consistent location. However, as mentioned above, this should not occur naturally. Small amounts of misalignment between the upper and lower support disk lead to premature loss of axisymmetric stability. The bridge can never be truly axisymmetric if the support disks are not axisymmetric. It is possible to know if the misalignment of the disks are more of a perturbation to the bridge shape than allowed by noting if the bridge consistently loses stability to a final nonaxisymmetric configuration with a fixed orientation in space. This was never observed. This indicated that the disks were properly aligned. Very sensitive methods of detecting the shape disturbance had to be developed, and the bridge and bath had to be completely isolated from all external disturbances, including vibrations and air currents from the air conditioning system. Thus, the optical table was floated on

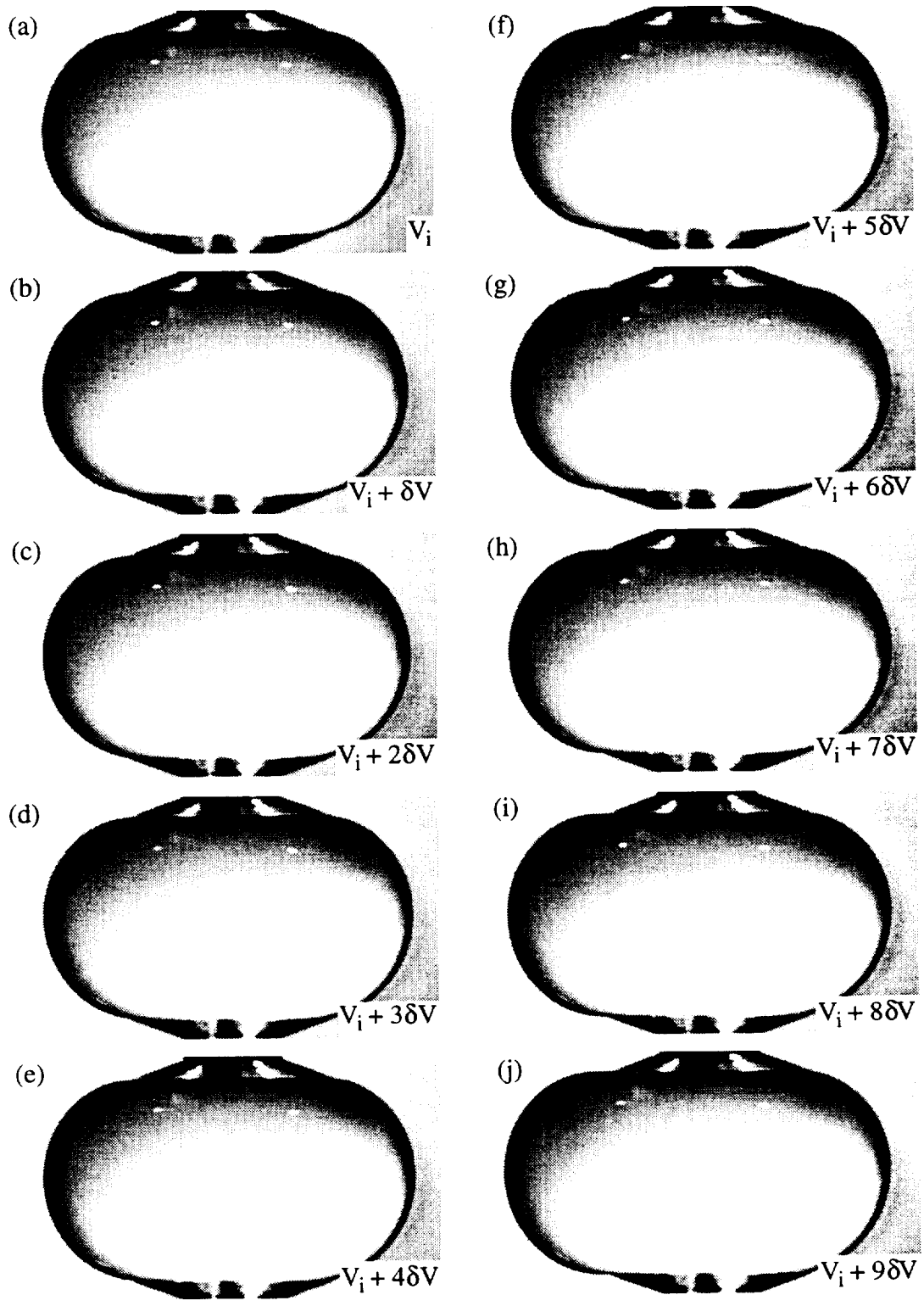

Figure 4.3. Loss of stability to a nonaxisymmetric perturbation. $\Lambda = 1.02$. $V_i = 2.82$, $\delta V = 0.095$, $V_c = 2.83$, Bo $\leq 10^{-4}$.

compressed air and the air conditioning system was turned off while the experiment was in progress. Various methods were tried to unequivocally determine the loss of stability. One method measured, under high magnification, the deformation of a bridge relative to a fixed reticule. The other method compared the centerline of the bridge to the centerline of the disk supports under lower magnification. Both have distinct advantages and disadvantages, as discussed below.

4.2.1.1. Shape deformation

This method is more precise and sensitive to changes in the bridge shape, but because the experiments are done at high magnification, the entire bridge could not be imaged. It was thus difficult to determine when the bridge was in fact axisymmetric. Sample images are shown in Figures 4.4 and 4.5. Figure 4.4 contains two images of a bridge of slenderness 0.45 separated by a $\delta V = 0.02$. Figure 4.5 consists of four images of a bridge of slenderness 0.55 each separated by $\delta V = 0.02$. Although there is a clear qualitative difference in the behavior of how each bridge deforms in response to small changes in volume, these images do not provide quantitative data. It is clearly impossible to determine which of the bridges are axisymmetric. The next approach attempted to quantify the deformation of the bridge shape by identifying the location of maximum deformation. First the bridge was brought near the upper stability margin, making sure the bridge remained axisymmetric. Then the magnification of the bridge was greatly increased. The magnified image of the bridge was moved so that a reticule intersected the bridge outline (see Figure 4.6 for a schematic). The distance between the fixed reticule would decrease with small additions of oil until the stability limit had been reached. Then, as the bridge crosses the stability margin, a bulge forms opposite the section of the bridge being imaged. When this occurs, the addition of oil caused the distance between the bridge silhouette and the reticule to increase. The difficulty remained that the maximum deformation may not occur in the plane of observation. To overcome this, the supports

were slowly rotated until the distance between the bridge silhouette and the reticule was a maximum. At this point, the bulge is located directly opposite the imaged side. Several more volume increments were added to follow the shape evolution near the maximum volume limit. The volume of the bridge was then slowly decreased in small decrements of oil. Small withdrawals of oil caused the measured distance between the bridge and the reticule to decrease until the stability limit was crossed, and then small withdrawals of oil caused the distance to increase again. This method was chosen because the rate of change of deformation versus volume will always pass through zero at the stability margin. By contrast, if the bulge side was used at the reference, the rate of change of deformation with volume increment would not indicate clearly when stability was lost.

Using this method the question of shape hysteresis could be studied. Given a general subcritical bifurcation, hysteresis is usually observed in the independent variable (see, for example, [269]). This fact is often used to great effect in optical, magnetic, and mechanical systems. However, hysteresis in bridge shape has not yet been observed [142, 267, and it was not observed here either. This question is still unresolved.

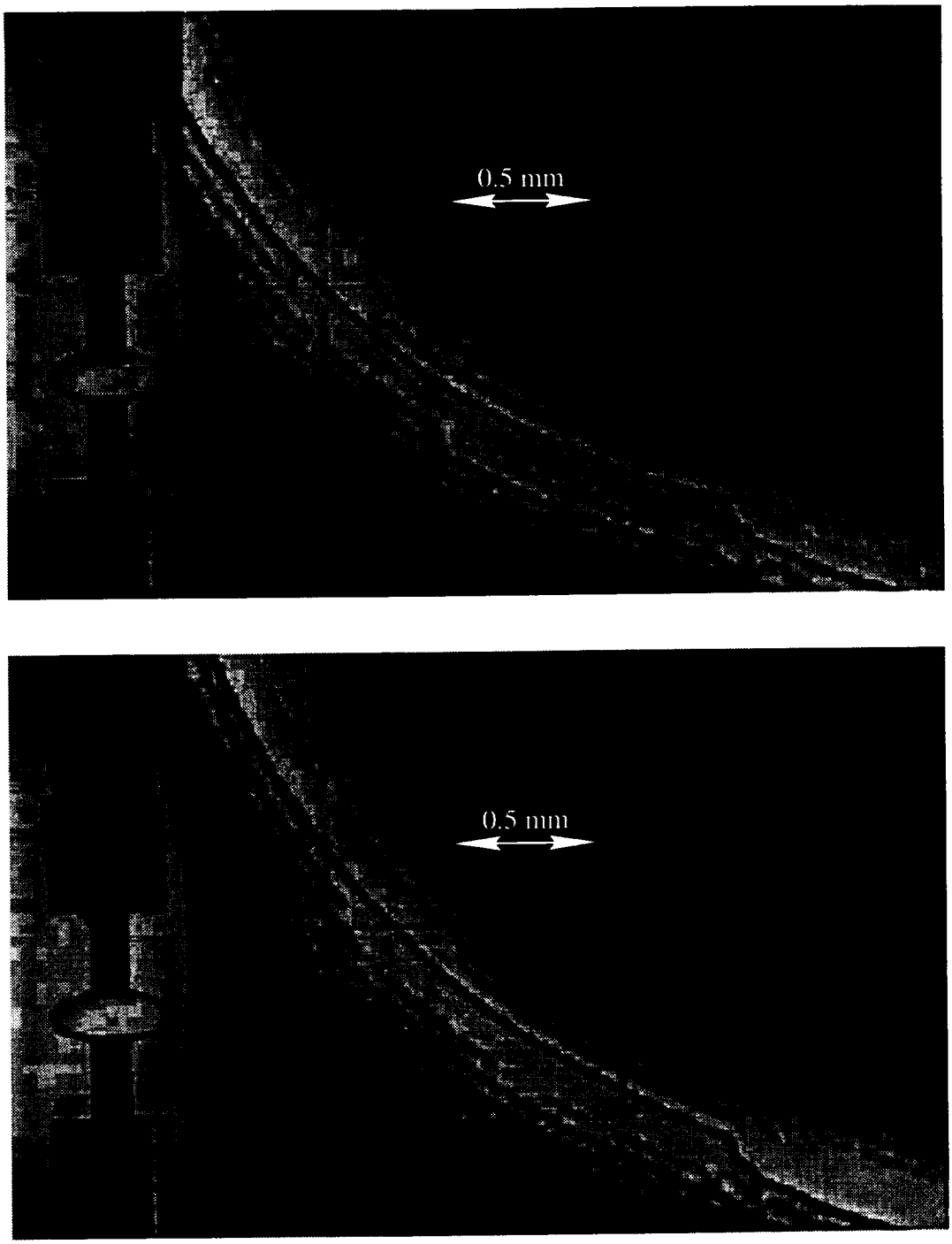

Figure 4.4. Nonaxisymmetric loss of stability, $\Lambda = 0.45$. (top): V_i. (bottom): $V_i + 0.02$. Scale for magnified portion is approximate

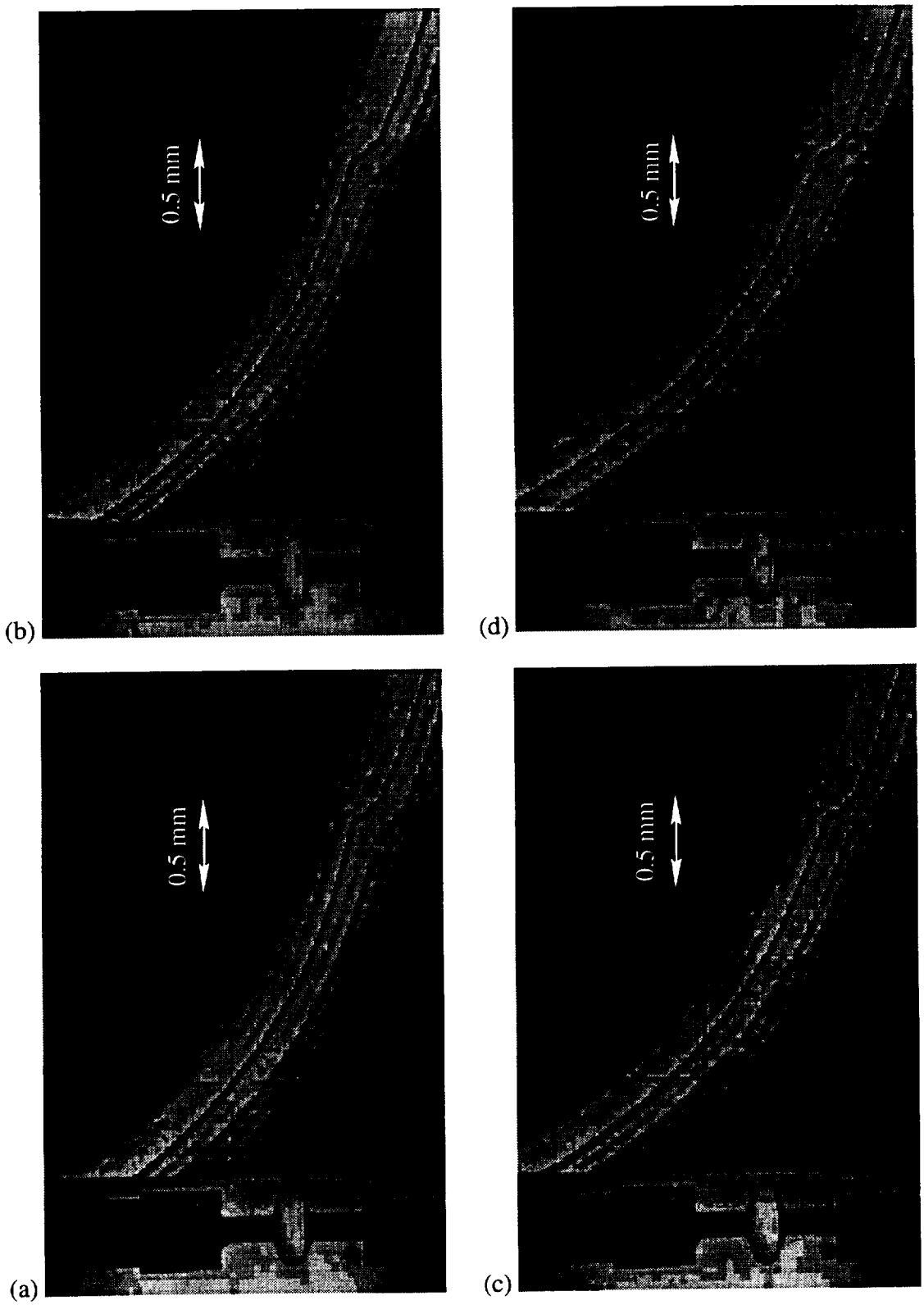

Figure 4.5. Nonaxisymmetric loss of stability, $\Lambda = 0.55$. (a): V_i. (b): $V_i + \delta V$. (c): $V_i + 2\delta V$. (d): $V_i + 3\delta V$. $\delta V = 0.02$. Scale in magnified portion is approximate.

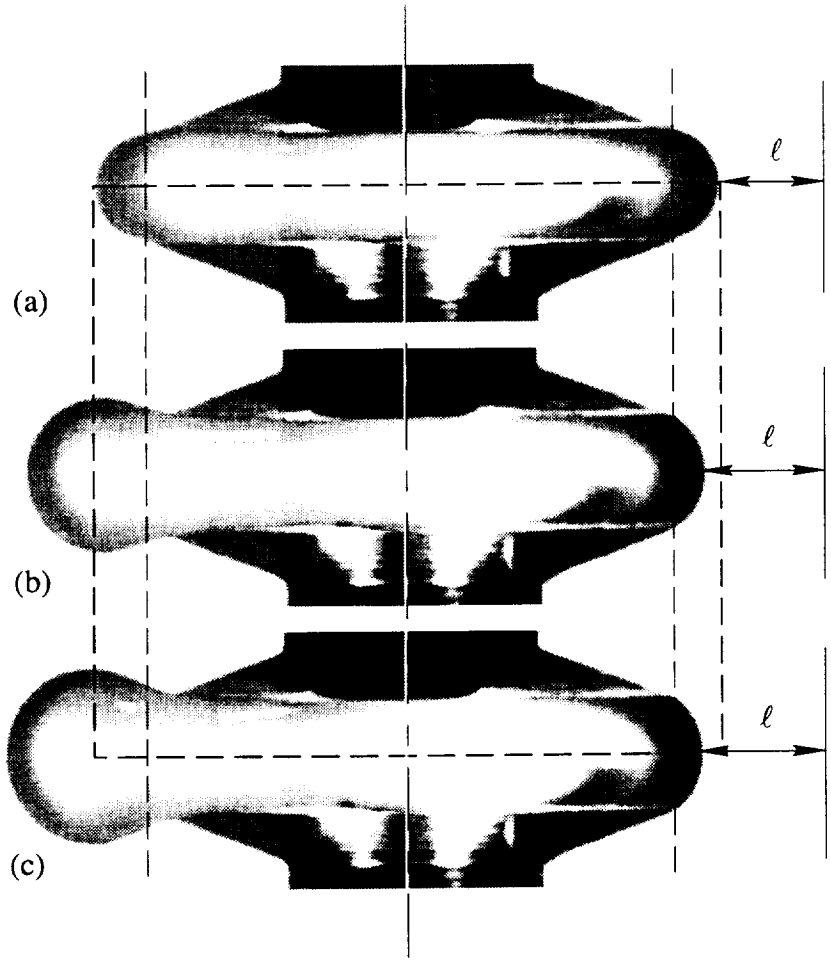

Figure 4.6. Schematic of shape deformation method of measurement. $\Lambda = 0.225$, $V_i = 1.31$, $V_c = 1.33$, $\delta V = 0.025$, $Bo \leq 10^{-4}$.

4.2.1.2. Centerlines

A bridge was formed and oil added by a microsyringe. At each addition of oil, five intensity scans of the bridge image were taken, one through each of the disk supports and the other three through the bridge. The center of the supports and of the bridge were determined by locating the edges of the features in the scan line (Figure 4.7). If the centerpoints coincide, the bridge is assumed to be axisymmetric, and if there is a difference greater than the measurement error (2 pixels) then the bridge is assumed to be

nonaxisymmetric. The initial volume of oil in between the disk supports is taken into account by assuming a right circular cylindrical bridge of slenderness 0.002. (0.002 is the average initial gap of the disk supports). This method provides a means to measure the critical volume V_c at an extremely high level of precision.

This method was not quite as accurate as the previous method, but we were able to image the entire bridge by using a moderate amount of magnification. The main advantage to this is we were able to quickly and easily determine if the bridge was axisymmetric. The method of comparing centerlines produced similar results to the results obtained with the shape deformation method.

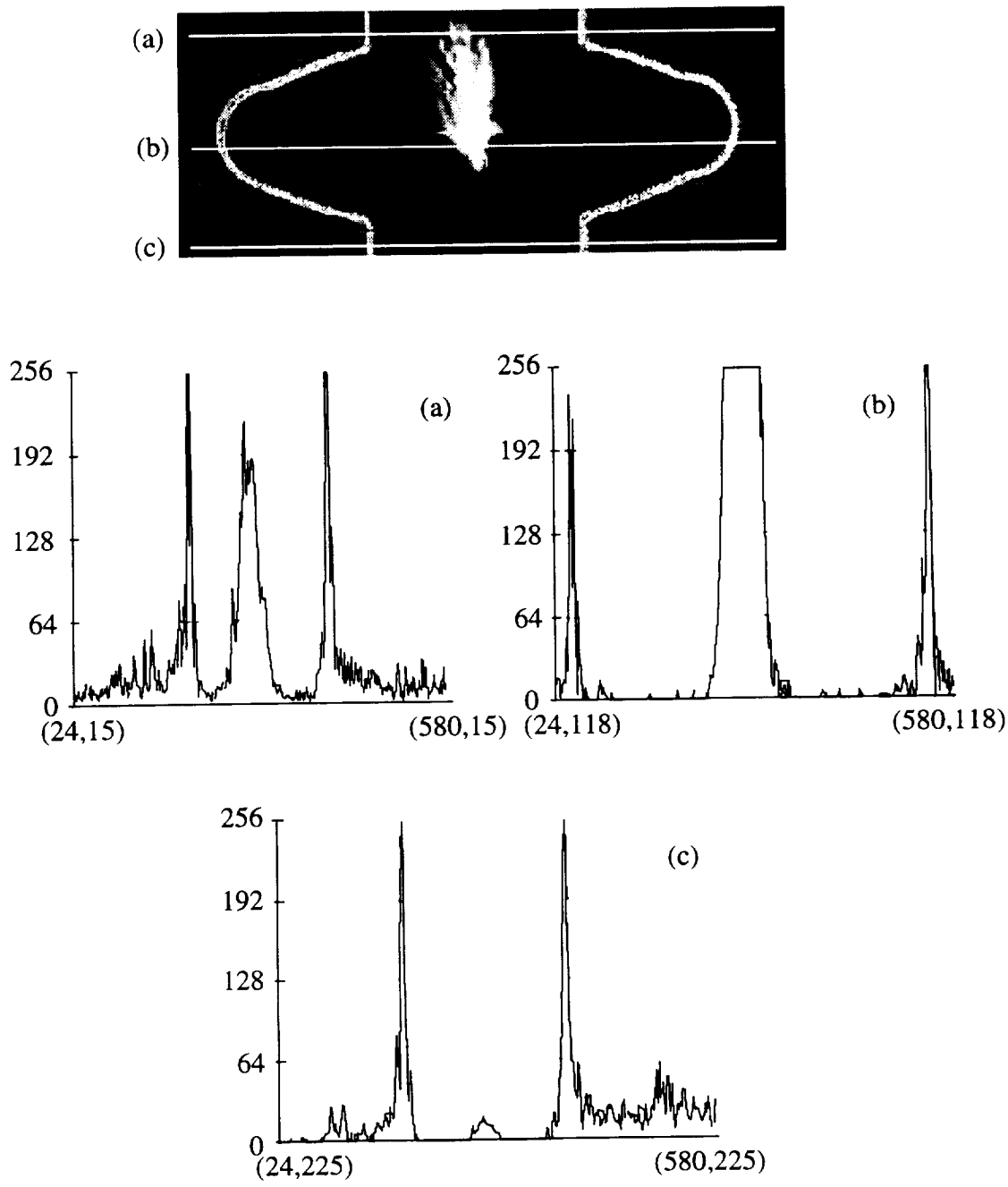

Figure 4.7. Method of centerlines. $\Lambda = 0.225$

4.3. Results

4.3.1 Static stability limits

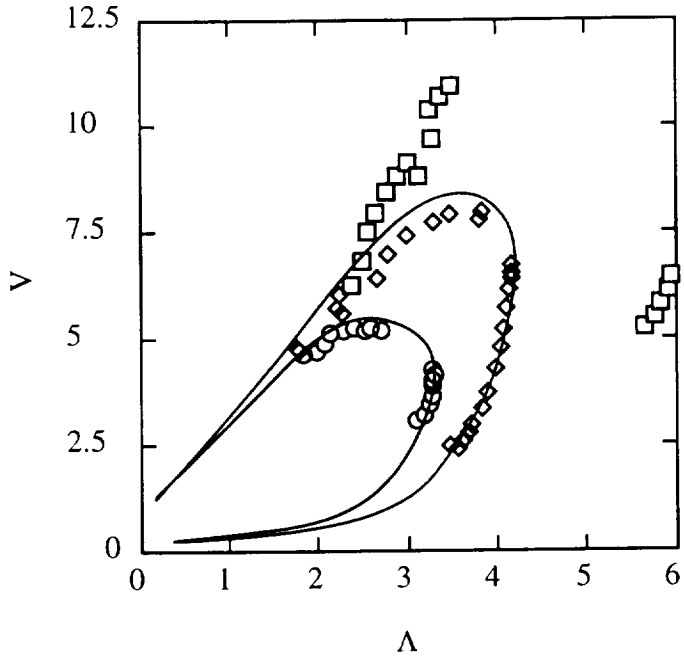

Figure 4.8. Comparison of numerical and experimental results. (□): Bo = 0.002. (◇): Bo = 0.056. (○): Bo = 0.089. (red line): numerical results, Bo = 0.05. (blue line): numerical results, Bo = 0.1.

The results obtained for various Bond numbers are presented above, in Figure 4.8. Each region of stability for a given Bo is enclosed by a region with a smaller Bo. There is no maximum Bo such that there exists stable axisymmetric bridges. Each region is closed, except for the case Bo = 0. Along segment OC (see Figure 4.1), the bridge will lose axisymmetric stability and attain a stable nonaxisymmetric shape. This configuration will be stable for volumes well in excess of the axisymmetric limit (see Figure 4.9) As point C is approached, the bridge will lose stability to a nonaxisymmetric mode while also necking down axisymmetrically (see Figure 4.10). Along the segment CD, the bridge loses stability through axisymmetric modes. It will form a neck, and upon losing stability, will break into two distinct pieces plus a satellite drop (see Figure 4.11). In general, the halves

will not have equal volume, as the dangerous perturbation is a sine function (the neck will occur approximately 1/3 the distance from a support). The segment DO was not investigated here.

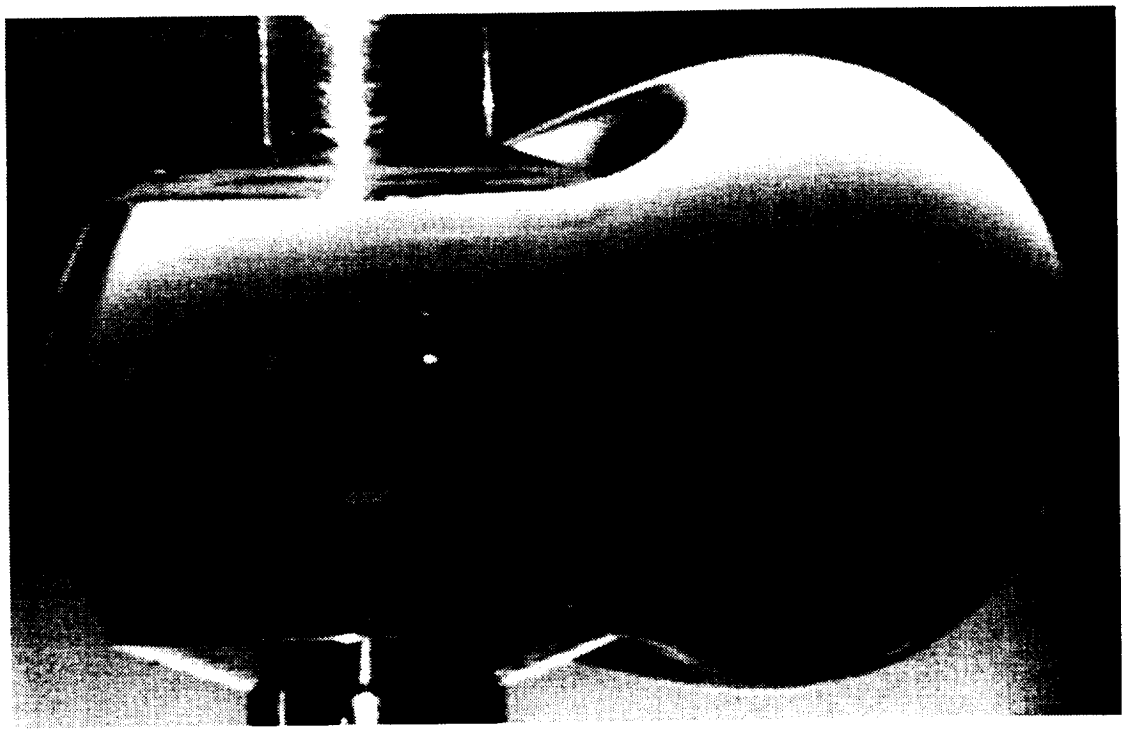

Figure 4.9. A stable nonaxisymmetric bridge. $\Lambda = 0.87$

4.3.2 Bifurcation of a neutrally stable weightless bridge at the maximum volume limit

Figure 4.12, below, summarizes the bifurcation data for liquid bridges of various slenderness using the method of shape deformation (the deformation has been made dimensionless by normalizing to the radius of the disk support). The sudden large deformation observed for bridges with $\Lambda < 0.4$ as they bifurcate from the critical axisymmetric state, combined with the theoretical prediction that these bridges should undergo a subcritical bifurcation, suggests that the expected jump-like transition for $\Lambda \leq 0.4$ is physically manifested in a rapid evolution toward the stable nonaxisymmetric state through a continuous sequence of unstable shapes. Work should be done to

unambiguously determine the presence or absence of hysteresis across the maximum volume limit.

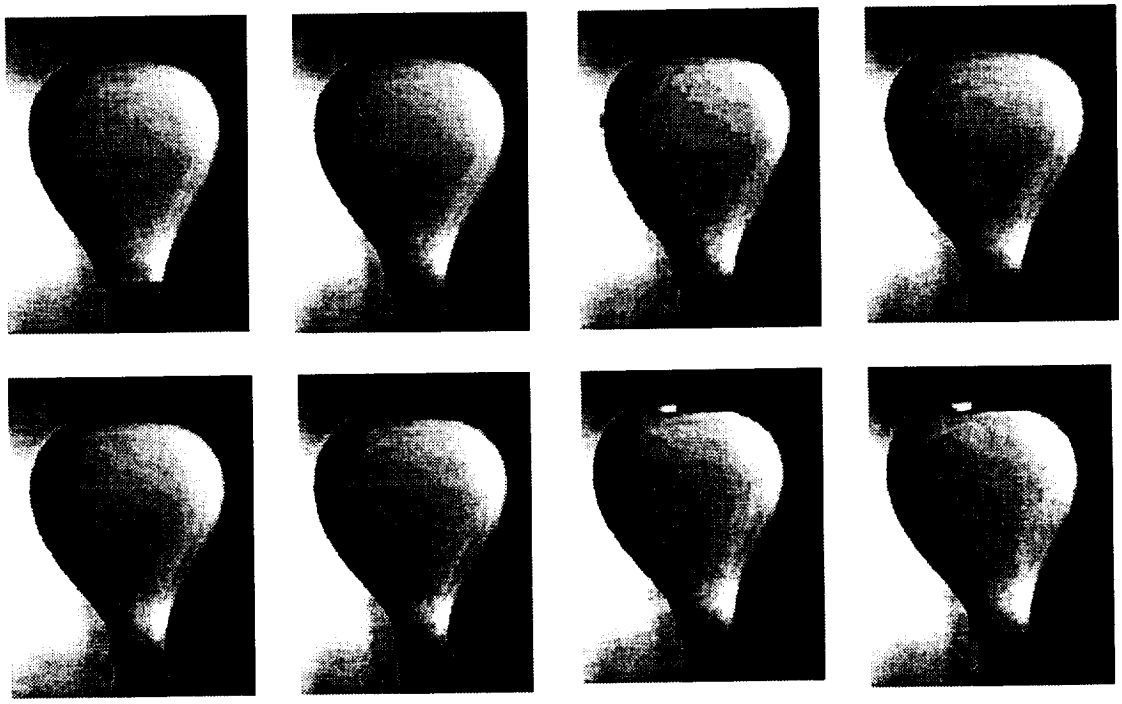

Figure 4.10. Loss of stability near the transition point C. $\Lambda = 3.530$. Bo = 0.089

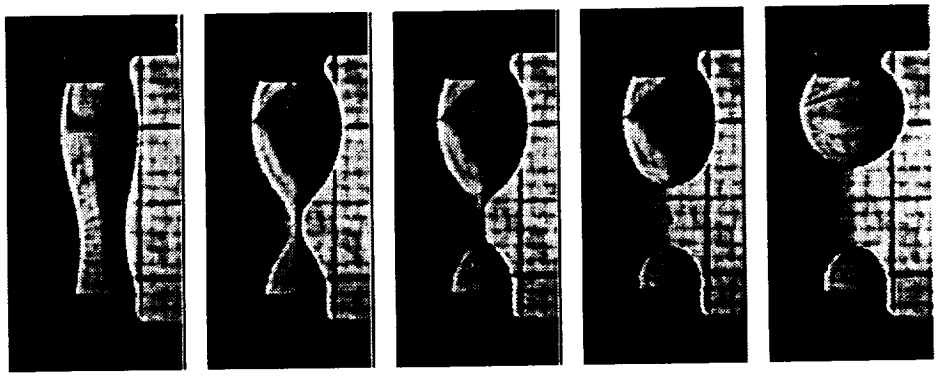

Figure 4.11. Loss of stability to axisymmetric perturbations. $\Lambda = 3.412$.

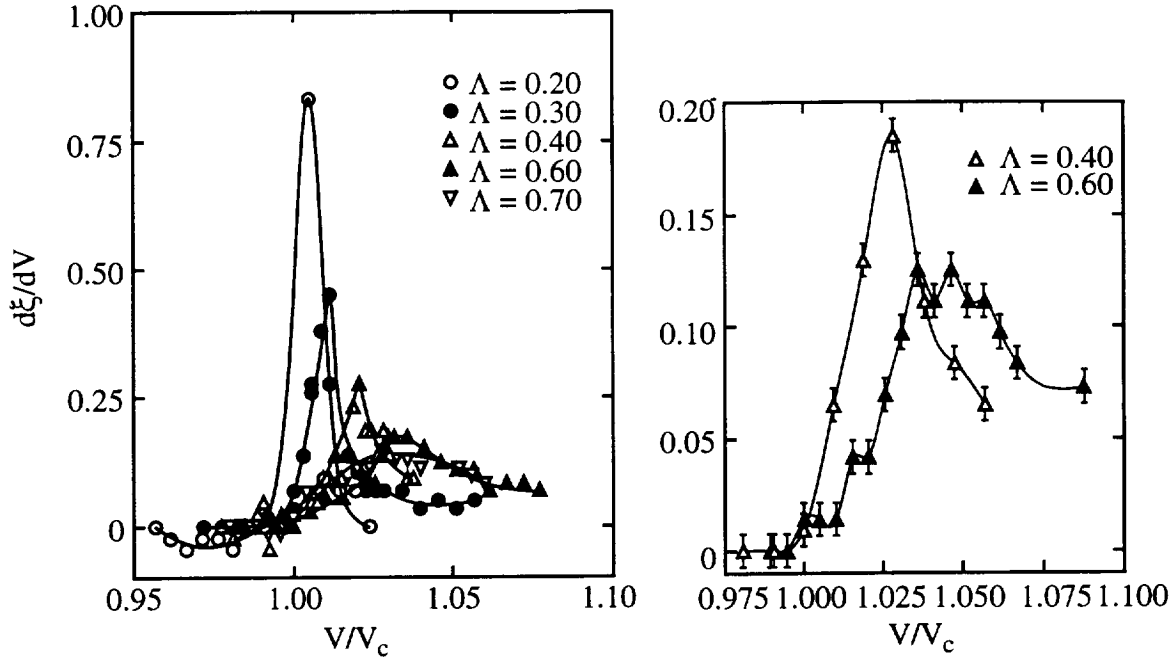

Figure 4.12. Data for bifurcation experiment. Shown here is the rate of change of dimensionless deformation ξ versus V against V/V_c.

4.4. Conclusions

The static stability limits for axisymmetric liquid bridges held between coaxial disks of equal radii were investigated. The experimental data agrees with previous results, except for the maximum volume, large Λ regions of stability. This is due to imperfect wetting at the disk edge, which causes the bridge to lose stability prematurely. The detailed behavior of a bridge as it undergoes a bifurcation to a nonaxisymmetric configurations was studied. It has been shown that there exists a critical slenderness Λ_c, below which the bridge undergoes a rapid transition to a stable nonaxisymmetric shape, and above which the bridge undergoes a continuous transition to a stable nonaxisymmetric configuration. Future work could study the stability limits of nonaxisymmetric bridges, either large bridges held between coaxial disks or bridges held between noncoaxial disks. The loss of stability due to contact line depinning could be studied as well (segment OD in Figure 4.1).

Chapter 5

DETERMINATION OF THE STABILITY LIMITS OF LIQUID BRIDGES HELD BETWEEN UNEQUAL COAXIAL SUPPORT DISKS

1. Introduction

The static stability limits for axisymmetric liquid bridges held between unequal coaxial circular disks were measured as part of a process to analyze the effect of support geometry on liquid bridge stability. Although much work has focused on stable bridge configurations held between supports of equal size, much less work has been performed when the supports, either spheres [31] or disks [73, 115], are of unequal size, and focused on the minimum volume limit. Here, both maximum and minimum volume limits were measured for K = 0.2, 0.4, 0.6, and 0.8, where K is the ratio of the disk diameters. These limits were each measured at Bo = $\pm$0.100. In addition, the effect on bridge stability as $K \rightarrow 0$ was investigated for K = 0.09. It should be emphasized that this is the first experimental comprehensive examination of the problem, and the first examination of the maximum volume limit. With the exception of [165, 265], the numerical solution to this problem has not been worked.

2. Method

The experimental method used is identical to the method described in Chapter 4. A bridge would be created at a starting configuration (Λ_i, V_i) and the disk separation and volume slowly changed to bring the bridge to the stability limit.

3. Results

The character of the stability limits is fundamentally altered for the case of unequal disks (Figure 5.1). These numerical solutions for this problem was presented in [169]. Now there is a difference if gravity is pointing "up", towards the larger disk (Bo < 0), or "down" towards the smaller disk (Bo > 0). The regions of stability are no longer nested as they were for the case of equal disks. There exists a maximum positive Bond number for each value of K < 1 such that there are no stable bridges for Bo > $Bo_{max}(K)$. There exists several cusp points on the boundary. For Bo > 0, the cusp point on the lower boundary is an absolute minimum volume for a particular aspect ratio, for all values of K. The effect of axisymmetric loss modes at the lower cusp point can be used as part of a very sensitive method to measure Bo (see Chapter 3, [116]). For Bo < 0, K < 0.3, there exists a cusp point on the maximum volume limit marking a transition from nonaxisymmetric breaking modes ($\Lambda > \Lambda_c$) to axisymmetric breaking modes ($\Lambda < \Lambda_c$). For Bo > 0, K < 0.3, there is also a transition to axisymmetric breaking modes on the maximum volume limit, but there is no corresponding cusp point.

The experimentally measured stability limits are shown below (Figure 5.2). The location of the cusp point on the minimum volume limit was found for Bo = 0.1 and all values of K. It as found that for Bo = +0.1, K < 1, stability may be enhanced in the sense that a bridge of a given aspect ratio will be stable at a smaller volume than is possible for K = 1. When gravity points toward the smaller disk (Bo > 0), the bridge assumes a pendant drop shape and this helps the bridge remain anchored to the smaller disk (see Figure 5.3a). The transition from nonaxisymmetric critical perturbations to axisymmetric critical

perturbations on the upper stability limit was found for K = 0.2. Figure 5.4 shows a bridge near the maximum volume limit when critical perturbations are axisymmetric.

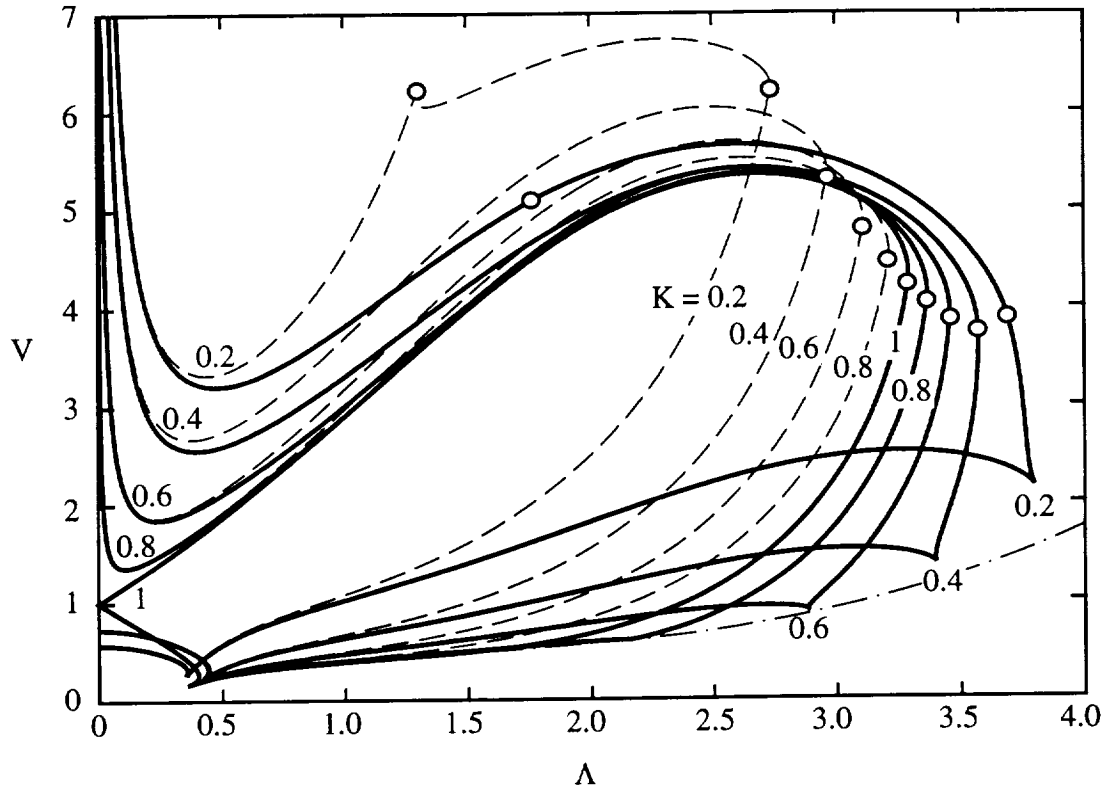

Figure 5.1. Numerical stability limits for K < 1. (solid): Bo = 0.1. (dashed): Bo = -0.1. (dot-dashed): K = 1, Bo = 0 minimum volume limit, for comparison (from [165]).

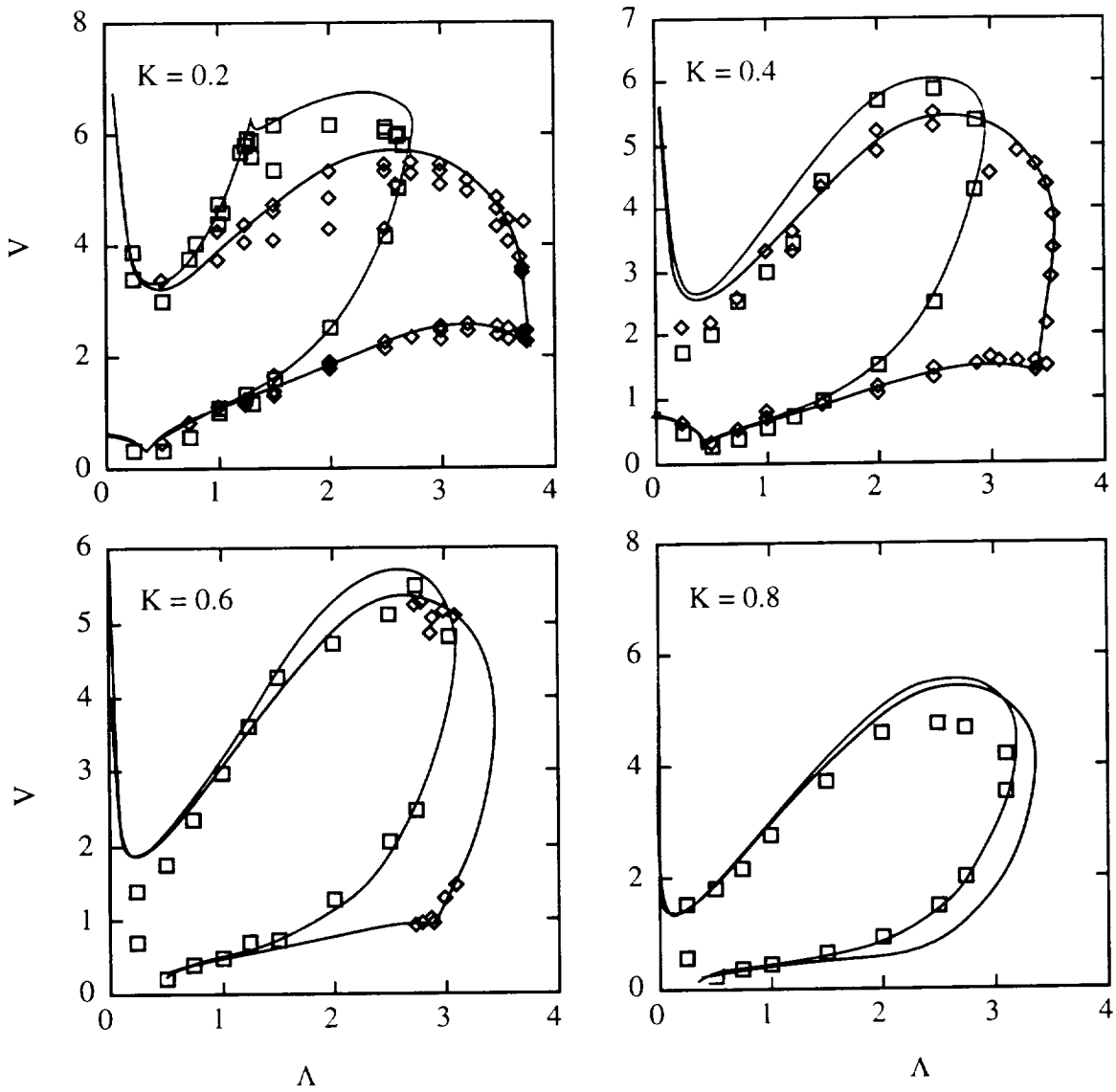

Figure 5.2. Experimentally measured axisymmetric static stability limits ($K \neq 1$) for Bo = 0.1 (blue line, ◇) and Bo = -0.1 (red line, □) under different values of the disk diameter ratio K.

The effect on bridge configuration as $K \rightarrow 0$ was investigated. Figure 5.5 a,b are bridges near the minimum volume limit for K = 0.8 and Bo = -0.1. Although the neck is slightly more pronounced than for K = 1, the overall effect is slight. In the limit of $K \rightarrow 0$, the bridge behavior should approach that of a hanging drop or sessile drop, with the additional constraint on Λ. It is important to note that while in the limit of a vanishing disk

radius the minimum volume limit for a liquid bridge has a physical meaning, while for a hanging drop it does not. This can be seen in Figures 5.6 and 5.7, where K = 0.2 (Figure 5.6) and K = 0.09 (Figure 5.7). Here, a squared-off hypodermic needle was used as the lower disk for K = 0.09 (the dropping tip of chapter 3). However, because the needle did not have sharp edges, the maximum volume stability limit could not be studied as the contact line would slip over the edge.

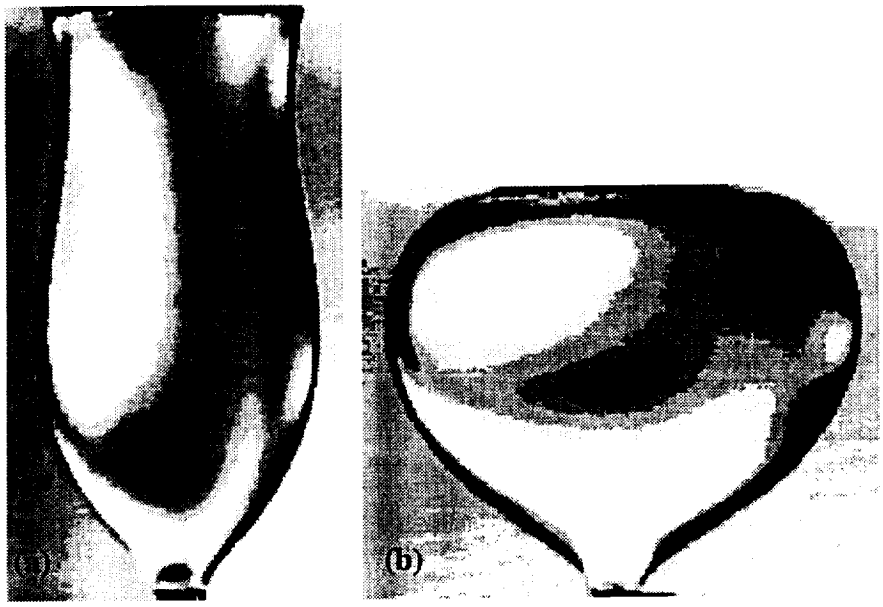

Figure 5.3. Examples of bridges near lower stability limit (K = 0.2). (a) $\Lambda = 3.744$, V = 2.29, Bo = 0.1 (b) $\Lambda = 2.606$, V = 5.04, Bo = –0.1

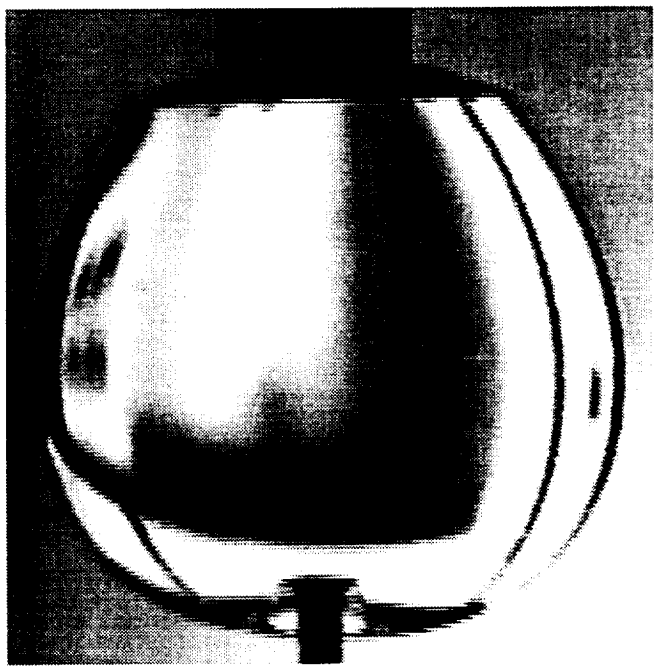

Figure 5.4. Example of symmetric loss of stability along upper stability margin, (K = 0.2, Λ = 1.03, V = 4.59, Bo = 0.1). Note that the disks are slightly misaligned.

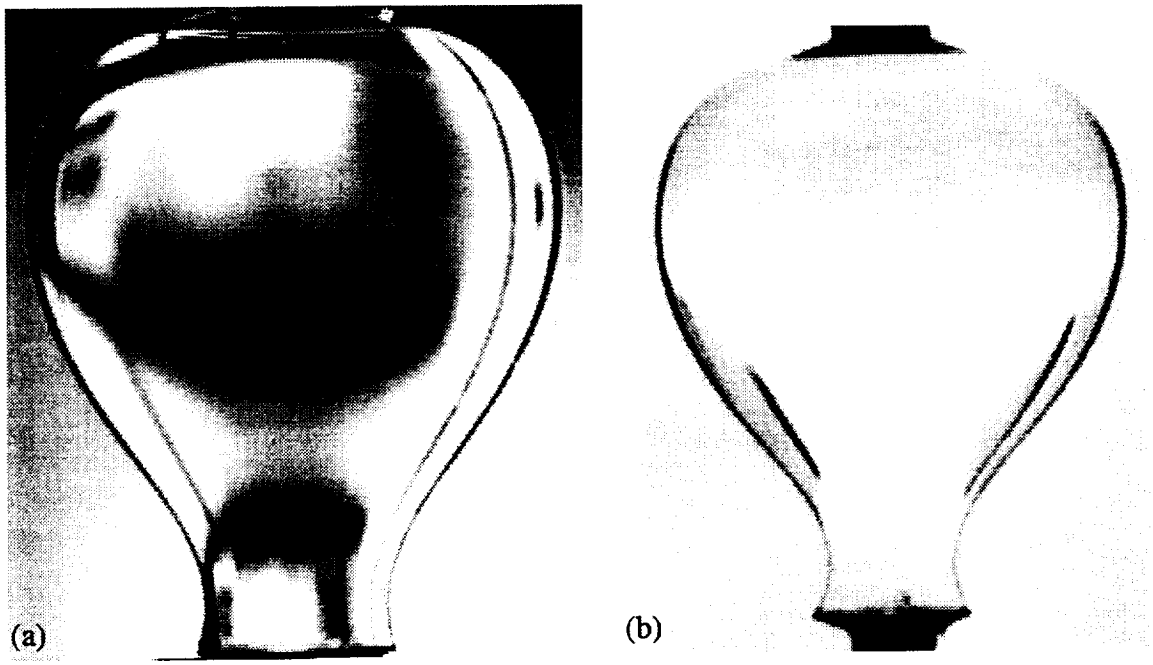

Figure 5.5. Axisymmetric liquid bridges near the minimum volume limit (K = 0.8, Bo = –0.1). (a) Λ = 2.778, V = 5.00. (b) Λ = 3.28, V = 4.82.

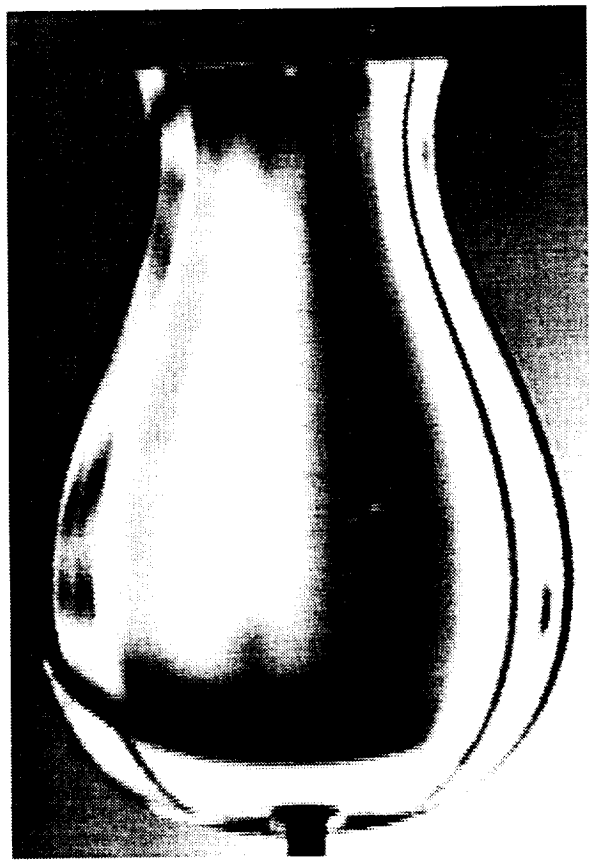

Figure 5.6. Effect on bridge configuration as $K \rightarrow 0$ ($K = 0.2$, $Bo = 0.1$). $\Lambda = 3.73$, $V = 3.47$

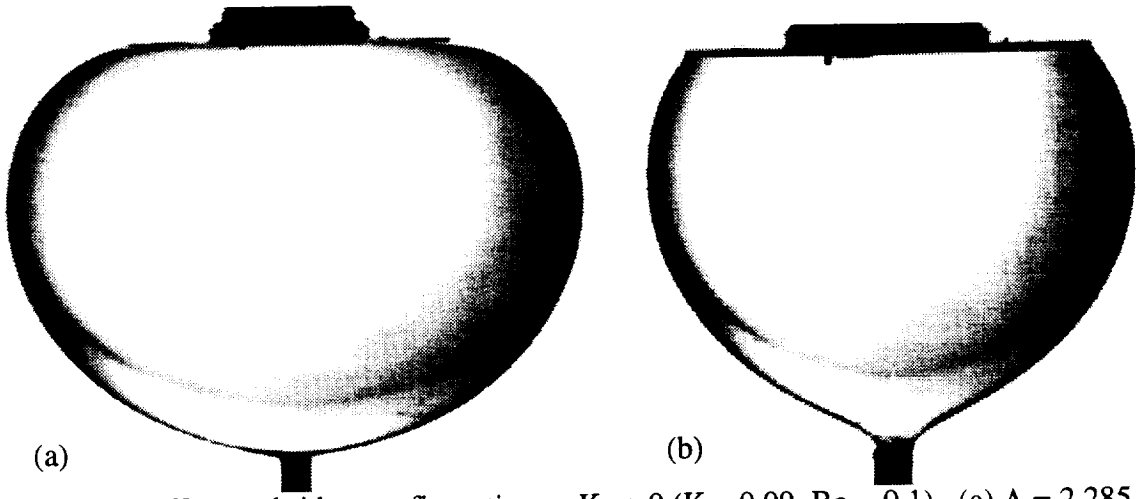

(a) (b)

Figure 5.7. Effect on bridge configuration as $K \rightarrow 0$ ($K = 0.09$, $Bo = 0.1$). (a) $\Lambda = 2.285$, $V \sim 6$. (b) $\Lambda = 1.73$, $V \sim 3$.

4. Conclusions

The effect of support geometry on bridge stability was investigated through use of coaxial unequal disk supports. Several qualitative differences occur between this case and the case K = 1. The minimum volume cusp point provides a useful method for determining Bo. In [116] a similar method to the one outlined here was used, the difference being in that case, the ratio of drop volumes after breaking was used to determine the location of the cusp point. The existence of a second transition point on the maximum volume limit to axisymmetric breaking modes is a second difference. Comparison of experimental values with numerical calculations is good, except at the maximum volume limit, large Λ region, the same as K = 1. This is due to imperfect wetting conditions at the disk edge. The limiting effect as $K \rightarrow 0$ was investigated for K = 0.09. Bridge stability is enhanced when Bo > 0, K < 1, even approaching the Bo = 0, K = 1 case. Future work could investigate the stability of nonaxisymmetric bridges that result following the loss of axisymmetric stability, as outlined at the end of chapter 4. The limiting case for $K \rightarrow 0$ could also be investigated further. The most practical way would be to increase the larger disk radius.

Chapter 6

DYNAMICS OF VIBRATING LIQUID BRIDGES

1. Introduction

A series of experiments has been undertaken to determine the spatial mode structure of neutrally buoyant right circular cylindrical liquid bridges held between coaxial sharp-edged disks subject to lateral sinusoidal oscillation at various amplitudes in the neighborhood of the fundamental resonance (see Figure 6.1). This began as a verification of a g-jitter numerical study performed earlier [106]. Experimental and theoretical studies of non-axisymmetric oscillations are limited. Small amplitude inviscid non-axisymmetric oscillations have been examined theoretically by Gañán and Barrero [97]. Experimental work with lateral oscillation of the lower disk was also carried out by Sanz and Lopez-Diez [62] and Tsamopolous *et al.* [15]. Experiments were performed with both the disk supports vibrating laterally in phase. In all frequency sweeps, the acceleration was held constant, thus requiring the displacement amplitude to change with frequency. This is different from previous experiments [62] where the displacement amplitude was held constant during a sweep of frequency. This way we could measure the bridge sensitivity to acceleration in a more straightforward manner. We attempted to measure the resonant frequency by visually observing an oscillating bridge, by measuring the mechanical gain of the system (maximum bridge deformation divided by maximum disk amplitude), and by measuring the contact angle during oscillation. We are interested in nonlinear shape

behavior and nonlinear frequency response of vibrating liquid bridges, which act as weak springs [15]. In an effort to explain the resonant behavior in detail, three methods were used to analyze the dynamic bridge shape. The refraction of a laser beam passing through the bridge in the plane of vibration was observed. The spatial mode structure of the bridge was imaged via the Fourier plane. Finally, an FFT was performed on the filtered image of the bridge.

Here the first experimental observation of the nonlinear third harmonic present in a liquid bridge undergoing lateral vibration at the fundamental frequency is reported. Typically, a forced nonlinear oscillator will display a nonlinear third harmonic contribution to the response [269]. Images of a V = 1, Λ = 2.6 bridge oscillating near N = 1, 2, and 3, m = 1 resonances are shown below (Figure 6.2).

2. Gain experiments

This method was originally chosen because previous experiments used the same method [62]. However, at small excitation amplitudes, bridges made from 100 cs oil would not deform enough to provide an accurate measurement. Thus, 5 cs oil was used. The gain was measured by measuring the maximum amount of bridge deformation and comparing it to the amount of distance the support disks moved. The maximum deformation of the bridge was measured by placing a Ronchi ruling between the collimating lens and the liquid bridge. The magnification of the ruling was measured by moving a disk a known distance until one period of the ruling had been traversed. Each Ronchi ruling period corresponded to 0.5 mm in the object plane. Thus, the deformation could be measured by counting the line pairs of the ruling. This method provided a simple and reasonably accurate means to measure a deformation of a fluid body when the center of mass does not remain in a set position. A sample raw image is shown below [Figure 6.3]

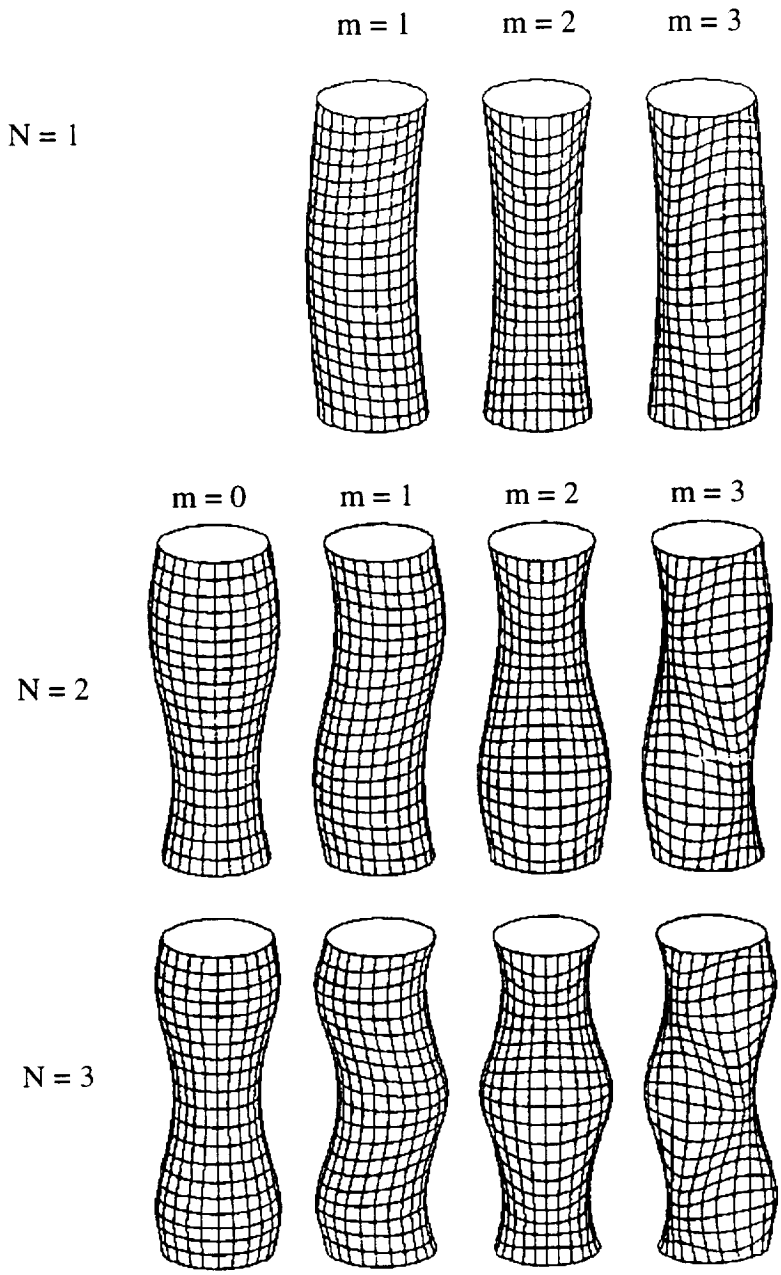

Figure 6.1. Computed resonant shapes of laterally oscillated bridges (from [62]).

(a) (b) (c)

Figure 6.2. Images of laterally oscillated $\Lambda = 2.6$ liquid bridges. (a): N = 1, m = 1. (b): N = 2, m = 1. (c) N = 3, m = 1.

The gain curves show clear evidence of saturation (Figure 6.4). That is, increasing excitation amplitudes do not produce a proportionately increasing deformation. It should be pointed out that large amplitude oscillations produce bridge motion not limited to m = 1. In addition, evidence of complicated bridge behavior in the neighborhood of the resonant frequency at small amplitude oscillations is seen. In particular, the presence of the local minimum on what is otherwise an ordinary resonant peak prompted the construction of a method to even more precisely and accurately characterize the bridge shape during oscillation. Measuring the contact angle the bridge makes with a disk support provides more sensitive measurements. The reason for this is explained below.

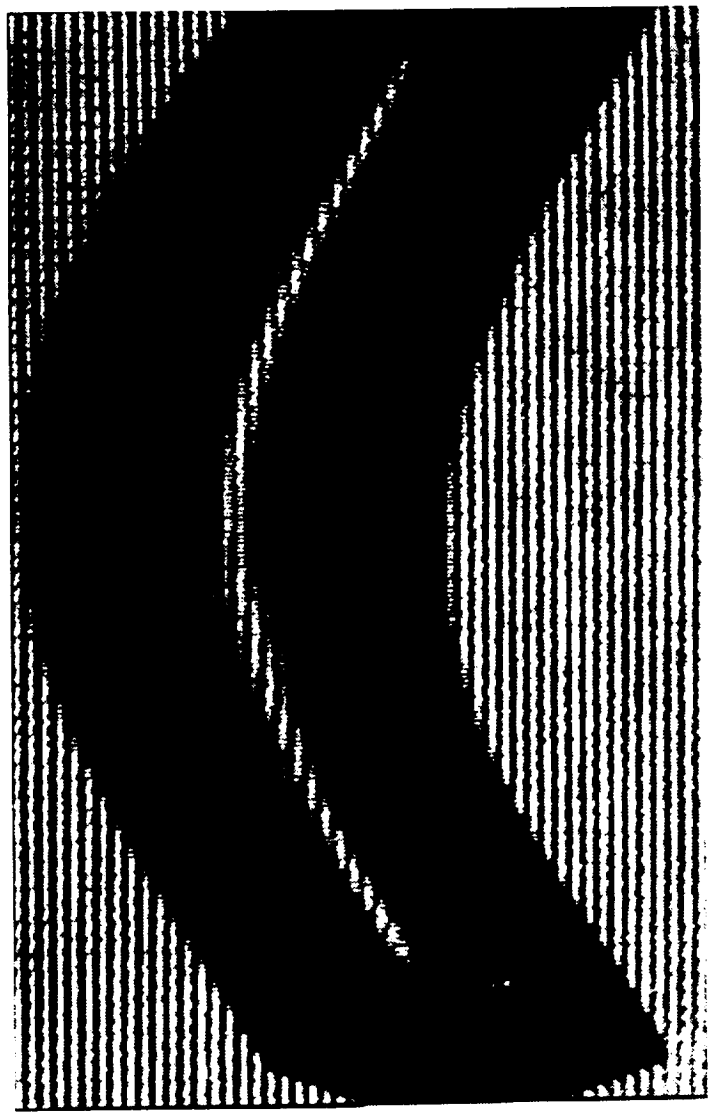

Figure 6.3. Experimental image of a laterally oscillating liquid bridge, $\Lambda = 2.826$

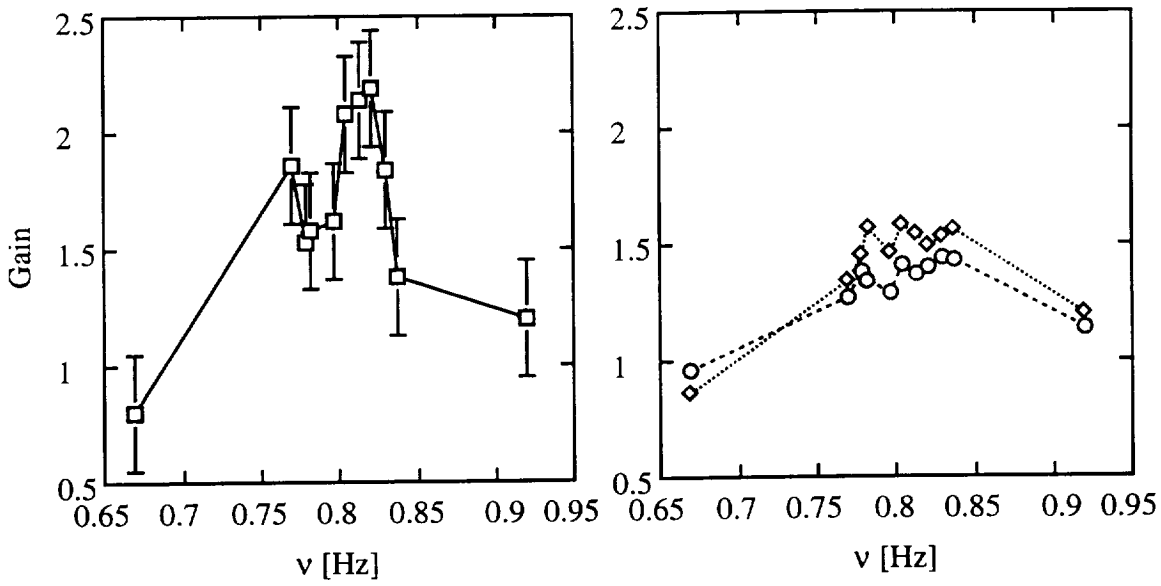

Figure 6.4. Experimentally obtained gain curves, $\Lambda = 2.826$. (□): A = 0.1 cm/s^2. (◇): A = 0.5 cm/s^2. (○): A = 1.0 cm/s^2. Note the saturation and the complex behavior of the gain curves in the vicinity of the resonant frequency.

A V = 1 weightless liquid bridge undergoing a small lateral sinusoidal oscillation has a deformation f_p [15,62]:

$$f_p \sim A_{Nm} Z_{Nm}(z) \cos m\theta \cos(\omega_{Nm} t + \phi_{Nm}), \tag{6.1}$$

where N, m are the axial and azimuthal wave numbers, respectively. The axial term, Z_{Nm}, closely matches $\cos(\pi z/2\Lambda)$ for N = 1 and $\sin(\pi z/\Lambda)$ for N = 2 [15]. The axial function is normalized to the height of the bridge $z = -\Lambda$ to $z = \Lambda$. In the case N, m = 1, and ignoring the time-dependence term, the contact angle ϕ at the disk supports is given by:

$$\tan\phi = \left.\frac{df}{dz}\right|_{z=\pm\Lambda} = A_{11} \sin\left(\frac{\pi z}{2\Lambda}\right)\left.\frac{\pi}{\Lambda}\right|_{z=\pm\Lambda} \tag{6.2}$$

which reduces to:

$$\phi = \tan^{-1}\left(A_{11}\frac{\pi}{\Lambda}\right) \tag{6.3}$$

Therefore, if $A_{11} << 1$ (small amplitude excitations), small changes in the excitation δA_{11} will produce small changes in deformation δf_p but large changes in contact angle $\delta\phi$. In addition, the contact angle can be measured more accurately than the shape deformation amplitude. In addition, we felt that we could reduce some of the measurement error by using contact angle measurements.

3. Contact angle experiments

Experimental data of the range of contact angle motion during lateral oscillation is shown below **[Figure 6.5]**. Each point represents 6 measurements of the contact angle taken at 100x magnification (3 at maximum and 3 at minimum). The time of maximum and minimum contact angle was fixed by measuring the contact angle 20 times during one oscillation period. The image was frame grabbed and each captured digital image was analyzed manually by an image processing program (Matrox Inspector®).

$\Lambda = 3.0$ shows behavior consistent with the gain data and [15]. The resonant frequency is lower than the linear theory predicts, consistent with a liquid bridge representing a soft spring. Now a local minimum can be clearly seen in the neighborhood of the resonant frequency. Based upon eigenmode analysis (see below), the local minimum is at the resonant frequency, and that the inhibition of contact angle motion is caused by nonlinear shape deformations of the bridge.

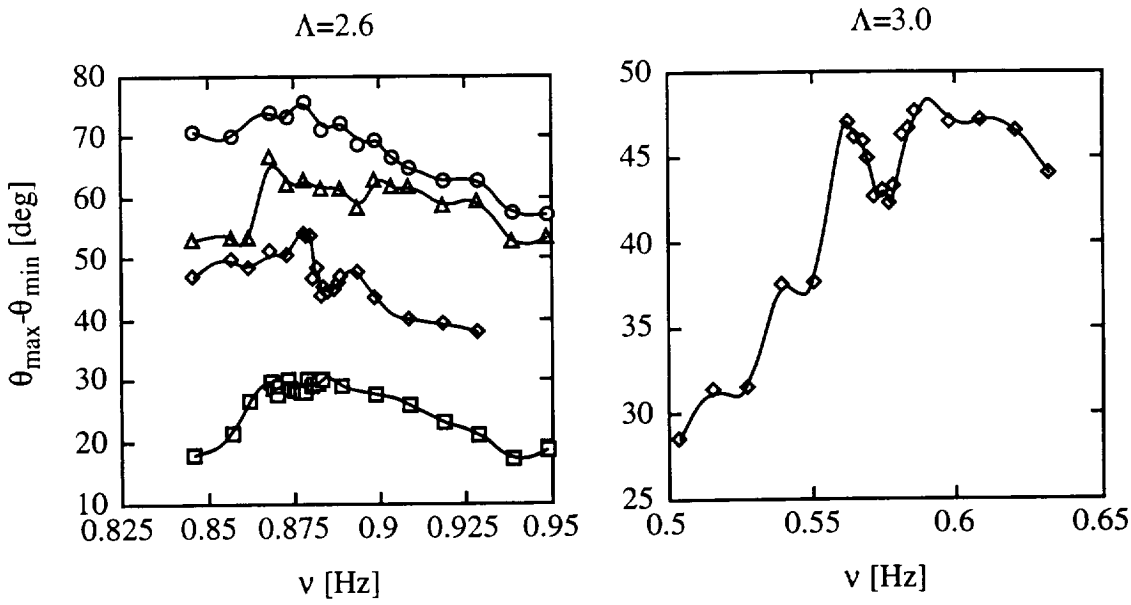

Figure 6.5. Measured range of contact angles assumed during lateral oscillation of a liquid bridge. (□): A = 0.1 cm/s^2. (◇): A = 0.2 cm/s^2. (△): A = 0.3 cm/s^2. (○): A = 0.4 cm/s^2.

There is similar behavior when laterally vibrating a bridge of Λ = 2.6. There is a local minimum of contact angle motion immediately surrounding the resonant frequency. Note that at high vibration amplitudes, the liquid bridge is not in a pure m = 1 state. This explains the broadening of the resonant peak, and the loss of a well-defined local minimum.

4. Mode analysis

Three different methods were used in an attempt to quantify the spatial mode structure of the bridge during oscillation. The first involved observing a raw laser beam as it was deflected by the bridge deformation. The second involved observing the behavior of the bridge in the Fourier plane. Lastly, a FFT was performed on the filtered image of the bridge.

4.1 Laser beam deflection

Because the index of refraction of the bridge is different from the index of refraction of the bath, light passing through the bridge is refracted (Figure 6.6). A raw laser beam passed through the bridge near the centerline in the plane of oscillation at various axial heights. A position sensitive photodiode collected the deflected beam (see chapter 7), and the position monitored as the bridge underwent lateral vibration. An advantage of this method is that effects from $m \neq 1$ modes can be partially filtered out by only observing the deflection in the axial direction. The shape of the beam that impinges on the photodiode is a horizontal line due to refraction of the light through the bridge. The bridge has approximate optical powers of 0.12 perpendicular to the plane of oscillation and 0.02 in the plane of oscillation. Both of these depend on the specific composition of the bath and the shape of the bridge. A cylindrical lens, placed appropriately, would cancel out much of the refraction perpendicular to the plane of oscillation. Data is shown below [Figures 6.7-6.9]. Some striking features especially stand out.

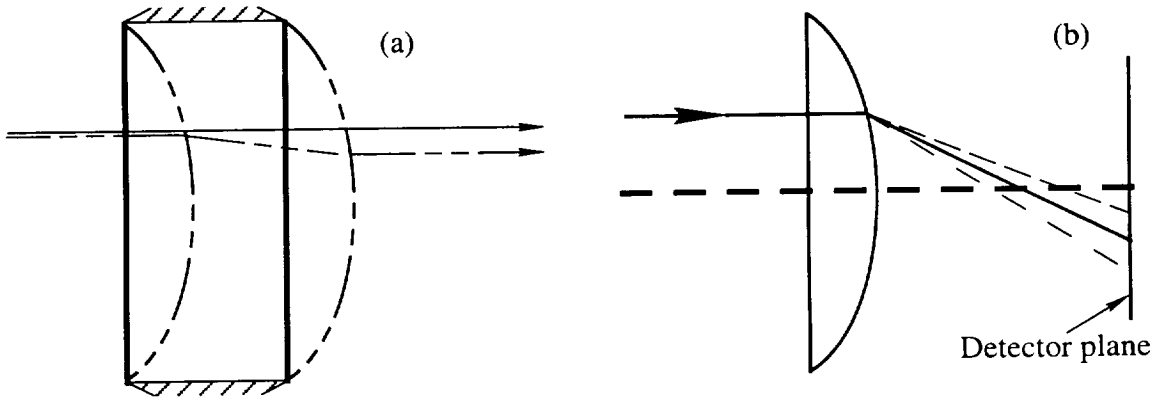

Figure 6.6. The refraction of a light ray through an oscillating liquid bridge. (a): the deflection of a beam during oscillation. (b): the effect of aberrations on a refracted beam

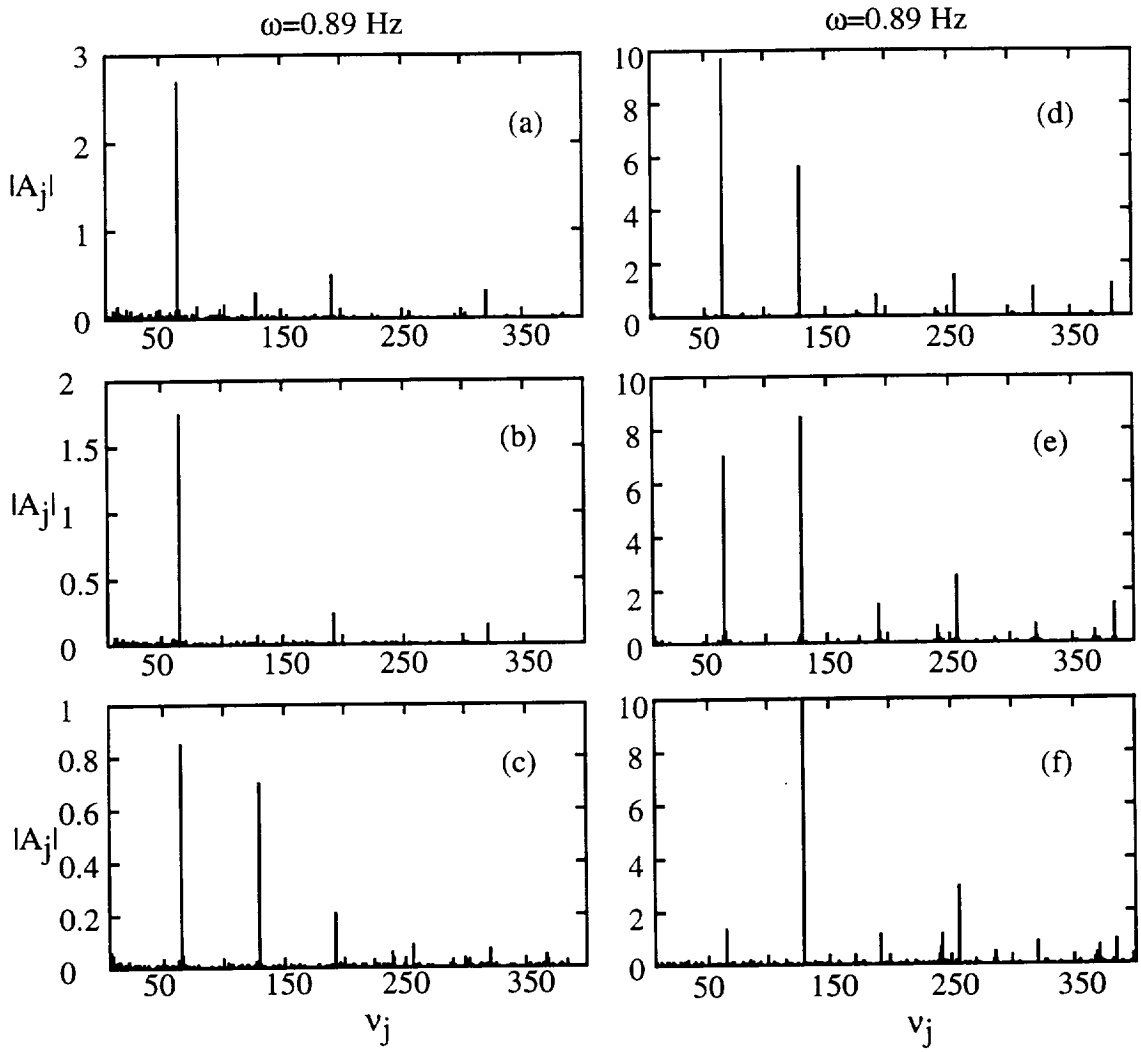

Figure 6.7. FFT of a raw laser beam passing through a laterally oscillated bridge in the plane of vibration. See text for a detailed description

Figures 6.7 a-f show the FFT obtained by a beam passing through different portions of the liquid bridge. In all cases, the beam passes through a $\Lambda = 2.6$ bridge in the plane of oscillation, near the centerline. Figure 6.7 a-c is for an oscillation amplitude of 0.1 cm/s^2, and Figure 6.7 d-f if for an amplitude of 0.5 cm/s^2. Note the difference in behavior as the beam passes through the bridge (a,d) near the feed disk ($z = \Lambda$), (b,e) halfway between the feed disk and the midplane of the bridge ($z = \Lambda/2$), and (c,f) the midplane of the bridge ($z = 0$). Figure 6.7 a-c represents the behavior of the bridge in a

small oscillation regime, while Figure 6.7 d-f represents nonlinear behavior of the bridge. Note the presence of the second harmonic which occurs even at very low excitation amplitudes. The second harmonic is most suppressed at $z = \Lambda$ (near the support disks) and least suppressed at $z = 0$ (the midplane). When the beam passes near the midplane, the beam is undeflected for a total of 4 times per oscillation period, when it is undeflected a total of 2 times at other axial positions. The higher order terms are due to aberrations introduced by the dynamic surface of the bridge. This is shown schematically in Figure 6.6 b for the simplified case of spherical aberration. As the bridge deforms, the surface becomes (equivalently) an aberrated lens (broken lines in Figure 6.6 b), and the beam will strike the detector in a different spot than it would for an aberrated lens (solid line in Figure 6.6 b). Thus the higher order modes present in the refraction data provide information about the dynamic shape of the bridge. A careful quantitative analysis of the aberration effects would be very useful and might provide a detailed description of the dynamic bridge shape during oscillation.

Figures 6.8 and 6.9 are spectra of beam deflection for a beam located at $z = \Lambda/2$ for a range of frequencies at acceleration amplitudes 0.1 (Figure 6.8) and 0.5 (Figure 6.9) cm/s^2. Although it is not clear which of the excitation frequencies represent an eigenfrequency, it is clear that higher-order mechanical vibrational terms are present in the response of the bridge. In all cases, the deflection of the beam shows remarkably sharp peaks, and the spectra is relatively free of noise. The presence of higher-order terms occur with great regularity, in some cases, up to the fifth harmonic is visible. There appears to be a suppression of the higher modes at frequency 0.865 Hz and 0.930 Hz in Figure 6.9. In addition, there seems to be a transition from a slightly noisy spectra below a certain frequency to a very clean spectra above a certain frequency, in this case 0.860 Hz for Figure 6.8 and 0.930 Hz for Figure 6.9.

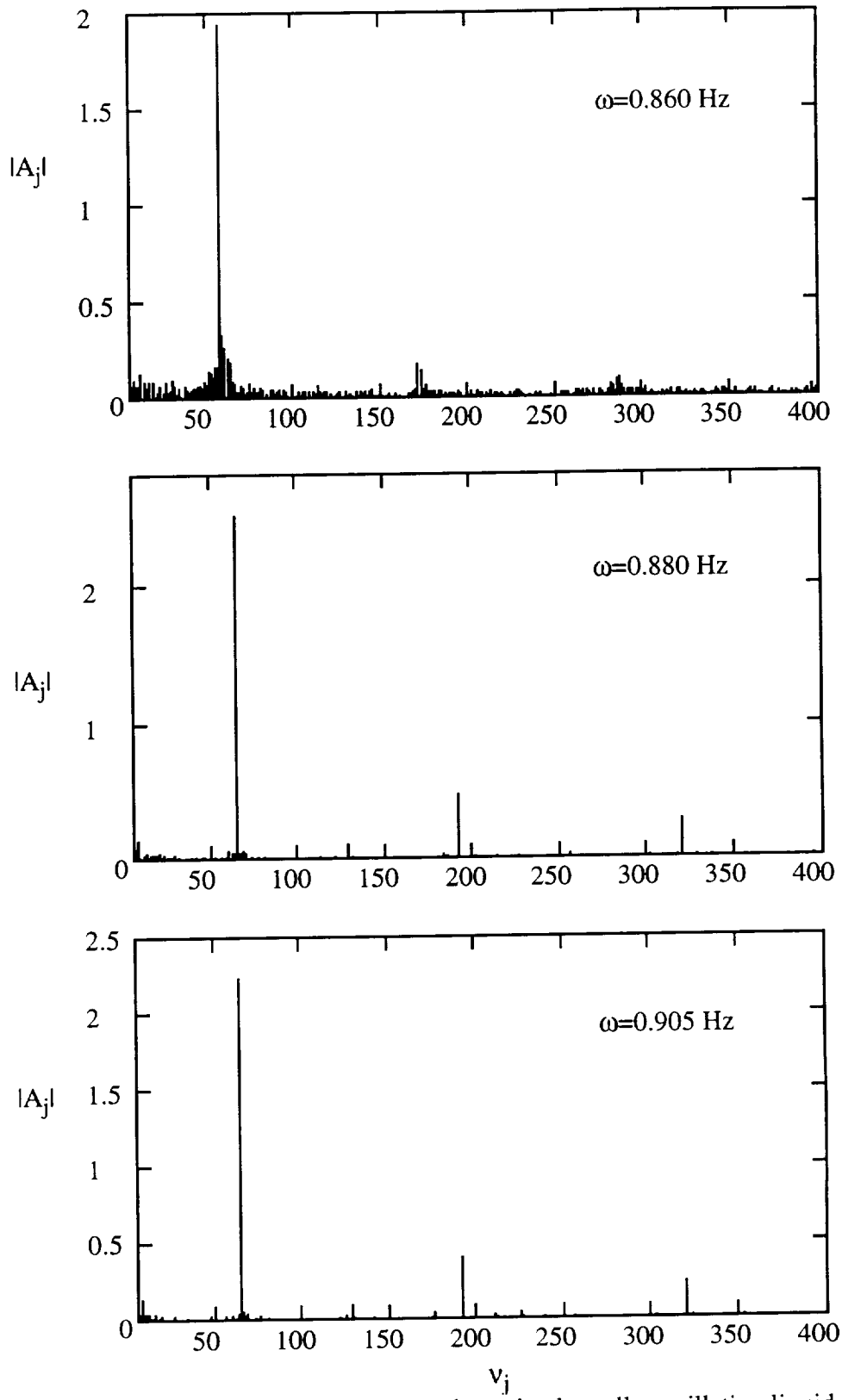

Figure 6.8. FFT of a raw laser beam passing through a laterally oscillating liquid bridge for a range of excitation frequencies at excitation amplitude 0.1 cm/s^2.

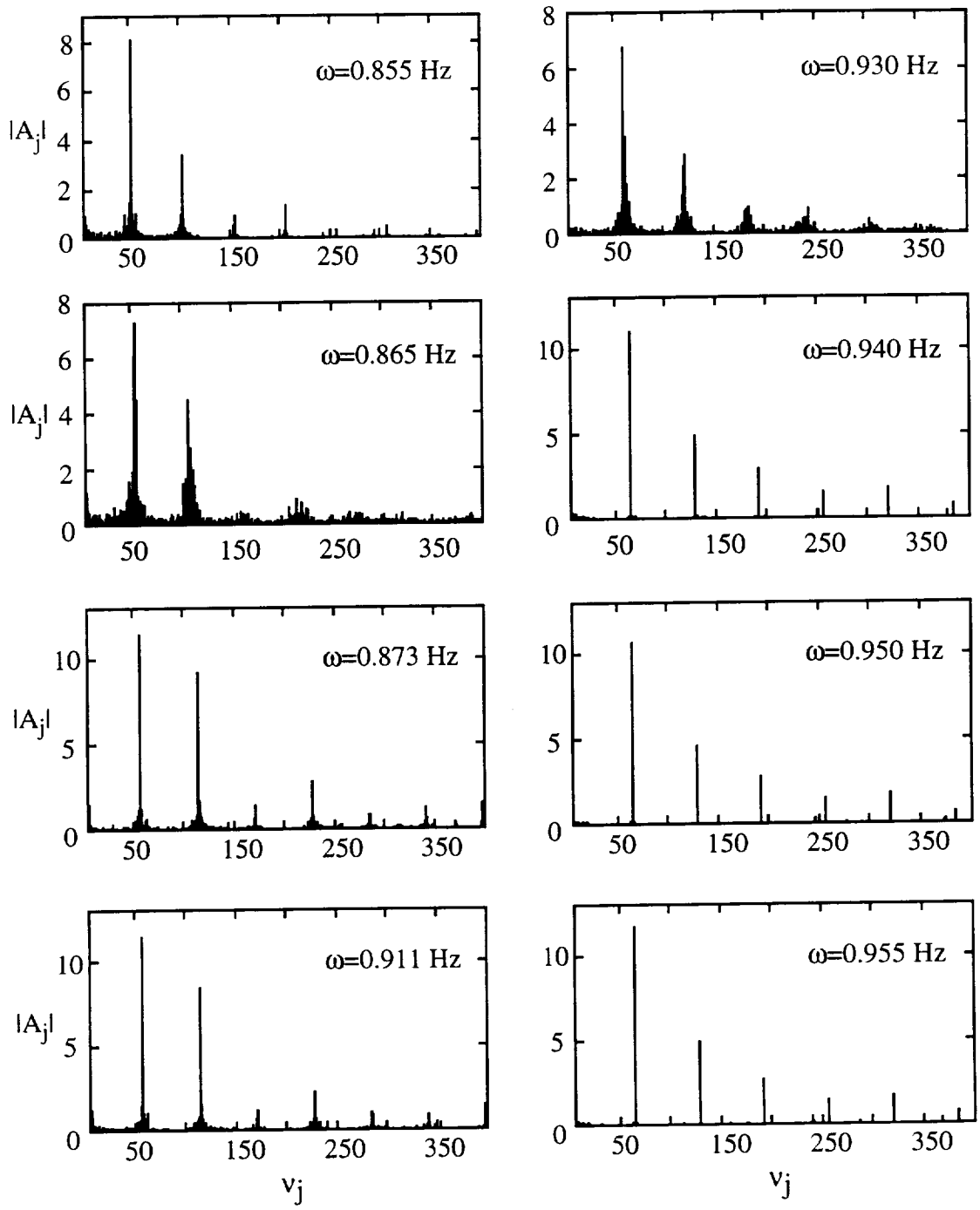

Figure 6.9. FFT of a raw laser beam passing through a laterally oscillating liquid bridge for a range of excitation frequencies at excitation amplitude 0.5 cm/s^2.

4.2. *Direct imaging of the spatial mode structure*

The second experiment directly imaged the spatial Fourier transform of a $\Lambda = 2.6$ liquid bridge. It was hoped that the spatial modes would provide a recognizable signature in the Fourier plane. Fig 6.10 a-d are images of the liquid bridge undergoing spatial oscillations with amplitudes 0, 0.04 , 0.1, and 0.2 cm/s^2 at a frequency of 0.880 Hz. This frequency was chosen because it was near the first resonant frequency for the various amplitudes. The presence of the dc stop is clearly shown.

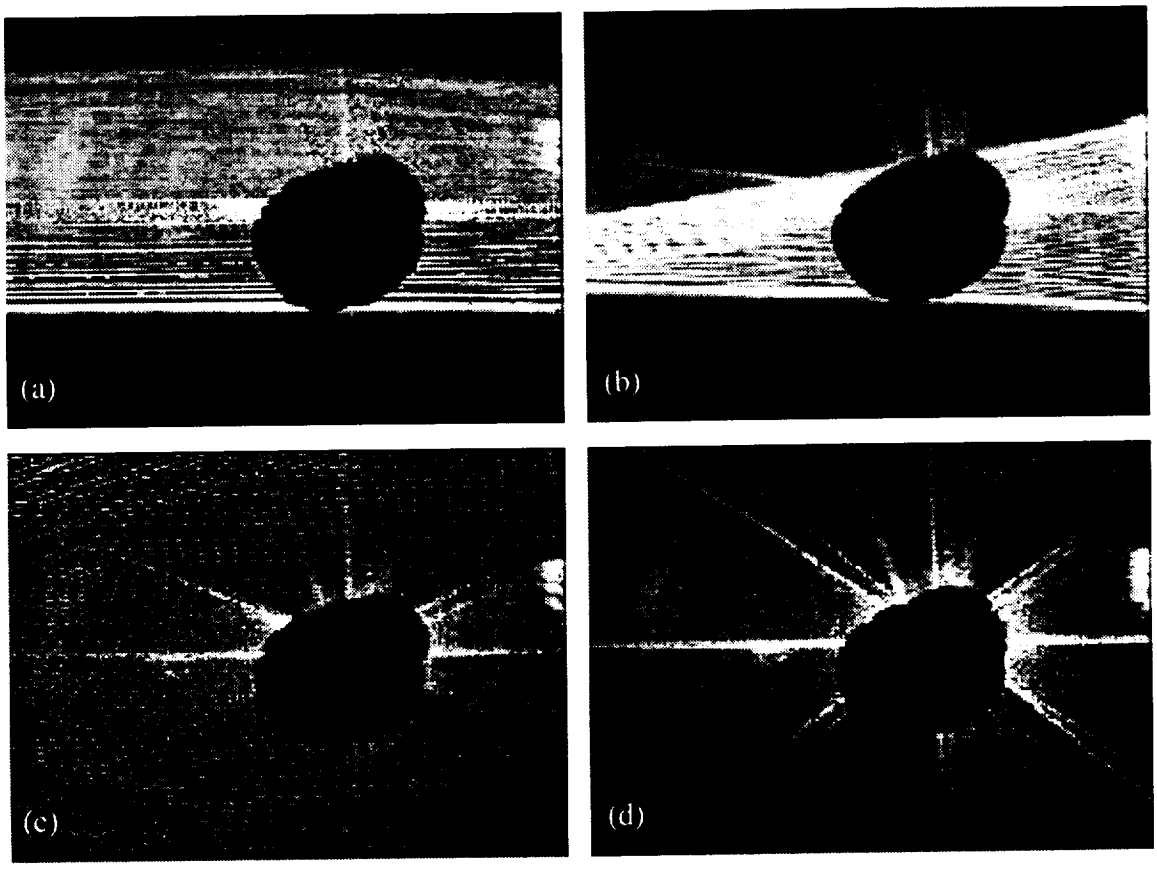

Figure 6.10. Images of the Fourier plane of a laterally oscillated liquid bridge. (a): A = 0 cm/s^2. (b): A = 0.04 cm/s^2. (c): A = 0.1 cm/s^2. (d): A = 0.2 cm/s^2. The dc term has been blocked.

Unfortunately, although some qualitative analysis is possible, the complexity of the Fourier plane precludes quantitative analysis. Among other problems, the light refracted

through the bridge obscures the desired information for much of the oscillation period, and only at some very specific times (maximum, minimum deflections) can the images be compared. An attempt was made to digitally subtract one image from another, but this did not improve the images. The fundamental is shown by the diagonal lines, left-right and up-down symmetric that occur at approximately 45° (this value depends on the amplitude of the deformation). The presence of higher harmonics are revealed by the side-lobes to the fundamental resonance lines. An analytic expression for the Fourier transform of the bridge does not exist, being of the form (using the notation in [263,264]):

$$F(\eta,\xi) = \frac{1}{2\pi}\iint dx\, dy\left[\text{rect}\left(\frac{y}{L}\right)\delta\left(x - \cos(y) \pm \frac{R}{2}\right)\right] e^{2\pi i(\eta x+\xi y)} \qquad (6.4)$$

where the argument is the expression for the (filtered) bridge silhouette. An approximate solution can be obtained by approximating the cosine shape of the bridge as two lines that meet at an angle ζ (see Figure 6.11). The magnitude of the transform of this would also be two lines (really the line response of the system [263]) that intersect through the origin at an angle $\zeta/2$, in qualitative agreement with Figure 6.10 . Recall:

$$g(\eta,\xi) = F(\delta(\theta-\zeta)) = 1/(2\pi^2)(\eta\cos\zeta+\xi\sin\zeta)^{-2}. \qquad (6.5)$$

The lines in the transform plane are at different phases due to the lateral offset of the lines in the object plane from the origin, but intensity-dependent measurements are insensitive to this phase difference. Including lines at different angles to better approximate the true sinusoidal shape would introduce other lines in the transform plane at other angles.

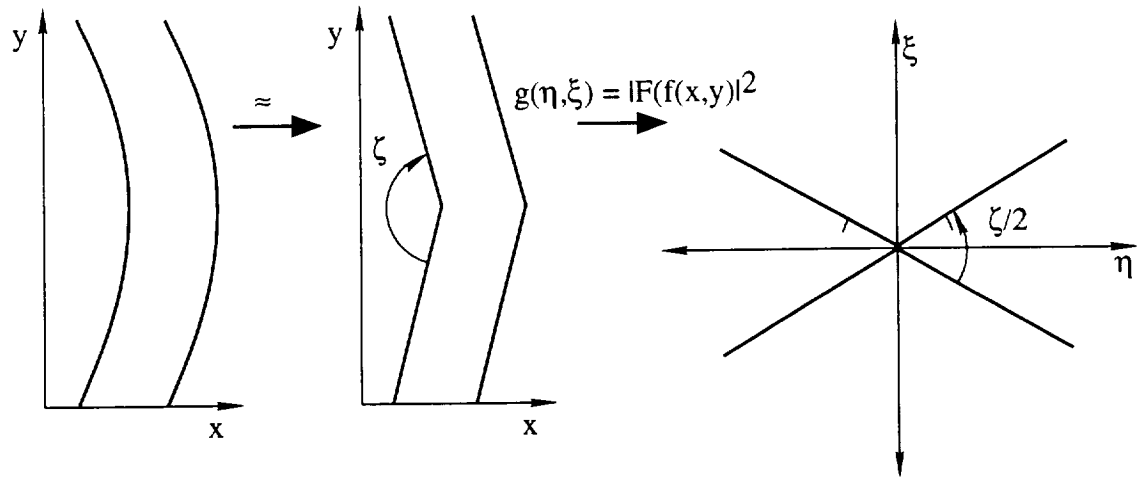

Figure 6.11. Approximation to bridge shape and the corresponding Fourier transform

4.3. Numerical analysis of the bridge shape

Lastly, an FFT of the spatially filtered bridge image was performed (see fig 6.12, 6.13) to analyze the bridge shape. Images taken while the bridge was oscillating were digitized. Scan lines across the image were used in a method similar to the method of centerlines in chapter 4, section 2.1.2. The edge of the bridge silhouette was sampled at regular intervals in the axial direction, and the data was subjected to a built-in FFT algorithm in Mathcad®. The fundamental response of the bridge, sin (z/Λ), was subtracted from the image data, and after subtracting out this fundamental frequency component, the third harmonic appears clearly at the acceleration amplitude 0.2 cm/s^2.

(a) (b) (c) (d)

Figure 6.12. Filtered images of a laterally oscillating bridge. (a): $A = 0$ cm/s^2. (b): $A = 0.04$ cm/s^2. (c): $A = 0.1$ cm/s^2. (d): $A = 0.2$ cm/s^2.

5. Conclusions

The nonlinear dynamics of a neutrally buoyant $V = 1$ laterally oscillated liquid bridge have been analyzed. In particular, it has been determined that when the disk supports are laterally oscillated near the first resonant frequency of the bridge, even at low excitation amplitudes, the amount of contact angle motion occurring during oscillation decreases relative to exciting the bridge off-resonance. This is due to the presence of a third harmonic mechanical response of the bridge. This was determined by utilizing the nature of the Fourier transform to identify the spatial modes. There appears to be a qualitative difference in resonant behavior between $\Lambda = 2.6$ and $\Lambda = 2.826$ bridges, and this should be explored further.

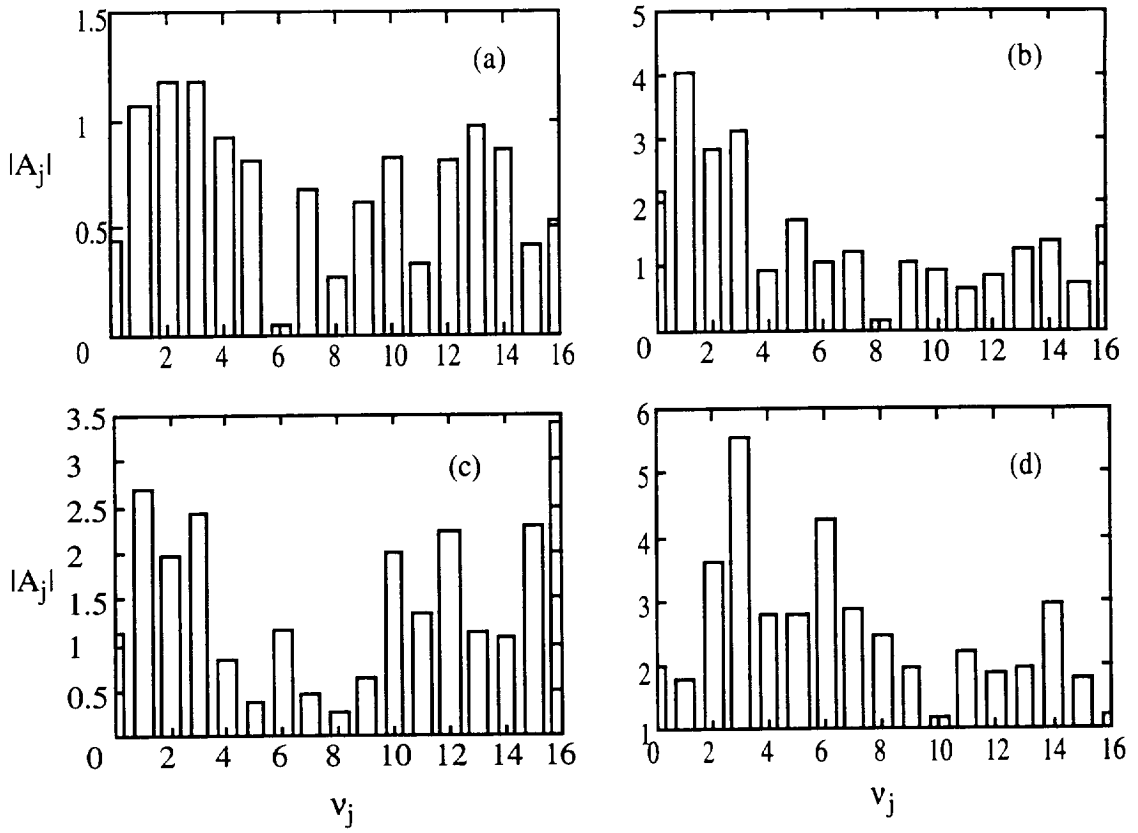

Figure 6.13. FFTs of filtered bridge images (fundamental subtracted). (a): A = 0 cm/s^2. (b): A = 0.04 cm/s^2. (c): A = 0.1 cm/s^2. (d): A = 0.2 cm/s^2.

Chapter 7

LIQUID BRIDGE FORCE MEASUREMENTS

7.1. Introduction

Forces exerted by a liquid bridge on a solid support are important in powder wetting problems, deformations of porous or unconsolidated media, and in adhesion problems [6-10]. Surfaces being studied with Atomic Force Microscopy (AFM) or Scanning Tunneling Microscopy (STM) techniques can be damaged by the formation of a bridge between the sample and the scanning tip [270]. The forces involved are the capillary force due to interfacial tension, and the hydrostatic pressure due to the curvature of the liquid bridge surface. For a liquid bridge held between two coaxial disks, we used a force deflection apparatus to measure the total force exerted by a liquid bridge on the lower disk. The lower disk was replaced with a thin polycarbonate disk which was attached to the end of a long cantilever arm (see Figure 7.1). The cantilever arm acts as a weak spring. The liquid bridge displaces the disk by an amount proportional to the total force, F_{tot}, exerted on the disk. Then, by directly measuring the displacement, we can determine F_{tot}. After calibrating the deflection of the cantilever arm with known applied loads, two sets of experiments were performed. In the first set, the total force was measured for various aspect ratio right circular cylindrical bridges (Bo = 0). This provides a simple method to measure the interfacial energy γ. The second set of experiments involves measuring the force exerted by liquid bridges with a variety of aspect ratios and volumes at different Bond

numbers. The principal question to be answered by this set of experiments is how the force changes as the liquid bridge approaches the minimum volume stability limit. In addition, computations of the force were carried out and the results compared with experimental data

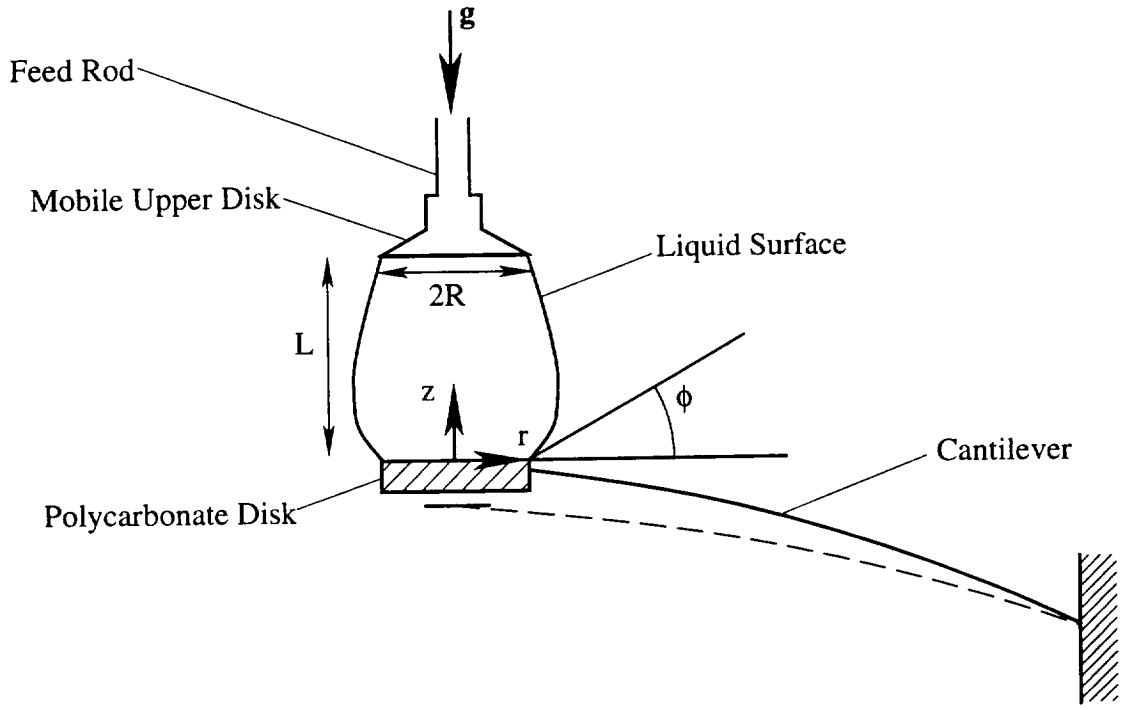

Figure 7.1. Force balance apparatus.

7.2. Theory

For a liquid bridge immersed in a bath, the total force F_{tot} exerted on the lower disk is:

$$F_{tot} = F_{cap} + F_{hydro} \tag{7.1}$$

or:

$$F_{tot} = 2\pi R\gamma \sin\phi - 2\pi R^2 J\gamma \tag{7.2}$$

where R is the radius of the disks, γ is the interfacial energy, ϕ is the contact angle, and J is the mean curvature of the liquid bridge near the lower disk.

For right circular cylindrical bridges, the total force simplifies considerably, as the contact angle is 90 degrees, and one of the principal curvatures is zero. Therefore, for right circular cylindrical (weightless) bridges, the total force is given by:

$$F_{tot} = \pi R\gamma \tag{7.3}$$

The force can be nondimensionalized by dividing by this scale factor, $F = F_{tot}/\pi R\gamma$.

7.3. Apparatus

A steel cantilever arm, length = 8.5 cm, diameter = 0.009 inches (0.0229 cm), was attached to a rigid support at one end and to a 1 cm diameter thin polycarbonate disk at the other (Figure 7.1). The cantilever arm was an electric guitar string (GHS strings) and is a plain steel similar to piano wire or spring steel. To easily track the movement of the disk, a piece of reflective white plastic tubing was located 6.2 cm from the fixed end of the cantilever arm. This piece of plastic diffusely scatters a laser beam, which was collected by a 35 mm single lens reflex camera and an 80 mm macro zoom lens, with a position sensitive photodiode mounted at the film plane of the camera. It was found that the maximum signal to noise ratio was obtained by a combination of maximum zoom and maximum defocus of the lens. This produces the largest spot of light on the photodiode. The photodiode is connected to a United Detector Technology model 431 X-Y position monitor. This position monitor provides separate outputs for position in the x-direction and position in the y-direction. By decoupling the motion in the vertical and horizontal direction, we can ignore the horizontal component of motion due to the fact that the disk moves along a segment of arc and not straight line. Output from the position monitor was sent to a chart recorder. The movement of the reflective plastic was tracked, and thus of

the lower disk. In addition, the liquid bridge was monitored with a CCD video camera connected to a video monitor through a videocassette recorder. This allowed direct measurement of the contact angle on the lower disk, which was used to estimate the amount of capillary force.

To calculate force from the measured deflection, it was assumed that the cantilever arm obeys Hooke's law. This was verified by displacing the disk a known amount and measuring the resultant load. The modulus of elasticity of the cantilever arm was found to be 30.42 x 10^6 psi, or 2.138 x 10^9 g/cm^2, and the effective spring constant was measured to be 137.51 dyne/cm. The force constant is linear over a large range of motion.

7.4. Procedure

7.4.1 Calibration

To calibrate how motion of the disk was related to motion of the chart pen, the lower and upper disks were connected by a thin film of silicone oil. Because the thin film holds the two disks together, the motion of the upper disk equals the motion of the lower disk, in the limit of small displacement. The upper disk was moved by computer controlled stepping motors moving along linear actuators. The precision of movement of the upper disk is 2.05 x 10^{-5} cm. The deflection of the chart pen was recorded and the position was held constant for two minutes to give a stable average reading. For small displacements (less than 0.25 cm) the motion of the pen was a linear function of the disk displacement (see Figure 7.2 a-d). For larger displacements, a quadratic fit is necessary. Two different lasers were tried, a 5 mW HeNe laser and a 15 mW HeNe laser. It was found that the brighter spot of the higher power laser greatly reduced the measurement noise of the position sensitive photodiode. In addition, the 15 mW laser produced a nearly linear relationship between actual disk displacement and chart recorder output. Thus, the higher power laser was used for all experiments. The calibration procedure was performed

for each separate trial run. This is because changes in the relative positions of the photodiode and reflector plastic and changes in the amount of ambient light alter the scale factor for the chart displacement versus disk displacement. As shown on the calibration graphs, although each scale factor is approximately the same (with the exception of the 5 mW laser), the scale factor does change from calibration to calibration.

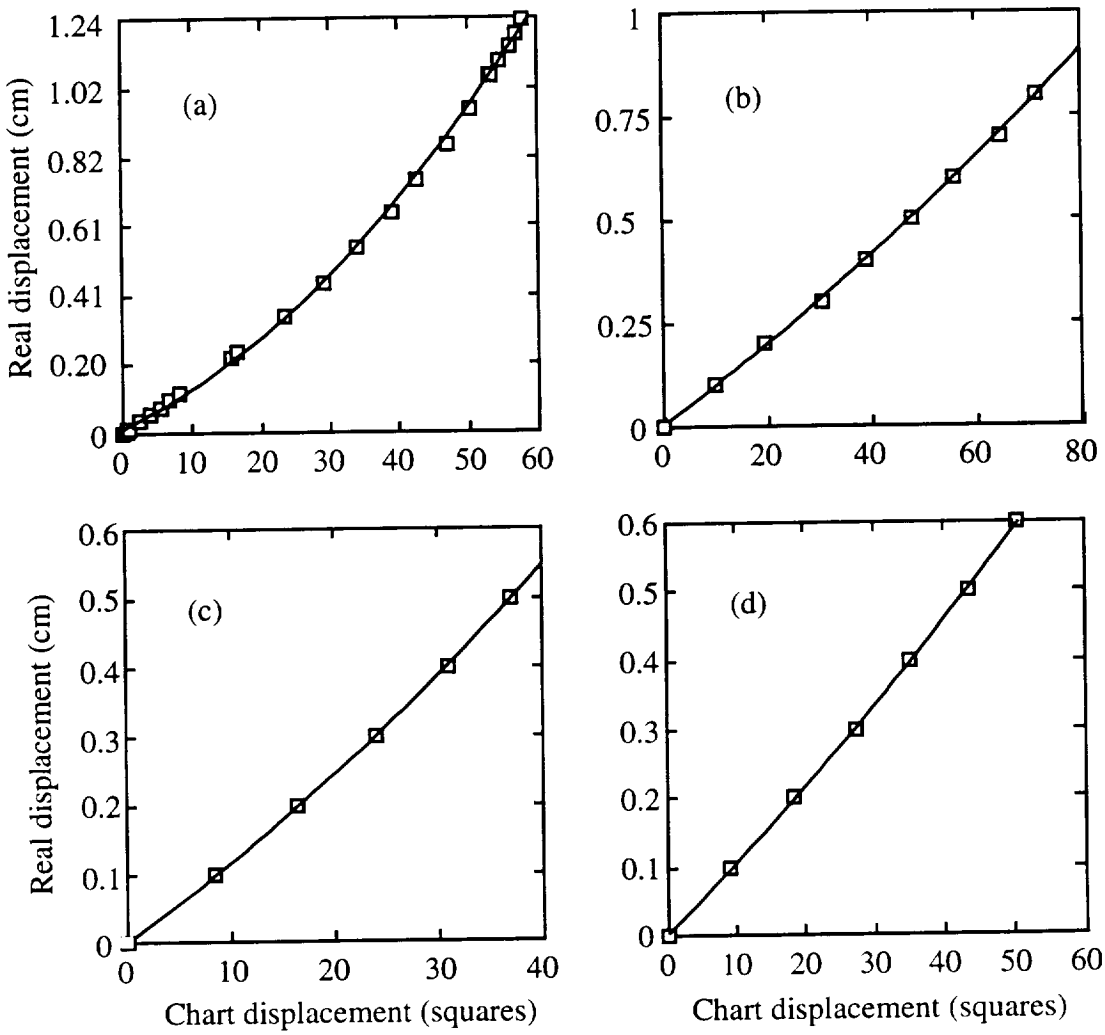

Figure 7.2. Calibration of chart recorder output. (a) 5 mW HeNe laser source. (b) - (d) 15 mW HeNe laser source

7.4.2 Right circular cylindrical bridges

The forces exerted by right circular cylindrical bridges with different aspect ratios were examined. This was done by allowing the cantilever arm to establish its equilibrium position corresponding to the buoyancy force of the disk and wire relative to the bath. This position was recorded on the chart recorder. The upper feed disk was then brought into contact with the lower disk, and adjusted to bring the lower disk back to its equilibrium position. This eliminates any effect caused by the buoyancy of the cantilever arm. The density and temperature of the bath was adjusted to produce nearly neutral bouyancy conditions (see section 3.5.1). Silicone oil was manually injected, and the upper feed disk moved until the bridge appeared to be a right circular cylinder upon visual inspection. The aspect ratio was measured directly from the viewing monitor with a set of calipers, and the displacement of the lower disk measured directly from the chart recorder. For right circular cylinders, the total force on the lower disk reduces to a linear dependence upon the radius of the disk and the interfacial energy. Because the radius of the disk is a constant, the displacement of the lower disk is proportional to the interfacial energy only. This fact was used to measure the interfacial energy γ at low Bo (see section 3.4.3.1.3).

7.4.3 General Liquid Bridge Configurations

The final set of experiments involved mapping out sections of the Λ-V stability region for a given Bond number. Before creating each new bridge, the cantilever arm was brought to its equilibrium position. The computer controlled motors were used to displace the upper disk a specified amount. The microsyringe injected a known amount of silicone fluid. The deflection of the lower disk was continuously recorded for a series of deformations, and the physical parameters of the bridge (volume, aspect ratio) were calculated from records of motor and lower disk movement. A sample of raw output data from the chart recorder is shown below (Figure 7.3), and the data is presented in Figure 7.4. Beginning on the left-hand side, the calibration of disk motion is recorded. The pen

travels from left to right at a speed of 1 in/10 min. The next feature present is the initial location of the lower disk. After the bare disk reaches an equilibrium position, the upper disk is brought into contact with the lower disk, causing a displacement of the lower disk until the oil wets the lower disk. The lower disk is then manually brought back to the original equilibrium position. The three curves each represent a bridge of fixed V_0 subjected to changes in Λ. The numerals indicate how many squares the curve is from equilibrium. The first curve represents (Λ_i, V_i) of (0.338, 1.88), the second, (Λ_i, V_i) of (0.219, 1.16), and the third (Λ_i, V_i) of (0.134, 0.946). Note how as Λ_i decreases, the behavior of the bridge as the minimum volume stability limit is approached becomes more and more exaggerated. At the end of the final sequence the bridge broke. Note that the (Λ, V) values for the first two or three points of the final curve of the raw output lie outside of the stability margin. A possible explanation will be presented at the end of this chapter.

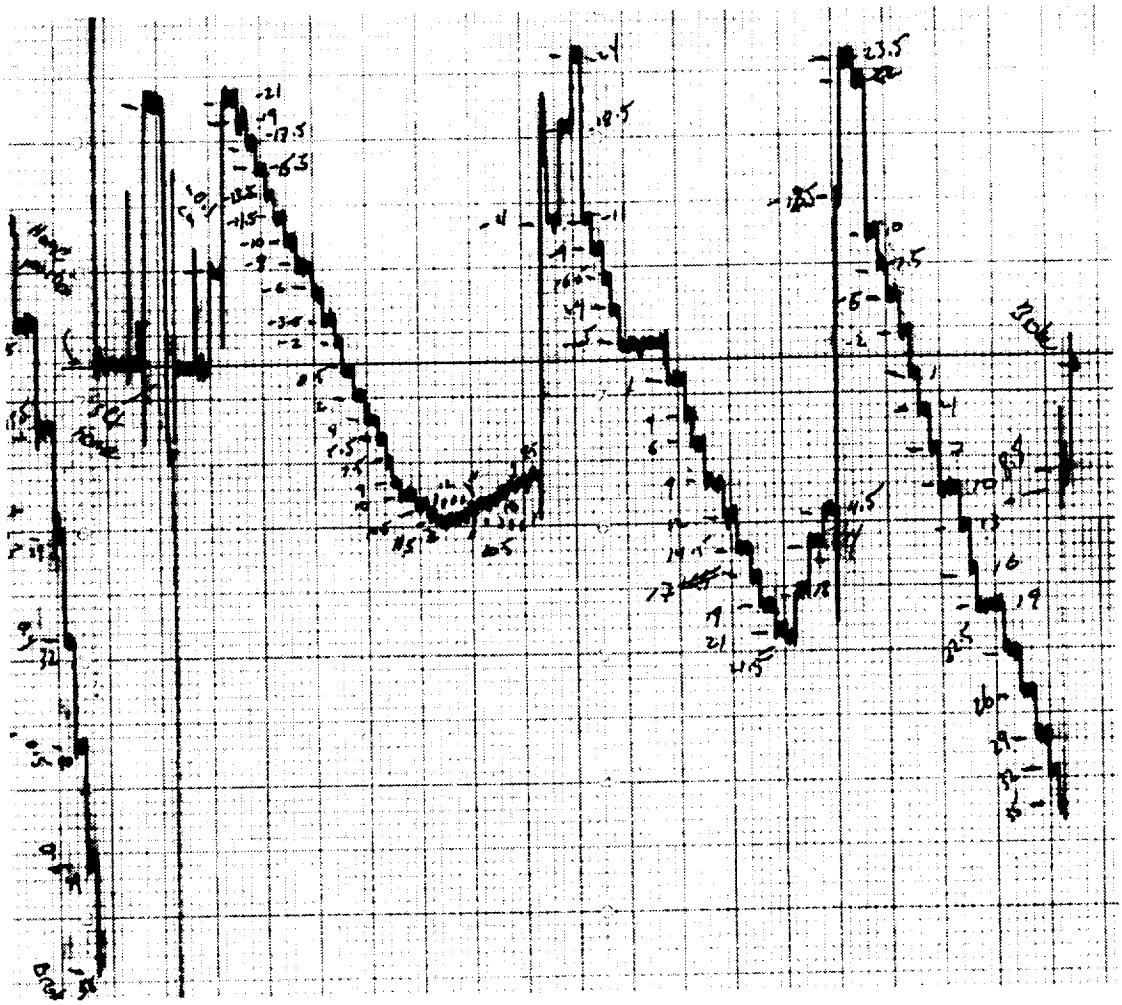

Figure 7.3. Chart recorder output of lower disk deflection

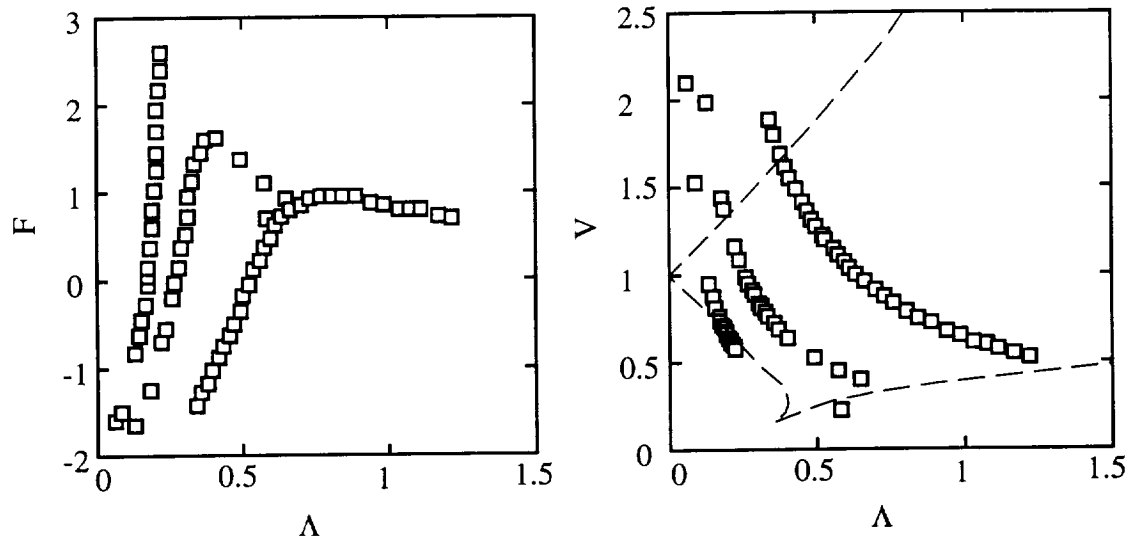

Figure 7.4 . Graphs of F and V against Λ.

There is one striking and unexpected trend in the data. For bridges with small volumes and aspect ratios, the force curve exhibits a maximum upward force before the bridge crosses the minimum volume stability limit. This contrasts with larger bridges that do not exhibit this maximum. We also performed a numerical calculation of the force exerted by the bridge on the lower disk, and the graph is superimposed over the measured data (Figure 7.5). The calculations do not match well at low aspect ratios and high volumes, but the calculation converges with the measured values at larger aspect ratios and smaller volumes. A reason why this may be the case is shown on the graph comparing the measured values of the contact angle with the calculated values (Figure 7.6). There is a large difference between the predicted value of the contact angle and the measured value of the contact angle. The possibility of a volume error in the experiment was investigated. The calculation was performed again, but with a 5% reduction in volume. Although agreement was slightly improved (Figure 7.7), the amount of volume error to completely account for the discrepancy is unrealistic, given the accuracy and precision of the syringe.

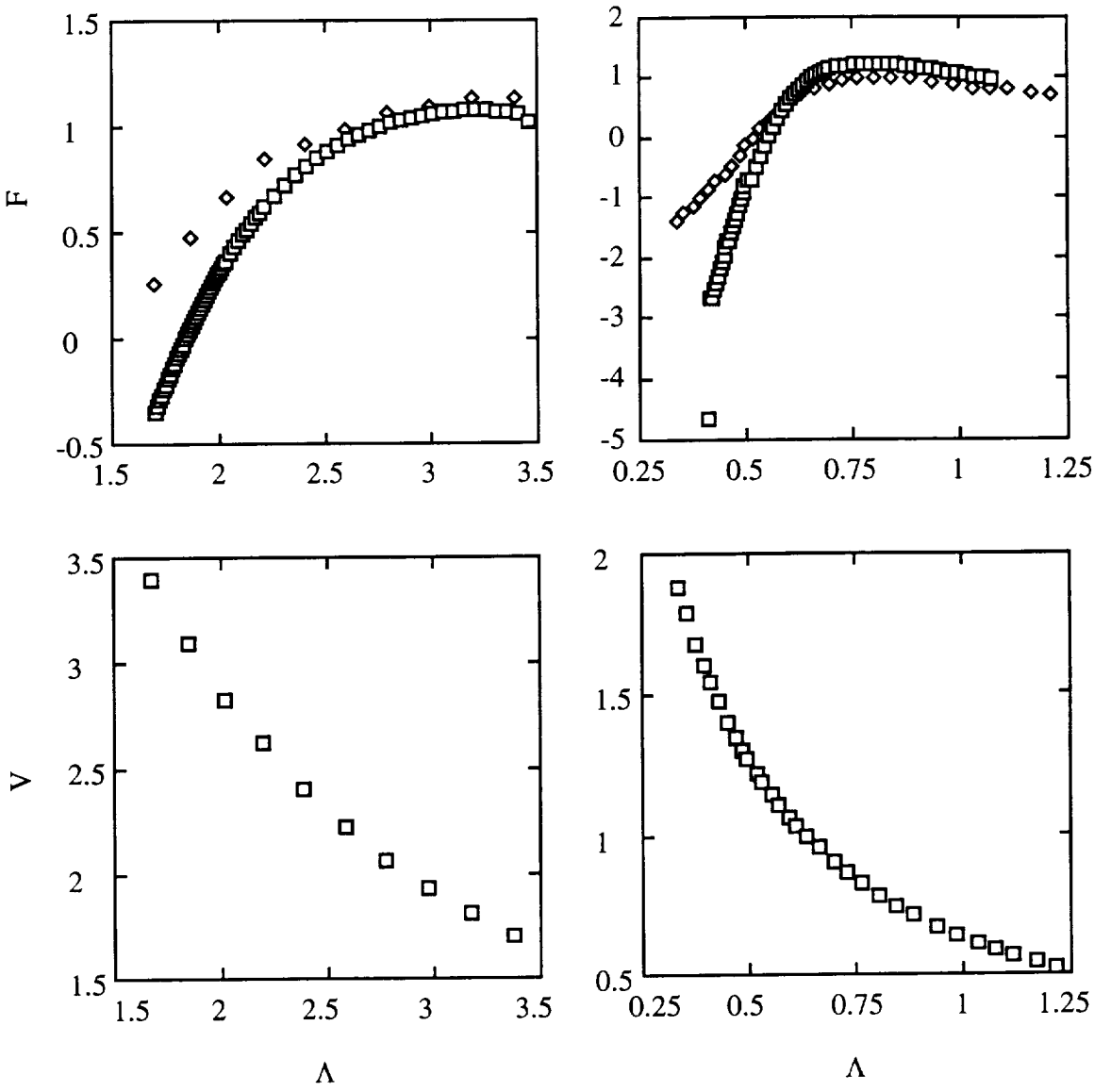

Figure 7.5. Comparison of numerical and experimental results of force measurements. (□) experimental points. (◇) numerical points.

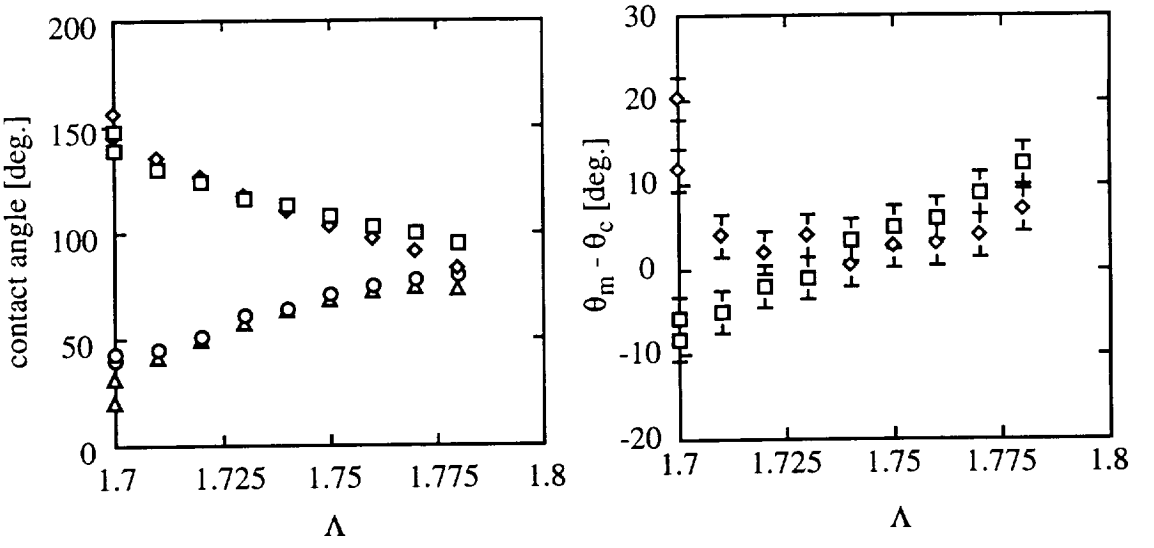

Figure 7.6. Comparison of calculated (θ_c) and measured (θ_m) contact angles. On left: (□) top angle (measured). (○) bottom angle (measured). (◇) top angle (calculated). (△) bottom angle (calculated). On right: (□) top angle. (◇) bottom angle

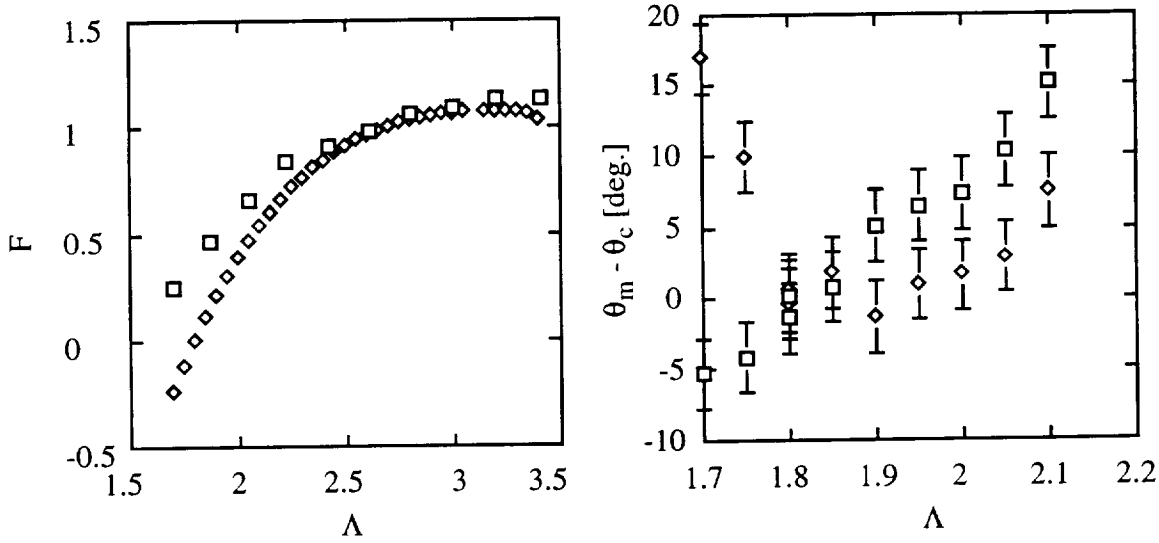

Figure 7.7 Comparison of numerical and experimental results with a 5% decrease of volume in numerical simulation. Force graph: (□) experimental points. (◇) numerical points. Contact angle graph: (□) top angle.
(◇) bottom angle

7.5. Error sources

The primary source of systematic error is due to the fact that the radius of the cantilever disk was not exactly equal to the radius of the upper feed disk. The ratio of disk radii is 0.98, with the cantilever arm disk the larger. This systematic error is 4%, as the pressure and Bo scale as R^2. The next most critical error is the fact that the lower disk does not remain parallel with the upper disk, but instead is at a relative angle to the upper disk. The maximum misalignment is 5 degrees, which corresponds to an error in the capillary force of approximately 0.8%. The resolution and noise level of the chart recorder places an error of ± 0.8 dyne on the total force, which is an error of 5% at typical force values. This is larger than the systematic error. The error in volume is the same as calculated in section 3.6.6, but the error in aspect ratio is related to the error in lower disk displacement, which is given by the resolution of the chart recorder, approximately 0.05 mm of real displacement, corresponding to $\delta\Lambda/\Lambda \approx 5 * 10^{-3}$.

7.6 Conclusions

A series of experiments measured the force exerted by a liquid bridge on the lower support disk. Discrepancies between the numerical results and the experimental results were attributed to differences in computed and measured contact angles. A possible explanation for this is that the contact line is not perfectly pinned on the polycarbonate disk. This would also explain why a few of the bridge configurations lie outside of the stability region. If the contact line had slipped over the edge of the disk, the lower support disk would not be at the proper height. Future experiments with a sharp-edged steel support disk may reconcile the discrepancy. Other future experiments could probe the dynamics of breaking and of drop coalescence.

Chapter 8

SUMMARY AND FUTURE WORK

The static and dynamic behavior of liquid bridges have been studied for this dissertation. New insights have been gained as a result of this work. The effect of support geometry on the stability of axisymmetric liquid bridges has been investigated. The dynamics of liquid bridges laterally oscillating in a neighborhood of the fundamental eigenfrequency has been investigated as well. Lastly, the force an axisymmetric bridge exerts on the lower disk support has been measured for a variety of Λ, V and Bo.

Two new results were obtained through experiments designed to study the effect of support geometry on bridge stability. The effect of Λ on the loss of stability to nonaxisymmetric perturbations has been studied. It was found that there exists a critical Λ, Λ_c, such that if $\Lambda < \Lambda_c$, the bifurcation is subcritical, while for $\Lambda > \Lambda_c$, the bifurcation is supercritical. The effect of K, the disk radii ratio, on axisymmetric bridge stability was also studied. It was found that if gravity is oriented towards the smaller disk, stability is enhanced in the sense that the minimum volume can approach the zero-gravity case for a specific Λ and Bo. We also observed the loss of stability to axisymmetric perturbations along the maximum volume section of the stability curve. The behavior of a bridge in the limiting case $K \rightarrow 0$ was observed for the case $K = 0.09$.

New experimental results were also obtained by laterally oscillating the bridge supports. The dynamic behavior of a $V = 1$ bridge was studied in the neighborhood of the

fundamental eigenfrequency N = 1, m = 1. The response of the bridge to vibration was measured several different ways in an attempt to accurately measure the eigenfrequency and the eigenmode. It was found that the bridge displays nonlinear behavior in both the eigenfrequency and the eigenmode. The eigenfrequency changes with changing excitation amplitude, and the bridge displayes a N = 3, m = 1 shape component on resonance.

The force exerted by a bridge on the lower disk support was measured, with particular attention paid to the behavior near the minimum volume stability limit. Agreement with numerical calculations was hampered by the lack of agreement between measured and calculated contact angles.

Several directions for future investigations suggest themselves. This topic and the experimental apparatus presents a wealth of possibilites for an experimentalist. A few are:

- The stability limits of nonaxisymmetric bridges held between either coaxial or noncoaxial disk supports could be studied.
- We were unable to determine if there is hysteresis that accompanies the subcritical bifurcation, and this topic could be invesitigated in the future.
- Liquid bridges held between spherical supports could be studied to investigate the role of contact line motion, especially during dynamic processes.
- The dynamical process of axisymmetric breaking could be studied.
- Light ray deflection measurement suggest the presence of even higher order terms in the bridge shape, and future experiments could probe for these.
- Dynamical behavior of bridges subject to axial or lateral vibration, rotation or a combination of all of these, with disks moving in or out of phase at either identical or different amplitudes and frequencies.
- Further force balance experiments with a sharp-edged steel disk support instead of the thick plastic disk should produce better agreement between numerical calculations and experiment.

- The force balance apparatus could be used to explore problems in drop coalescence and film pressure.

APPENDICES

Appendix A.

BACKGROUND OF TENSOR CALCULUS

Because most of the mathematics involved in fluid dynamics involve tensors, it is fruitful to quickly review the nomenclature and any important theorems. Two basic concepts to be reviewed are the use of the metric tensor to raise and lower indices and the covariant, also called total or material, derivative. In general, the notation in [271] is followed (see [271,272] for a more thorough development).

In general, a tensor may written in bold without subscripts, as **T**. However, to be more explicit, the indices may be written as well: $T^{abc...m}_{pqr...z}$. A repeated index, as $T_{ij}V^j$, indicates a sum or inner product over the repeated index, called a dummy index. There are three types of tensor components: contravariant, covariant, and mixed. A contravariant component of a tensor transforms under coordinate transformations as:

$$V^i = \frac{\partial x^i}{\partial x^j} V^j \tag{A.1}$$

while a covariant component of a tensor transforms as:

$$V_i = \frac{\partial x^j}{\partial x^i} V_j \tag{A.2}$$

An example of a contravariant quantity is displacement, and an example of a covariant quantity is gradient. A mixed tensor component transforms as expected,

$$T^i_j = \frac{\partial x^i}{\partial x^m}\frac{\partial x^n}{\partial x^j}T^m_n \tag{A.3}$$

In general, contravariant and covariant components are very different entities. The indices may not be moved up or down at whim. This is because there are two equivalent ways of explicitly writing $\mathbf{V}$, $\mathbf{V} = V^i\mathbf{e}_i = V_i\boldsymbol{\omega}^i$. The first expression expresses $\mathbf{V}$ in terms of a basis set of vectors, $\mathbf{e}_i$, where the superscript refers to the i^{th} vector, not the i^{th} component. The second expression involves the dual to the basis vectors, called 1-forms. It is important to note that V^i and V_i are in general entirely unrelated to each other. However, in a Riemannian space, when we have a metric tensor defined, they both refer to the same geometrical object $\mathbf{V}$. Then, if V^i is known, V_i can be determined. A summation (inner product) may only occur between a contravariant and a covariant component. In the restricted case of Euclidean (flat) space, indexes may be raised or lowered arbitrarily. The tensor that allows us to move indices is the metric tensor g_{ij}:

$$ds^2 = g_{ij}dx^i dx^j \tag{A.4}$$

where ds^2 is the square of the line element between infinitesimally separated points. We define the contravariant tensor g^{ij} as: $g^{in}g_{jn} = \delta^i_j$. Indices can now be raised or lowered, for example,

$$V_i = g_{ij}V^j,\ V^i = g^{ij}V_j. \tag{A.5}$$

A second important concept is the covariant derivative. This is different from a partial differentiation, which is written as follows:

$$\partial_k T^i_j \equiv \partial_{\mathbf{e}_k} T^i_j = \frac{\partial T^i_j}{\partial x^k} = T^i_{j,k} \tag{A.6}$$

However, in curved space, $\nabla \mathbf{T} \neq T^i_{j,k}$. This is because the basis $\mathbf{e}_i$ (as well as the 1-form, $\boldsymbol{\omega}^j$) varies smoothly from point to point. $\nabla \mathbf{T} = \nabla_k \left(T^i_j \mathbf{e}_i \otimes \boldsymbol{\omega}^j \right)$ will contain additional contributions from $\nabla \mathbf{e}_i$ and $\nabla \boldsymbol{\omega}^j$. To handle these contributions, "connection coefficients" (Christoffel coefficients of the first kind) are defined: $\Gamma^i_{jk} = \left\langle \boldsymbol{\omega}^i, \nabla_k \mathbf{e}_j \right\rangle$. This represents the i^{th} component of change in $\mathbf{e}_j$ relative to parallel transport along $\mathbf{e}_k$. The covariant derivative of a tensor can now be calculated:

$$\begin{aligned} \nabla \mathbf{T} &= \nabla_k \left(T^i_j \mathbf{e}_i \otimes \boldsymbol{\omega}^j \right) \\ &= \nabla_k \left(T^i_j \right) \mathbf{e}_i \otimes \boldsymbol{\omega}^j + T^i_j \nabla_k \left(\mathbf{e}_i \right) \otimes \boldsymbol{\omega}^j + T^i_j \mathbf{e}_i \otimes \nabla_k \left(\boldsymbol{\omega}^j \right) \\ &= T^i_{j,k} \mathbf{e}_i \otimes \boldsymbol{\omega}^j + T^i_j \Gamma^n_{ik} \mathbf{e}_n \otimes \boldsymbol{\omega}^j - \Gamma^j_{nk} T^i_j \mathbf{e}_i \otimes \boldsymbol{\omega}^n \\ &= \left\{ T^i_{j,k} + T^m_j \Gamma^i_{mk} - \Gamma^m_{jk} T^i_m \right\} \mathbf{e}_i \otimes \boldsymbol{\omega}^j \end{aligned} \tag{A.7}$$

where the expressions for the connection coefficients have been re-written as:

$$\Gamma^n_{jk} \mathbf{e}_n = \nabla_k \mathbf{e}_j, \quad \Gamma^i_{jk} \boldsymbol{\omega}^j = -\nabla_k \boldsymbol{\omega}^i \tag{A.8}$$

The definition of a covariant derivative, written as $T^i_{j|k}$ is:

$$\nabla \mathbf{T} \equiv T^i_{j|k} = T^i_{j,k} + \Gamma^i_{mk} T^m_j - \Gamma^m_{jk} T^i_m \tag{A.9}$$

Similarly, the covariant derivative of a tensor of rank one is written:

$$\nabla \mathbf{V} \equiv V^{i}_{|j} = V^{i}_{,j} + \Gamma^{i}_{mj} V^{m} \qquad (A.10)$$
$$\nabla \mathbf{V} \equiv V_{i|j} = V_{i,j} - \Gamma^{m}_{ij} V_{m}$$

where the connection coefficients can also be written explicitly [257]:

$$\Gamma^{i}_{jk} = g^{im}\Gamma_{mjk} = g^{im}\frac{1}{2}\left(g_{mj,k} + g_{mk,j} - g_{jk,m}\right). \qquad (A.11)$$

Appendix B.

THE NAVIER-STOKES EQUATIONS

It is beyond the scope of this dissertation to completely cover the development of axisymmetric flow problems and flow problems involving a free boundary, but a short review of important and related concepts will be presented here and in appendices C, D. For a more comprehensive discussion, see for example [273-278].

The basic equations governing fluid flow are derived from first priciples: the Navier-Stokes system of equations. Then, the specific Navier-Stokes equations in (r,θ,z) coordinates are written. It is insightful to keep in mind that the Navier-Stokes equations are simply conservation equations, recast into a different coordinate system. Typically, in problems involving solid bodies, Lagrangian coordinates are used. These are also refered to as material coordinates, and written in upper case. Here, the position vector $\mathbf{R}$ of a particle at time "t" is given as

$$\mathbf{R} = \mathbf{R}(\mathbf{r},t) \tag{B.1}$$

where $\mathbf{r}$ is the position vector from the origin to a point $\mathbf{R}_o$ at time $t = t_o$. The velocity of the particle is defined as

$$\mathbf{V}(\mathbf{r},t) = \frac{\partial \mathbf{R}}{\partial t} = \frac{\partial}{\partial t}[\mathbf{r} + \mathbf{U}(\mathbf{r},t)] = \frac{\partial \mathbf{U}}{\partial t} = \mathbf{U}_{,t} \tag{B.2}$$

where **U** is a displacement vector, **U** = **R**(**r**,t) - **r** and **r** is independent of time. By contrast, Eulerian coordinates, or spatial coordinates, (written in lower case) co-move with fluid "particles", and **u** = **R** - **r**(**R**,t). Because these variables change with both time and position, the temporal derivative changes to the total derivative:

$$\mathbf{v} = \frac{D\mathbf{u}}{Dt} = \left(\frac{\partial}{\partial t} + \mathbf{v}\cdot\nabla\right)\mathbf{u} = \mathbf{u}_{|t} \tag{B.3}$$

The first law of Thermodynamics in Eulerian coordinates is written as:

$$\frac{DK}{Dt} + \frac{DU}{Dt} = M + Q \tag{B.4}$$

where K is the kinetic energy, U the potential energy, M is mechanical power, and Q is heat energy. Consider a bounded volume of fluid, so that

$$K = \frac{1}{2}\iiint_{\Omega}\rho v^i v_i d\Omega \tag{B.5}$$

$$U = \iiint_{\Omega}\rho\varepsilon d\Omega \tag{B.6}$$

$$M = \iiint_{\Omega}\rho F^i v_i d\Omega + \iint_{\Sigma} T^{ij} n_i v_j d\Sigma \tag{B.7}$$

$$Q = \iiint_{\Omega}\rho h d\Omega + \iint_{\Sigma} q^i n_i d\Sigma \tag{B.8}$$

where ρ is the density, ε the internal energy density, **F** a body force, **T** the surface traction, **n** the surface (outward pointing) normal, h the heat density and **q** the heat flux (**F**, **T** are also in Eulerian coordinates). By using the divergence theorem and Reynolds transport theorem (see Appendix C), noting that

$$\frac{D\,J}{Dt} = (\nabla \cdot \mathbf{v})\,J \tag{B.9}$$

where J is the Jacobian:

$$J = \left| \frac{\partial x^i}{\partial x'^j} \right| \tag{B.10}$$

the following are obtained by substitution,

$$\begin{aligned}
\frac{DK}{Dt} &= \iiint_\Omega \frac{D}{Dt}\left(\frac{\rho}{2} v^i v_i\right) d\Omega + \iiint_\Omega \frac{\rho}{2} v^i v_i \frac{D d\Omega}{Dt} \qquad \text{(B.11)} \\
&= \iiint_\Omega \frac{\partial}{\partial t}\left(\frac{\rho}{2} v^i v_i\right) d\Omega + \iiint_\Omega \mathbf{v} \cdot \nabla\left(\frac{\rho}{2} v^i v_i\right) d\Omega + \iiint_\Omega \frac{\rho}{2} v^i v_i (\nabla \cdot \mathbf{v}) d\Omega \\
&= \frac{1}{2} \iiint_\Omega \left[\frac{\partial}{\partial t}\left(\rho v^i v_i\right) + \left(\rho v^i v_i\right)_{|j} v^j + \rho v^i v_i v^j_{|j} \right] d\Omega \\
&= \frac{1}{2} \iiint_\Omega \left[v^i v_i \frac{\partial \rho}{\partial t} + \rho \frac{\partial}{\partial t}\left(v^i v_i\right) + \rho_{|j} v^i v_i v^j + \rho\left(v^i v_i\right)_{|j} v^j + \rho v^i v_i v^j_{|j} \right] d\Omega \\
&= \iiint_\Omega \left[\frac{1}{2} v^i v_i \left(\frac{\partial \rho}{\partial t} + \left(\rho v^j\right)_{|j} \right) + v_i \left(\rho \frac{\partial v^i}{\partial t} + \rho v^i_{|j} v^j \right) \right] d\Omega
\end{aligned}$$

where the following relation is used:

$$\begin{aligned}
v^i \frac{\partial v_i}{\partial t} &= g^{ij} v_j \frac{\partial\left(g_{ik} v^k\right)}{\partial t} \qquad \text{(B.12)} \\
&= g^{ij} g_{ik} v_j \frac{\partial v^k}{\partial t} \\
&= \delta^j_k v_j \frac{\partial v^k}{\partial t} \\
&= v_j \frac{\partial v^j}{\partial t} \qquad .
\end{aligned}$$

Similarly, for the internal energy:

$$\frac{DU}{Dt} = \iiint_\Omega \left[\left(\rho \frac{\partial \varepsilon}{\partial t} + \rho \varepsilon_{|i} v^i \right) + \varepsilon \left(\frac{\partial \rho}{\partial t} + \left(\rho v^i \right)_{|i} \right) \right] d\Omega \tag{B.13}$$

thus, by grouping terms, the following is obtained:

$$\begin{aligned} &\iiint_\Omega E \left(\frac{\partial \rho}{\partial t} + (\rho v^i)_{|i} \right) d\Omega \\ &+ \iiint_\Omega v_j \left(\rho \frac{\partial v^j}{\partial t} + \rho v^j_{|i} v^i - \rho F^j - T^{ij}_{|i} \right) d\Omega \\ &+ \iiint_\Omega \left(\rho \frac{\partial \varepsilon}{\partial t} + \rho \varepsilon_{|i} v^i - T^{ij} v_{j|i} - q^i_{|i} - \rho h \right) d\Omega = 0 \end{aligned} \tag{B.14}$$

where $E = \varepsilon + 1/2\ v^i v_i$.

In order for this relation to hold, each of the integrands must vanish. That is,

$$\begin{aligned} &\text{(conservation of mass)} && \frac{\partial \rho}{\partial t} + (\rho v^i)_{|i} = 0, \\ &\text{(conservation of momentum)} && \rho \frac{\partial v^j}{\partial t} + \rho v^j_{|i} v^i - \rho F^j - T^{ij}_{|i} = 0, \\ &\text{(conservation of energy)} && \rho \frac{\partial \varepsilon}{\partial t} + \rho \varepsilon_{|i} v^i - T^{ij} v_{j|i} - q^i_{|i} - \rho h = 0. \end{aligned} \tag{B.15}$$

In the more familiar notation, this becomes:

$$\begin{aligned} \frac{\partial \rho}{\partial t} + \nabla \cdot (\rho \mathbf{v}) &= 0 \\ \rho \frac{D\mathbf{v}}{Dt} - \rho \mathbf{F} - \nabla \cdot \mathbf{T} &= 0 \\ \rho \frac{D\varepsilon}{Dt} - \mathbf{T} \cdot (\nabla \mathbf{v})^T - \nabla \cdot \mathbf{q} - \rho h &= 0 \end{aligned} \tag{B.16}$$

In order to reduce the conservation of momentum and energy equations into a more tractable form, the stress tensor T_{ij} is analyzed. Stokes proposed in 1845 [279] that the stress tensor should be of the form $T_{ij} = -\Pi\delta_{ij} + \boldsymbol{f}(d_{ij})$, where Π is the thermodynamic (isotropic) pressure and $\boldsymbol{f}(d_{ij})$ is a function of the rate-of-deformation tensor $d_{ij} = 1/2(v_{i|j} + v_{j|i})$. The generalized form of Hooke's law for linear elasticity is:

$$f_{ij} = E_{ijkm}d^{km}. \tag{B.17}$$

where the most general form of E_{ijkm} for an isotropic medium is

$$E_{ijkm} = \lambda\delta_{ij}\delta_{km} + \mu(\delta_{ik}\delta_{jm}+\delta_{im}\delta_{kj}) + \xi(\delta_{ik}\delta_{jm}-\delta_{im}\delta_{kj}) \tag{B.18}$$

Recall that f_{ij} must be symmetric. Thus,

$$E_{ijkm} = E_{jikm} = E_{kmij} = E_{jimk} \rightarrow \xi = 0 \tag{B.19}$$

The explicit form of $\boldsymbol{f}$ can be written as :

$$f_{ij} = E_{ijkm}d^{km} = (\lambda\delta_{ij}\delta_{km} + \mu(\delta_{ik}\delta_{jm}+\delta_{im}\delta_{kj}))d^{km} \tag{B.20}$$

or more simply as $f_{ij} = \lambda d^k_k\delta_{ij} + 2\mu d_{ij}$. λ is called the dilatational viscosity, and μ is the shear viscosity. To relate the two constants, note that the mean pressure is proportional to the trace of the stress tensor. That is, $T^i_i = -3p = -3\Pi + 3\lambda d^i_i + 2\mu d^i_i$ or $\Pi - p = \left(\lambda + \frac{2}{3}\mu\right)d^i_i$. Because the thermodynamic pressure is nearly equal to the mean pressure (for quasi-static processes), $\lambda = -\frac{2}{3}\mu$. Thus, the dilatational viscosity can be

eliminated and instead write $T_{ij} = -p\delta_{ij} + f_{ij}$, where $f_{ij} = 2\mu\left(d_{ij} - \frac{1}{3}d^k_k\delta_{ij}\right)$. Thus, the term $\nabla \cdot \mathbf{T}$ is re-written as $-\nabla p + \mu\nabla^2\mathbf{v}$ for incompressible fluids.

The conservation of momentum equation in cylindrical coordinates for an isotropic incompressible fluid in the prescence of gravity can now be written. Also required are the non-zero connection coefficients:

$$\Gamma^r_{\theta\theta} = -r \qquad \Gamma^\theta_{\theta r} = \Gamma^\theta_{r\theta} = \frac{1}{r} \tag{B.21}$$

This provides the general Navier-Stokes equations in (r, θ, z) coordinates:

(r-component)

$$\rho\left(\frac{\partial v_r}{\partial t} + v_r\frac{\partial v_r}{\partial r} - \frac{v_\theta^2}{r} + v_\theta\frac{1}{r}\frac{\partial v_r}{\partial \theta} + v_z\frac{\partial v_r}{\partial z}\right) = -\frac{\partial p}{\partial r} + \mu\left[\frac{\partial}{\partial r}\left(\frac{1}{r}\frac{\partial}{\partial r}(rv_r)\right) + \frac{1}{r}\frac{\partial^2 v_r}{\partial \theta^2} - \frac{2}{r^2}\frac{\partial v_\theta}{\partial \theta} + \frac{\partial^2 v_r}{\partial z^2}\right] \tag{B.22}$$

(z-component)

$$\rho\left(\frac{\partial v_z}{\partial t} + v_r\frac{\partial v_z}{\partial r} + v_\theta\frac{1}{r}\frac{\partial v_z}{\partial \theta} + v_z\frac{\partial v_z}{\partial z}\right) = -\frac{\partial p}{\partial z} + \mu\left[\frac{1}{r}\frac{\partial}{\partial r}\left(r\frac{\partial v_z}{\partial r}\right) + \frac{1}{r^2}\frac{\partial^2 v_z}{\partial \theta^2} + \frac{\partial^2 v_z}{\partial z^2}\right] + \rho g_z \tag{B.23}$$

(θ-component)

$$\rho\left(\frac{\partial v_\theta}{\partial t} + v_r\frac{\partial v_\theta}{\partial r} + \frac{v_r v_\theta}{r} + v_\theta\frac{1}{r}\frac{\partial v_\theta}{\partial \theta} + v_z\frac{\partial v_\theta}{\partial z}\right) = -\frac{1}{r}\frac{\partial p}{\partial \theta} + \mu\left[\frac{\partial}{\partial r}\left(\frac{1}{r}\frac{\partial(rv_\theta)}{\partial r}\right) + \frac{1}{r^2}\frac{\partial^2 v_\theta}{\partial \theta^2} + \frac{2}{r^2}\frac{\partial v_r}{\partial \theta} - \frac{v_\theta}{r^2} + \frac{\partial^2 v_\theta}{\partial z^2}\right] \tag{B.24}$$

and the conservation of mass equation

$$\frac{1}{r}\frac{\partial(rv_r)}{\partial r} + \frac{1}{r}\frac{\partial v_\theta}{\partial \theta} + \frac{\partial v_z}{\partial z} = 0 \tag{B.25}$$

This can be greatly simplified by considering only axisymmetric flows. The equations reduce to:

$$\text{(r-component)}\,\rho\left(\frac{\partial v_r}{\partial t}+v_r\frac{\partial v_r}{\partial r}-\frac{v_\theta^2}{r}+v_z\frac{\partial v_r}{\partial z}\right)=-\frac{\partial p}{\partial r}+\mu\left[\frac{\partial}{\partial r}\left(\frac{1}{r}\frac{\partial}{\partial r}(rv_r)\right)+\frac{\partial^2 v_r}{\partial z^2}\right] \quad \text{(B.26)}$$

$$\text{(z-component)}\,\rho\left(\frac{\partial v_z}{\partial t}+v_r\frac{\partial v_z}{\partial r}+v_z\frac{\partial v_z}{\partial z}\right)=-\frac{\partial p}{\partial z}+\mu\left[\frac{1}{r}\frac{\partial}{\partial r}\left(r\frac{\partial v_z}{\partial r}\right)+\frac{\partial^2 v_z}{\partial z^2}\right]+\rho g_z \quad \text{(B.27)}$$

$$\text{(}\theta\text{-component)}\,\rho\left(\frac{\partial v_\theta}{\partial t}+v_r\frac{\partial v_\theta}{\partial r}+\frac{v_r v_\theta}{r}+v_z\frac{\partial v_\theta}{\partial z}\right)=\mu\left[\frac{\partial}{\partial r}\left(\frac{1}{r}\frac{\partial(rv_\theta)}{\partial r}\right)+\frac{\partial^2 v_\theta}{\partial z^2}\right] \quad \text{(B.28)}$$

$$\text{(Conservation of mass)}\qquad \frac{\partial v_z}{\partial z}+\frac{1}{r}\frac{\partial(rv_r)}{\partial r}=0. \quad \text{(B.29)}$$

For fluids at a constant temperature, the conservation of energy equation is trivial. For numerical computations, the Navier-Stokes equations are usually written in dimensionless form, by introducing the Reynolds number $\rho vR/\mu$.

$$\frac{Dv}{Dt}-\mathbf{F}+\frac{1}{\rho}\nabla p-\frac{1}{Re}\nabla^2\mathbf{v}=0 \quad \text{(B.30)}$$

Appendix C.

BOUNDARY CONDITIONS ACROSS SURFACES OF DISCONTINUITY

The boundary conditions that occur at a surface of discontinuity between two distinct volume regions are derived. The kinematic boundary condition for a moving surface of discontinuity is then derived.

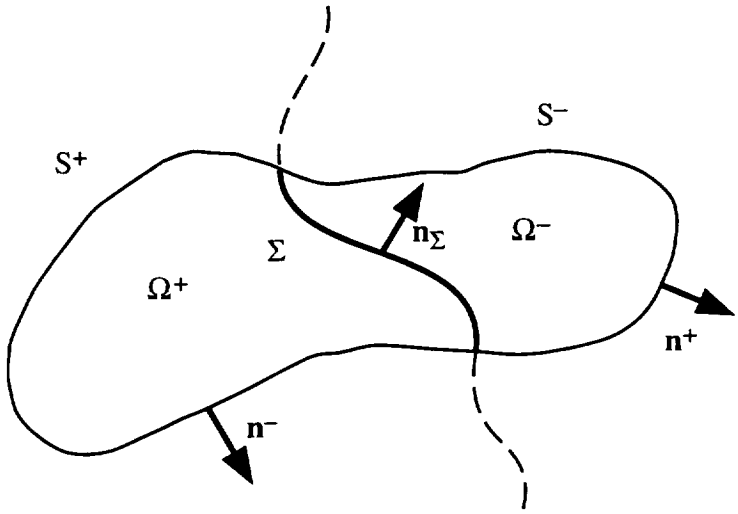

Figure C.1. Schematic of a surface of discontinuity.

A region Ω with a surface of discontinuity Σ is defined (see Figure C.1). Σ divides Ω into Ω^+ and Ω^-. The region $\Omega^\pm$ is bounded by $S^\pm$ and Σ. Also defined is

$\partial\Omega^{\pm} = \Sigma \cup S^{\pm}$. For any point $\mathbf{a} \in \Sigma$ a function F (a quantity to be balanced across the interface) is defined as:

$$F = \int_{\Omega(t)} \rho f \, d\Omega \tag{C.1}$$

$$\begin{aligned} F^{\pm}(\mathbf{a},t) &= \lim_{\mathbf{r}^{\pm} \to \mathbf{a}} F^{\pm}(\mathbf{r},t) \\ [F(\mathbf{a},t)] &= F^{+}(\mathbf{a},t) - F^{-}(\mathbf{a},t) \end{aligned} \tag{C.2}$$

where $[F(\mathbf{a},t)]$ represents the jump of F across the interface Σ. Also defined are the velocities $\mathbf{v}_s$ of the surfaces $S^{\pm}$ and Σ:

$$\begin{aligned} \mathbf{v}_s^{+}(\mathbf{r},t) &= \mathbf{v}^{+}(\mathbf{r}(\mathbf{R},t),t) = \dot{\mathbf{r}}^{+} \quad \text{on } S^{+} \\ \mathbf{v}_s^{-}(\mathbf{r},t) &= \mathbf{v}^{-}(\mathbf{r}(\mathbf{R},t),t) = \dot{\mathbf{r}}^{-} \quad \text{on } S^{-} \\ \mathbf{v}_s^{+} \cdot \mathbf{n}_{\Sigma} &= \mathbf{v}_s^{-} \cdot \mathbf{n}_{\Sigma} = v_n \quad \text{on } \Sigma \end{aligned} \tag{C.3}$$

where $\mathbf{v}$ is the velocity of the fluid particles. The total time rate of change of the quantity F is:

$$\frac{D}{Dt} \int_{\Omega(t)} \rho f \, d\Omega = \frac{D}{Dt} \int_{\Omega^{+}(t)} \rho^{+} f^{+} \, d\Omega + \frac{D}{Dt} \int_{\Omega^{-}(t)} \rho^{-} f^{-} \, d\Omega \tag{C.4}$$

which is split up into Ω^{+} and Ω^{-} regions. For each region,

$$\begin{aligned} \frac{D}{Dt} \int_{\Omega^{+}(t)} \rho^{+} f^{+} \, d\Omega &= \int_{\Omega^{+}(t)} \frac{\partial}{\partial t}\left(\rho^{+} f^{+}\right) d\Omega + \int_{S^{+}(t)} \rho^{+} f^{+} \mathbf{v}^{+} \cdot \mathbf{n}^{+} \, d\Sigma - \int_{\Sigma(t)} \rho^{+} f^{+} v_n \, d\Sigma \\ &= \int_{\Omega^{+}(t)} \frac{\partial}{\partial t}\left(\rho^{+} f^{+}\right) d\Omega + \int_{\partial\Omega^{+}(t)} \rho^{+} f^{+} \mathbf{v}^{+} \cdot \mathbf{n}^{+} \, d\Sigma - \int_{\Sigma(t)} \rho^{+} f^{+} s_n^{+} \, d\Sigma \end{aligned} \tag{C.5}$$

and

$$\frac{D}{Dt}\int_{\Omega^-(t)}\rho^-f^-\,dv_{\bar{x}} = \int_{\Omega^-(t)}\frac{\partial}{\partial t}\left(\rho^-f^-\right)d\Omega + \int_{S^-(t)}\rho^-f^-\mathbf{v}^-\cdot\mathbf{n}^-\,d\Sigma + \int_{\Sigma(t)}\rho^-f^-v_n\,d\Sigma \qquad (C.6)$$
$$= \int_{\Omega^-(t)}\frac{\partial}{\partial t}\left(\rho^-f^-\right)d\Omega + \int_{\partial\Omega^-(t)}\rho^-f^-\mathbf{v}^-\cdot\mathbf{n}^-\,d\Sigma + \int_{\Sigma(t)}\rho^-f^-s_n^-\,d\Sigma$$

where $s_n^{\pm} = v_n - \mathbf{v}^{\pm}\cdot\mathbf{n}_\Sigma$ is the relative normal velocity of the interface Σ, compared to the velocity of the interfaces $S^{\pm}$. Note that for a material surface of discontinuity, $s_n = 0$. The Reynolds transport theorem is used as well:

$$\frac{D}{Dt}F = \frac{D}{Dt}\left(\int_{\Omega(t)}\rho f\,d\Omega\right) \qquad (C.7)$$
$$= \frac{D}{Dt}\left(\int_{\Omega(0)}\rho fJ\,d\Omega\right)$$
$$= \int_{\Omega(0)}\frac{D}{Dt}(\rho fJ)\,d\Omega$$
$$= \int_{\Omega(0)}\left(fJ\frac{D\rho}{Dt} + \rho J\frac{Df}{Dt} + \rho f\frac{DJ}{Dt}\right)d\Omega$$
$$= \int_{\Omega(0)}\left(f\frac{D\rho}{Dt} + \rho\frac{Df}{Dt} + \rho f\nabla\cdot\mathbf{v}\right)J\,d\Omega$$
$$= \int_{\Omega(t)}\left(f\frac{D\rho}{Dt} + \rho\frac{Df}{Dt} + \rho f\nabla\cdot\mathbf{v}\right)d\Omega$$
$$= \int_{\Omega(t)}\left(\frac{\partial}{\partial t}(\rho f) + \nabla\cdot(\rho f\mathbf{v})\right)d\Omega$$
$$= \int_{\Omega(t)}\frac{\partial}{\partial t}(\rho f)\,d\Omega + \int_{\Sigma(t)}\rho f\mathbf{v}\cdot\mathbf{n}\,d\Sigma$$

Adding together the contribution from each region $\Omega^{\pm}$,

$$\frac{D}{Dt}\int_{\Omega(t)}\rho f\,d\Omega = \int_{\Omega^+(t)}\frac{\partial}{\partial t}\left(\rho^+ f^+\right)d\Omega + \int_{\Omega^-(t)}\frac{\partial}{\partial t}\left(\rho^- f^-\right)d\Omega + \int_{\partial\Omega^+(t)}\rho^+ f^+ \mathbf{v}^+\cdot\mathbf{n}^+\,d\Sigma + \int_{\partial\Omega^-(t)}\rho^- f^- \mathbf{v}^-\cdot\mathbf{n}^-\,d\Sigma - \int_{\Sigma(t)}[\rho f s_n]\,d\Sigma \tag{C.8}$$

or, alternatively,

$$\frac{D}{Dt}\int_{\Omega(t)}\rho f\,d\Omega = \int_{\Omega(t)}\rho\frac{Df}{Dt}\,d\Omega - \int_{\Sigma(t)}[\rho f s_n]\,d\Sigma. \tag{C.9}$$

Thus, the total time rate of change of a quantity F has a contribution from the bulk region Ω as well as a contribution from the dividing surface Σ.

The following balance law for regions with a surface of discontinuity is now postulated seperately:

$$\frac{D}{Dt}\int_{\Omega(t)}\rho f\,d\Omega = \int_{\Omega(t)}\rho Q\,d\Omega - \int_{\partial\Omega(t)}\mathbf{j}\cdot\mathbf{n}\,d\Sigma + \int_{\Sigma(t)} g\,d\Sigma \tag{C.10}$$

where Q is a source in the bulk region, g is a source on the surface Σ, and $\mathbf{j}\cdot\mathbf{n}$ is the flux of ρf across the surface Σ. Equating the two expressions for the time rate of change of ρf in the entire region,

$$\int_{\Omega(t)}\left(\rho\frac{Df}{Dt} - \rho Q\right)d\Omega = -\int_{\partial\Omega(t)}\mathbf{j}\cdot\mathbf{n}\,d\Sigma + \int_{\Sigma(t)}\left([\rho f s_n] - g\right)d\Sigma \tag{C.11}$$

Taking the limit as Ω shrinks down to an arbitrary size, leaving only Σ,

$$\lim_{\Omega(t)\to 0}\left\{\int_{\Omega(t)}\rho\left(\frac{Df}{Dt}-Q\right)d\Omega\right\}=0 \tag{C.12}$$

so that

$$0=\int_{\Sigma(t)}\left([\mathbf{j}\cdot\mathbf{n}]-[\rho f s_n]-g\right)d\Sigma \tag{C.13}$$

or

$$[\rho f s_n]=[\mathbf{j}\cdot\mathbf{n}]-g \tag{C.14}$$

This represents the jump in a physical quantity density f across and interface moving at a relative speed s_n. There is a contribution from a surface source (if any), as well as the flux of the quantity through the interface. For a jump mass balance (f=1, g=0) at a phase interface when interfacial effects are ignored,

$$[\rho(\mathbf{j}\cdot\mathbf{n}-s_n)]=0 \tag{C.15}$$

This relates the velocity of a surface of disontinuity to the rate of mass flow, which can be re-written into a kinematic condition for the surface by writing explicitly the form of s_n.

Now the kinematic boundary condition is derived. Let F(**a**, t) represent the surface Σ which separates two imiscible phases α and β. F is not to be confused with the generic quantity F used above. The surface normal is defined in the usual way,

$$\mathbf{n}\equiv\frac{\nabla F}{|\nabla F|} \tag{C.16}$$

For any point $\mathbf{a}\in\Sigma$ on the surface the following physical constraints are required:

[1] no mass will pass through the interface Σ.

[2] The two fluids will remain in continuous contact

[3] If both fluids have non-zero viscosity, there is no slip along the surface Σ.

[4] linear momentum is conserved across the interface

Conditions [1] and [2] dictate that at any point **a** on the surface, the component of fluid velocity **v**(**a**,t) normal to the surface F(**a**,t) = 0 must be equal to the velocity of the surface v_n(**a**,t) along the direction **n**(**a**,t), the unit normal to the surface F(**a**,t) = 0 . This is written as:

$$\lim_{\substack{\mathbf{r}\to\mathbf{a} \\ \mathbf{r}\in\Omega_i}} \mathbf{v}^{(i)}(\mathbf{r},t)\cdot\mathbf{n}(\mathbf{r},t) = v_n(\mathbf{a},t) \tag{C.17}$$

for all $\mathbf{a} \in \Sigma$. Now consider the trajectory of a point, $\mathbf{a}_p(t)$ which lies on the surface Σ.

$$F(\mathbf{a}_p(t),t) = 0 \tag{C.18}$$

as the trajectory of the surface. Differentiating,

$$\nabla F\cdot\mathbf{v}(\mathbf{a}_p,t) + \frac{\partial F}{\partial t} = 0 \tag{C.19}$$

where $\mathbf{v}(\mathbf{a}_p,t)$ is simply the velocity of the surface at point "p". The normal component of the velocity of the surface is then:

$$\mathbf{v}(\mathbf{a},t)\cdot\mathbf{n} = \mathbf{v}(\mathbf{a},t)\cdot\frac{\nabla F}{|\nabla F|} \tag{C.20}$$

which is equated with the normal component of the fluid velocity at the interface. The surface normal velocity is: (by substitution in Equation C.19)

$$v_n(\mathbf{a},t) = \frac{-1}{|\nabla F|}\frac{\partial F}{\partial t} \tag{C.21}$$

and from substitution into Equation C.17,

$$\lim_{\substack{\mathbf{r}\to\mathbf{a} \\ \mathbf{r}\in\Omega_i}} \mathbf{v}^{(i)}(\mathbf{r},t)\cdot\nabla F(\mathbf{a},t) = -\frac{\partial F}{\partial t} \tag{C.22}$$

which is known as the kinematic boundary condition.

Appendix D.

A THERMODYNAMIC DERIVATION OF YOUNG AND LAPLACE EQUATIONS USING THE GENERALIZED THEORY OF CAPILLARITY

In this appendix Young's equation, the Neumann triangle relation, and the Laplace equation for the jump in pressure across an interface for surfaces and three-phase lines of arbitrary curvature are derived. Recall that Gibbs' derivation of the Young equations holds only for interfaces of small curvature. In a manner similar to Gibbs, a thermodynamic approach is used to derive an energy relation, and by minimizing the energy functional, the relevant equations are obtained.

Begin with the relation between the bulk internal energy and the surroundings. (the fundamental equation):

$$du^{(\Omega)} = Tds^{(\Omega)} + \sum_i \mu_i \rho_i^{(\Omega)} \tag{D.1}$$

$$dU^{(\Omega)} = TdS^{(\Omega)} - Pd\Omega + \sum_i \mu_i dM_i^{(\Omega)} \tag{D.2}$$

Equation D.1 is the intensive form and Equation D.2 is the extensive form of the equation.

1. Surface energy

The fundamental equation for surfaces can also be formulated. Define the excess energy of a surface separating two phases α and β to be

$$U^{(\Sigma)} = U^{(\Omega)} - U^{(\Omega_\alpha)} - U^{(\Omega_\beta)} \tag{D.3}$$

The internal energy is a function of the surface entropy, area, and chemical constituents. In addition, work can be performed by changing the curvature of the interface, independant of the change in area. The principal radii of curvature are convenient quantities to describe this change. However, they are not differential invariants [280]. Therefore, the invariant quatities J,K are used (mean and Gaussian curvatures).

$$\begin{aligned} J &= \frac{1}{2}(\kappa_1 + \kappa_2) \\ K &= \kappa_1 \kappa_2 \end{aligned} \tag{D.4}$$

The surface internal energy is thus a function of surface entropy, area, chemical potential, and curvature.

$$u^{(\Sigma)} = u^{(\Sigma)}\left[s^{(\Sigma)}, \rho_1^{(\Sigma)}, \rho_2^{(\Sigma)}, \ldots, \rho_r^{(\Sigma)}, J, K\right] \tag{D.5}$$

Curvature potentials can be introduced, usually called the first and second bending moments:

$$C_J = \left(\frac{\partial u^{(\Sigma)}}{\partial J}\right)_{s^{(\Sigma)}, \left\{\rho_i^{(\Sigma)}\right\}, K} \tag{D.6}$$

$$C_K = \left(\frac{\partial u^{(\Sigma)}}{\partial K} \right)_{s^{(\Sigma)}, \left\{ \rho_i^{(\Sigma)} \right\}, J}$$

The differential form of the fundamental equation in intensive and extensive forms are:

$$du^{(\Sigma)} = Tds^{(\Sigma)} + \sum_i \mu_i \rho_i^{(\Sigma)} + C_J dJ + C_K dK \tag{D.7}$$
$$dU^{(\Sigma)} = TdS^{(\Sigma)} + \gamma d\Sigma + \sum_i \mu_i M_i^{(\Sigma)} + C_J dJ + C_K dK$$

where J,K are surface integrals of J,K.

$$J = \iint_{\Sigma} J \, d\Sigma \tag{D.8}$$
$$K = \iint_{\Sigma} K \, d\Sigma$$

and the interfacial energy is defined as:

$$\gamma = \left(\frac{\partial U^{(\Sigma)}}{\partial \Sigma} \right)_{S^{(\Sigma)}, \left\{ M_i^{(\Sigma)} \right\}, J, K} \tag{D.9}$$

Similarly, an expression for the internal energy of a three-phase line can be written. Following the reasoning behind excess surface energy, the excess line internal energy between surface phases α and β is defined as:

$$U^{(\ell)} = U^{(\Sigma)} - U^{(\Sigma_\alpha)} - U^{(\Sigma_\beta)} \tag{D.10}$$

Two quantities are required: the contact angles $\phi_{jj'}$ between surfaces j and j' at a multiphase contact line, and the curvature terms κ_n, κ_g, and τ [280]. The contact angles satisfy

$$\sum_{jj'} \phi_{jj'} = 2\pi \tag{D.11}$$

while the normal and geodesic curvature terms satisfy

$$\kappa_{n1}^2 + \kappa_{g1}^2 = \kappa_{n2}^2 + \kappa_{g2}^2 = \kappa_{n3}^2 + \kappa_{g3}^2 = \kappa^2. \tag{D.12}$$

giving the differential form of the fundamental equation:

$$du^{(\ell)} = Tds^{(\ell)} + \sum_i \mu_i d\rho_i^{(\ell)} + \sum_{(jj')} C_{\phi_{jj'}} d\phi_{jj'} + \sum_{(j)} \left(C_{nj} d\kappa_{nj} + C_{gj} d\kappa_{gj} + C_{\tau j} d\tau_j \right) \tag{D.13}$$

$$dU^{(\ell)} = TdS^{(\ell)} + \sigma d\ell + \sum_i \mu_i M_i^{(\ell)} + \sum_{(jj')} C_{\phi_{jj'}} \Phi_{jj'} + \sum_{(j)} \left(C_{nj} K_{nj} + C_{gj} K_{gj} + C_{\tau j} T_j \right)$$

where $\Phi_{jj'}$, K_{nj}, K_{gj}, and T_j are integral quantities of $\phi_{jj'}$, κ_{nj}, κ_{gj}, and τ_j, respectively, $C_{\theta_{jj'}}$, C_{nj}, C_{gj}, and $C_{\tau j}$ are mechanical potentials analogous to the bending potentials for surfaces, and the line tension is defined as:

$$\sigma = \left(\frac{\partial U^{(\ell)}}{\partial \ell} \right)_{S^{(\ell)}, \left\{ M_i^{(\ell)} \right\}, \Phi_{jj'}, K_{nj}, K_{gj}, T_j} \tag{D.14}$$

Finally, the fundamental equation for points is written:

$$du^{(0)} = Tds^{(0)} + \sum_i \mu_i \rho_i^{(0)} + \sum_{(ll')} C_{\varphi_{ll'}} \varphi_{ll'} \tag{D.15}$$

where $\varphi_{ll'}$ represents the vertex angle between intersecting lines l and l'. This equation is the same in internal and external forms.

The generalized Laplace equation, Neumann triangle relation, and Young equation are now derived. This is a variational problem of equilibrium, and the method of Lagrange multipliers is used:

$$f = u_T - \overline{T}s - \sum_i \overline{\mu}_i \rho_i \tag{D.16}$$

$$\delta I = 0 = \sum_{k=1}^{n_\Omega} \delta \iiint_\Omega f^{(\Omega)} d\Omega + \sum_{k=1}^{n_\Sigma} \delta \iint_\Sigma f^{(\Sigma)} d\Sigma + \sum_{k=1}^{n_\ell} \delta \int_\ell f^{(\ell)} d\ell + \sum_{k=1}^{n_0} \delta f^{(0)}$$

where $\overline{T}$ and $\overline{\mu}$ are constant Lagrange multipliers, and n is the number of distinct bulk phases, dividing surfaces, lines and points. The solution is rather lengthy, and the reader is encouraged to see reference [281] for a full derivation. The condition of mechanical equilibrium for a dividing surface becomes:

$$2J\gamma + 2KC_1 - \nabla_2^2 C_1 - K\nabla_2^* \cdot (\nabla_2 C_2) - \rho^{(A)} \mathbf{n} \cdot \nabla\phi = \Delta P \tag{D.17}$$

Here, the surface gradents are defined as:

$$\nabla_2 = \frac{1}{|\mathbf{e}_u \times \mathbf{e}_v|}\left(\mathbf{e}_v \times \mathbf{n} \frac{\partial}{\partial u} + \mathbf{n} \times \mathbf{e}_u \frac{\partial}{\partial v} \right), \text{ and} \tag{D.18}$$

$$K\nabla_2^* = J\nabla_2 + (\nabla_2 \mathbf{n}) \cdot \nabla_2 .$$

If we assume constant potentials:

$$2J\gamma + 2KC_1 = \Delta P \tag{D.19}$$

and neglect curvature, this reduces to the classical Laplace equation:

$$2J\gamma = \Delta P. \tag{D.20}$$

The formulation for the contact line at equlibrium is: (generalized Neumann triangle relation)

$$\left(\sigma + \sum_{(jj')} C_{\phi_{jj'}} \phi_{jj'}\right)\kappa = \sum_{j}\left(\gamma^{(j)} + \left(C_{\phi_{jj_1}} - C_{\phi_{jj_2}}\right)\kappa_{nj}\right)\mathbf{n}_j \tag{D.21}$$

Where $\mathbf{n}_j$ is the outwardly pointing normal to the line tangent to the j^{th} surface. We have assumed the line curvature potentials and line tension are constant along the dividing line. The most general form is extremely complex and is available elsewhere [281]. The order of dividing surfaces around the dividing line has been set to be j_1, j and j_2.

Young's equation is derived from Equation D.21. The bulk phases are re-labeled with subscripts $_{(s)}$ for solids, $_{(l)}$ for liquid, and $_{(v)}$ for vapor. Similarly, the dividing surfaces will be labeled $^{(sv)}$, $^{(sl)}$, and $^{(lv)}$. For the dividing line, the equation of equilibrium is:

$$\begin{aligned}&\left(\sigma + \left(C_{\phi l} - C_{\phi v}\right)\phi_l\right)\kappa_{gs} + \left[\gamma^{(lv)} + \left(C_{\phi l} - C_{\phi v}\right)\left(\kappa_{ns}\cos\phi_l - \kappa_{gs}\sin\phi_l\right)\right]\cos\phi_l = \\ &\gamma^{(sv)} - \gamma^{(sl)} + \left(C_{\phi l} - C_{\phi v}\right)\kappa_{ns}\end{aligned} \tag{D.22}$$

Which can be further approximated by neglecting the curvature potentials:

$$\begin{aligned}&\sum_{j}\gamma^{(j)}\mathbf{n}_j - \sigma\kappa = 0 \\ &\gamma^{(sv)} - \gamma^{(sl)} - \gamma^{(lv)}\cos\phi_l + \sigma\kappa_{gs} = 0\end{aligned} \tag{D.23}$$

Which are the classical Neumann triangle and classical Young's equation, with a line tension term added. It should be noted that the simplifying assumptions recover the classical Laplace equation but not the classical Young equation.

Appendix E.

EXPLICIT DERIVATION OF THE NORMAL PRESSURE BALANCE ACROSS AN INTERFACE

Normally, this is just presented and left as an exercise to the reader. Here is an explicit derivation. In this appendix, for clarity, the "comma" signifier is omitted, and the presence of a subscript will indicate partial differentiation with respect to the subscripted variable. The equation of the liquid bridge surface is defined in the following form:

$$F = r - f(\theta, z, t) \tag{E.1}$$

where f represents the deviation of the surface from a cylinder of radius R. An expression for the normal pressure balance, which is related to the curvature of the surface: $\Delta p = 2J\gamma$, where J is the mean curvature and γ is the interfacial energy is to be derived. the mean curvature is related to the surface normal, expressed in cylindrical coordinates:

$$2J = \nabla \cdot \mathbf{n} = \frac{1}{r}\frac{\partial}{\partial r}(rn_r) + \frac{1}{r}\frac{\partial}{\partial \theta}(n_\theta) + \frac{\partial}{\partial z}(n_z) \tag{E.2}$$

where the divergence is expressed in cylindrical coordinates (r,θ,z). The normal is the normed gradient of the surface, also expressed in cylindrical coordinates:

$$\mathbf{n} = \frac{\nabla F}{|\nabla F|} = \frac{\frac{\partial F}{\partial r}\mathbf{e}_r + \frac{\partial F}{\partial z}\mathbf{e}_z + \frac{1}{r}\frac{\partial F}{\partial \theta}\mathbf{e}_\theta}{\left[\left(\frac{\partial F}{\partial r}\right)^2 + \left(\frac{\partial F}{\partial z}\right)^2 + \left(\frac{1}{r}\frac{\partial F}{\partial \theta}\right)^2\right]^{1/2}} \tag{E.3}$$

$$= \frac{\mathbf{e}_r - f_z\mathbf{e}_z - \frac{1}{r}f_\theta\mathbf{e}_\theta}{\left[1 + f_z^2 + \left(\frac{f_\theta}{r}\right)^2\right]^{1/2}} = \frac{r\mathbf{e}_r - rf_z\mathbf{e}_z - f_\theta\mathbf{e}_\theta}{\left[r^2 + r^2f_z^2 + f_\theta{}^2\right]^{1/2}}$$

and thus the curvature can be expressly written as the following:

$$\frac{1}{r}\frac{\partial}{\partial r}(rn_r) = \frac{1}{r}\left[\frac{\left[r^2 + r^2f_z^2 + f_\theta{}^2\right]^{1/2} \cdot 2r - r^3\left(1 + f_z^2\right)\left[r^2 + r^2f_z^2 + f_\theta{}^2\right]^{-1/2}}{\left[r^2 + r^2f_z^2 + f_\theta{}^2\right]}\right] \tag{E.4}$$

$$= \frac{1}{r}\left[\frac{2r}{\left[r^2 + r^2f_z^2 + f_\theta{}^2\right]^{1/2}} - \frac{r^3\left(1 + f_z^2\right)}{\left[r^2 + r^2f_z^2 + f_\theta{}^2\right]^{3/2}}\right]$$

$$\frac{1}{r}\frac{\partial}{\partial \theta}\left(n_\theta\right) = \frac{1}{r}\left[\frac{\left[r^2 + r^2f_z^2 + f_\theta{}^2\right]^{1/2} \cdot f_{\theta\theta} - f_\theta\left(r^2f_zf_{z\theta} + f_\theta f_{\theta\theta}\right)\left[r^2 + r^2f_z^2 + f_\theta{}^2\right]^{-1/2}}{\left[r^2 + r^2f_z^2 + f_\theta{}^2\right]}\right] \tag{E.5}$$

$$= \frac{1}{r}\left[\frac{f_{\theta\theta}}{\left[r^2 + r^2f_z^2 + f_\theta{}^2\right]^{1/2}} - \frac{r^2f_\theta f_zf_{z\theta} + f_\theta^2 f_{\theta\theta}}{\left[r^2 + r^2f_z^2 + f_\theta{}^2\right]^{3/2}}\right]$$

$$\frac{\partial}{\partial z}(n_z) = \left[\frac{\left[r^2 + r^2f_z^2 + f_\theta{}^2\right]^{1/2} \cdot rf_{zz} - rf_z\left(r^2f_zf_{zz} + f_\theta f_{\theta z}\right)\left[r^2 + r^2f_z^2 + f_\theta{}^2\right]^{-1/2}}{\left[r^2 + r^2f_z^2 + f_\theta{}^2\right]}\right] \tag{E.6}$$

$$= \left[\frac{rf_{zz}}{\left[r^2 + r^2f_z^2 + f_\theta{}^2\right]^{1/2}} - \frac{r^3f_z^2f_{zz} + f_zf_\theta f_{\theta z}}{\left[r^2 + r^2f_z^2 + f_\theta{}^2\right]^{3/2}}\right]$$

$$\nabla\cdot\mathbf{n}=\left[\frac{2-\frac{f_{\theta\theta}}{r}-rf_{zz}}{\left[r^2+r^2f_z^2+f_\theta{}^2\right]^{1/2}}-\frac{r^2\left(1+f_z^2\right)-rf_\theta f_z f_{z\theta}-\frac{f_\theta^2 f_{\theta\theta}}{r}-r^3f_z^2f_{zz}-rf_z f_\theta f_{\theta z}}{\left[r^2+r^2f_z^2+f_\theta{}^2\right]^{3/2}}\right] \tag{E.7}$$

$$=\frac{1}{\left[r^2+r^2f_z^2+f_\theta{}^2\right]^{3/2}}\left[\begin{array}{l}2r^2\left(1+f_z^2\right)+2f_\theta^2-rf_{\theta\theta}\left(1+f_z^2\right)-\frac{f_\theta^2f_{\theta\theta}}{r}-r^3\left(1+f_z^2\right)f_{zz}-rf_\theta^2f_{zz}\\-r^2\left(1+f_z^2\right)+rf_\theta f_z f_{z\theta}+\frac{f_\theta^2f_{\theta\theta}}{r}+r^3f_z^2f_{zz}+rf_z f_\theta f_{\theta z}\end{array}\right]$$

$$=\left[\frac{r\left(1+f_z^2\right)\left(r-f_{\theta\theta}\right)-rf_{zz}\left(r^2+f_\theta^2\right)+2f_\theta\left(f_\theta+rf_z f_{z\theta}\right)}{\left[r^2+r^2f_z^2+f_\theta{}^2\right]^{3/2}}\right]$$

which is in agreement with [62,68,118]. This can be simplified in the case of axisymmetric bridges to :

$$\nabla\cdot\mathbf{n}=\left[\frac{r^2\left(1+f_z^2\right)-r^3f_{zz}}{\left[r^2\left(1+f_z^2\right)\right]^{3/2}}\right] \tag{E.8}$$

REFERENCES

[1] Orr, F. M., Scriven, L. E. and Rivas, A. P., Pendular rings between solids: meniscus properties and capillary force, *J. Fluid Mech.* **67**, 1975, 723 -742.

[2] Haines, W. B., A note on the cohesion developed by capillary forces in an ideal soil, *J. Agric. Sci.* **15**, 1925, 529-543.

[3] Morrow, N. R., The retention of connate water in hydrocarbon reservoirs, *J. Can. Pet. Tech.* **10**, 1971, 38-46.

[4] Defay, R. and Prigogine, I., *Surface Tension and Absorption,* Wiley, New York, 1966.

[5] Everett, D. H., *The Solid- Gas Interface*, vol. 2, E. A. Flood, ed., Dekker, New York, 1967.

[6] Heady, R. B. and Cahn, J. W., An analysis of the capillary forces in liquid-phase sintering of spherical particles, *Met. Trans.* **1**, 1970, 185-189.

[7] Carmen, P.C., Properties of capillary held liquids *J. Phys. Chem.* **57**, 1953, 56.

[8] Haines, W. B., Studies of the physical properties of soils *J. Agric. Sci.* **17**, 1927, 264-290.

[9] Fisher, R. A., On the capillary forces in an ideal soil; correction of formulae given by W. B. Haines, *J. Agric. Sci.* **16**, 1926, 492-505.

[10] Zimon, A. D., *Adhesion of Dust and Powder* Plenum, New York, 1969.

[11] Langbein, D., *J. Phys. Condens. Matter* **2**, 1990, SA491-SA498. see also ref. [22].

[12] Coriell, S. R., Hardy, S. C. and Cordes, M. R., Stability of liquid zones, *J. Colloid Interface Sci.* **60**, 1977, 126-136.

[13] Chun, C. H., Experiments on steady and oscillatory temperature distribution in a floating zone due to the Marangoni convection, *Acta Astronautica* **7**, 1980, 479-488.

[14] Langbein, D., Crystal growth from liquid columns, *J. Crystal Growth* **104**, 1990, 47-59.

[15] Tsamopolous, J., Chen, T. and Borkar, A., Viscous oscillations of capillary bridges, *J. Fluid Mech.* **235**, 1992, 579-609.

[16] Ennis, B. J., Li, J., Tardos, G. and Pfeffer, R., The influence of viscosity on the strength of an axially strained pendular bridge, *Chem. Eng. Sci.* **45**, 1990, 3071-3088.

[17] George, R. B. *et al.*, in *Chest Medicine. Essentials of Pulmonary and Critical Care Medicine*, Williams and Wilkins, Baltimore,1990.

[18] Johnson, M. *et al.*, The nonlinear growth of surface-tension-driven instabilities in a thin annular film, *J. Fluid Mech.* **233**, 1991, 141-156.

[19] Newhouse, L. A. and Pozrikidis, C., The capillary instability of annular layers and thin liquid threads, *J. Fluid Mech.* **242**, 1992, 193-209.

[20] Slobozhanin, L. A. and Tyuptsov, A. D., Stable equilibrium of the surface of a capillary liquid in contact with the edge of a solid, *Izv. Akad. Nauk SSSR. Mekh. Zhid. Gaza* **1**, 1974, 3-6 (in Russian). English translation: *Fluid Dynam.* **9**(1), 1974, 1.

[21] Dyson, D. C., Contact line stability at edges: Comments on Gibbs' inequalities, *Phys. Fluids* **31**, 1988, 229-232.

[22] Martinez, I. M., Haynes, J. M. and Langbein, D., Fluid statics and capillarity, in *Fluid Sciences and Material Sciences in Space*, H. Walter, ed. Springer Verlag, Berlin, 1987, 53-80.

[23] Haynes, J. M., Capillarity and wetting, in *Materials Science in Space*, B. Feuerbacher, H. Hamacher, R. J. Naumann, eds. Springer Verlag, Berlin, 1987, 129-147.

[24] Steen, P. H. and Lowry, B. J., Flow induced stabilization of liquid columns in a dynamic Plateau chamber, *AIAA* paper no. 93-0255, 1993.

[25] Vogel, T. I., Stability of a liquid drop trapped between two parallel plates, *SIAM J. Appl. Math.* **49**, 1987, 516-525.

[26] Vogel, T. I., Stability of a liquid drop trapped between two parallel plates II: General contact angles, *SIAM J. Appl. Math.* **49**, 1989, 1009-1028.

[27] Langbein, D., Stability of liquid bridges between parallel plates, *Microgr. Sci. Technol.* **V**, 1992, 2-11.

[28] Capodano, P., On the small oscillations of a catenoidal liquid bridge between two parallel plates under zero gravity, *Microgr. Sci. Technol.* **VII**, 1994, 252-257.

[29] Langbein, D., Oscillations of finite liquid columns, *Microgr. Sci. Technol.* **V**, 1992, 73-85.

[30] Orr, F. M. and Scriven, L. E., Meniscus properties and capillary forces, *J. Fluid Mech.* **67**, 1975, 723-742.

[31] Mehrotra, V. P. and Sastry, K. V. S., Pendular bond strength between unequal-sized spherical particles, *Powder Tech.* **25**, 1980, 203-214.

[32] Mazzone, D. N., Tardos, G. I. and Pfeffer, R., The behavior of bridges between two relatively moving particles, *Powder Tech.* **51**, 1987, 71-83.

[33] De Bisschop, F. R. E., Rigole, W. J. L., A physical model for liquid capillary bridges between adsorptive solid spheres: The nodoid of Plateau, *J. Colloid Interface Sci.* **88**, 1982, 117-128.

[34] Abbe, E., Beitrage zur Theorie des Mikroskops und der mikroskopischen Wahrnehmung, *Archiv. Mikroskopische Anat.* **9**, 1873, 413-468.

[35] Porter, A. B., On the Diffraction Theory of Microscopic Vision, *Phil. Mag.* **11**, (6), 1906, 154-166.

[36] Maréchal, A. and Croce, P., Un filtre des fréquences spatiales pour l'amélioration du contraste des images optiques, *Comptes Rendus* **237**, 1953, 607 609.

[37] Marquet, M., Détramage de clichés par filtrage optique, *Optica Acta* **6**, 1959, 404-405.

[38] Duffieux, P. M., *L'Intégrale de Fourier et sees Applications à L'Optique*, Faculté des Sciences, Besançon, 1946.

[39] Elias, P., Optics and Communication Theory, *J. Opt. Soc. Am.* **43** (4), 1953, 229-232.

[40] Linfoot, E. H., Information Theory and Optical Images, *J. Opt. Soc. Am.* **45** (10), 1955, 808-819.

[41] Elias, P., Grey, D. S. and Robinson, D. Z., Fourier Treatment of Optical Processes, *J. Opt. Soc. Am.* **42** (2), 1952, 127-134.

[42] Rhodes, W. T., Simple procedure for the analysis of coherent imaging systems, *Opt. Let.* **19** (19), 1994, 1559-1561.

[43] Cutrona, L. J., Leith, E. N., Palermo, C. J. and Porcello, L. J., Optical Data Processing and Filtering Systems, *IRE Trans. Infor. Th.* Vol. IT-**6** (3), 1960, 386-400.

[44] O'Neill, E. L., Spatial Filtering in Optics, *IRE Trans. Infor. Th.* Vol. IT-2, 1956, 56-65.

[45] Turin, G. L., An Introduction to Matched Filters, *IEEE Trans. Infor. Th.* Vol. IT-**6** (2), 1960, 311-329.

[46] Vander Lugt, A., Signal Detection by Complex Spatial Filtering, *IEEE Trans. Infor. Th.* Vol. IT-10, 1964, 139-145.

[47] Tsuiuchi, J., Restitution des images aberrantes par le filtrage des fréquences spatiales, *Optica Acta* **7** (3), 1960, 243-261.

[48] Cutrona, L. J., Optical computing techniques, *IEEE Spectrum*, **1**, (10), 1964, 101-108.

[49] Flannery, D. L. and Horner, J. L., Fourier Optical Signal Processors, *Proc. of the IEEE*, **77**, (10), 1989, 1511-1527.

[50] Lowry, B. J. and Steen, P., On the density matching of liquids using Plateau's method, AIAA paper no. 94-0832, 32nd Aerospace Sciences Meeting, January 10-13, Reno NV, 1994.

[51] Mason, G. C., An experimental determination of the stable length of cylindrical liquid bubbles, *J. Colloid Interface Sci.* **32**,1970, 172-176.

[52] Sanz, A. and Martínez, I., Minimum volume for a liquid bridge between equal disks, *J. Colloid Interface Sci.* **93**, 1983, 235-240

[53] Meseguer, J. and Sanz, A., Numerical and experimental study of the dynamics of axisymmetric liquid bridges, *J. Fluid Mech.* **153**, 1985, 83-101.

[54] Meseguer, J., Mayo, L. A., Llorente, J. C. and Fernández, A., Experiments with liquid bridges in simulated microgravity, *J. Crystal Growth* **73**, 1985, 609-621.

[55] Bezdenejnykh, N. A. and Meseguer, J., Stability limits of minimum volume and breaking of axisymmetric liquid bridges between equal disks. *Presented at the International Symposium on Hydromechanics and Heat/Mass Transfer in Microgravity*, Perm, 1991.

[56] Gonzalez, H., McCluskey, F. M. J., Castellanos, A. and Barrero, A., Stabilization of dielectric liquid bridges by electric fields in the absence of gravity, *J. Fluid Mech.* **206**, 1989, 545-561.

[57] Carruthers, J. R. and Grasso, M., Studies of floating liquid zones in simulated zero gravity, *J. Appl. Phys.* **43**, 1972, 436-445.

[58] Carruthers, J. R., Gibson, E. G., Klett, M. G. and Facemire, B. R., Studies of rotating liquid floating zones on Skylab IV, *AIAA Paper No.* 75-692 (1975).

[59] Carruthers, J. R., Gibson, E. G., Klett, M. G. and Facemire, B. R., Studies of rotating liquid floating zones on Skylab IV, *Progress in Astronautics and Aeronautics* **52**, 1977, 207-221.

[60] Elagin, M. P., Lebedev, A. P. and Tsmelev, A. V., Laboratory modeling of the stability and dynamics of free liquid zones, in *Hydromechanics and Heat and Mass Transfer in Zero-Gravity* (in Russian), Mauka, Moscow, 1982, 24-33.

[61] Sanz, A., The influence of the outer bath on the dynamics of axisymmetric liquid bridges, *J. Fluid Mech.* **156**, 1985, 101-140.

[62] Sanz, A. and López-Díez, J., Non-axisymmetric oscillations of liquid bridges, *J. Fluid Mech.* **205**, 1989, 503-521.

[63] Meseguer, J., Sanz, A. and López, J., Liquid bridge breakages aboard Spacelab-D1, *J. Crystal Growth* **78**, 1986, 325-334.

[64] Martínez, I., Liquid column stability, in *Material Sciences under Microgravity*, ESA SP-222, 1984, 31-36.

[65] Martínez, I., Stability of long liquid columns in spacelab-D1, in *Material Sciences under Microgravity* ESA SP-256, 1987, 235-240.

[66] Martínez, I. and Meseguer, J., Floating liquid zones in microgravity, in *Scientific Results of the German Spacelab Mission D1*, 1987, 105-112, DFVLR.

[67] Martínez, I. and Sanz, A., Long liquid bridges aboard sounding rockets, *ESA Journal* **9**,1985, 323-328.

[68] Sanz, A. and Perales, J. M., Liquid bridge formation, *Appl. Microgravity Tech.* **2**, 1989, 133-141.

[69] Sanz, A., Perales, J. M. and Rivas, D., Rotational instability of a long liquid column, ESA-SP Series, 1989, in press.

[70] Martínez, I., Sanz, A., Perales, J. M. and Meseguer, J., Freezing of a liquid column on the Texus-18 sounding rocket flight, *ESA Journal*, **12**, 1988, 483-489.

[71] Haynes, J. M., Stability of a fluid cylinder, *J. Colloid Interface Sci.* **32**, 1970, 652-654.

[72] Da Riva, I., Stability of liquid bridges, in *Applications of Space Technology*, Pergamon Press, 1981, 69-80.

[73] Meseguer, J., Stability of slender, axisymmetric liquid bridges between unequal disks, *J. Crystal Growth* **67**, 1984, 141-143.

[74] Ungar, L. H. and Brown, R. A., The dependence of the shape and stability of captive rotating drops on multiple parameters, *Phil. Trans. R. Soc. Lond. A* **306**, 1982, 347-370.

[75] Gillette, R. D. and Dyson, R. D., Stability of fluid interfaces of revolution between equal solid circular plates, *Chem. Eng. J.* **2**, 1971, 44-54.

[76] Martínez, I., Floating zone. Equilibrium shapes and stability criteria, in *COSPAR Space Research XVIII*, Pergamon Press, 1978, 519-522.

[77] Martínez, I., Hidrostática de la zona flotante, Tesis Doctoral, 1978, Universidad Politécnica de Madrid.

[78] Boucher, E. A. and Evans, M. J. B., Capillary phenomena, Part XII. Properties of fluid bridges between solids in a gravitational field, *J. Colloid Interface Sci.* **75**, 1980, 409-418.

[79] Slobozhanin, L. A., Problems of stability of an equilibrium liquid encountered in space technology research, in *Fluid Mechanics and Heat/and Mass Transfer Under Zero–Gravity*, Nauka, Moscow, 1982, 9-24 (in Russian).

[80] Boucher, E. A. and Jones T. G., Equilibrium and stability characteristics of zero-gravity fluid bridges constrained between equal solid rods, *J. Colloid Interface Sci.* **126**, 1988, 469-481.

[81] Brown, R. A. and Scriven, L. E., The shapes and stability of captive rotating drops, *Phil. Trans. R. Soc. Lond. A* **297**, 1980, 51-79.

[82] Coriell, S. R. and Cordes, M. R., Theory of molten zone shape and stability, *J. Crystal Growth* **42**, 1977, 466-472.

[83] Da Riva, I. and Martínez, I., Floating zone stability, Exp. 1-ES-331, in *Material Sciences in Space*, ESA SP-142, 1979, 67-73.

[84] Martínez, I. and Perales, J. M., Liquid bridge stability, *J. Crystal Growth* **78**, 1986, 369-378.

[85] T. Surek and S. R. Coriell, Shape stability in float zoning of silicon crystals, *J. Crystal Growth* **37**, 1977, 253.

[86] Meseguer, J., Stability of long liquid columns, in *Material Sciences under Microgravity*, ESA SP-222, 1984, 297-300.

[87] Meseguer, J., Sanz, A. and Perales, J. M., Axisymmetric long liquid bridge stability and resonances, *Appl. Microgravity Tech.* **2**, 1990, 186-192.

[88] Perales, J. M., Meseguer, J. and Martínez, I., Minimum volume stability limits for axisymmetric liquid bridges subject to steady axial acceleration, *J. Crystal Growth* **110**, 1991, 855-861.

[89] Perales, J. M., Dinámica de Columnas Líquidas, Tesis Doctoral, 1990, Universidad Politécnica de Madrid.

[90] Gañán, A., Análisis modal de zonas líquidas axilsimétricas confinadas por tensión superficial, Tesis Doctoral, 1989, Universidad de Sevilla.

[91] Boucher, E. and Evans, M. J. B., A liquid-bridge model for the float-zone processing of materials, *J. Chem. Soc., Faraday Trans. 1*, **81**, 2787, 1985,.

[92] Martínez, I., Floating zone under reduced gravity. Axisymmetric equilibrium shapes, in *Material Sciences in Space*, ESA SP-114, 1976, 277-282.

[93] Martínez, I., Stability of axisymmetric liquid bridges, in *Material Sciences under Microgravity*, ESA SP-191, 1983, 267-273.

[94] Erle, M. A., Gillette, R. D. and Dyson, D. C., Stability of interfaces of revolution with constant surface tension. The case of the catenoid, *Chem. Eng. J.* **1**, 1970, 97-109.

[95] Vega, J. M. and Perales, J. M., Almost cylindrical isorotating liquid bridges for small Bond numbers, in *Material Sciences under Microgravity*, ESA SP-191, 1983, 247-252.

[96] Perales, J. M., Non-axisymmetric effects on long liquid bridges, *Acta Astronautica* **8**, 1987, 561-565.

[97] Perales, J. M., Sanz, A. and Rivas, D., Eccentric rotation of a liquid bridge, *Appl. Microgravity Tech.* **2**, 1990, 193-197.

[98] Meseguer, J., The influence of axial microgravity on the breakage of axisymmetric slender liquid bridges, *J. Crystal Growth* **62**, 1983, 577-586.

[99] Meseguer, J., Sanz, A. and Rivas, D., The breaking of axisymmetric non-cylindrical liquid bridges, in *Materials Sciences under Microgravity*, ESA SP-191, 1983, 261-265.

[100] Meseguer, J., The dynamics of axisymmetric slender liquid bridges between unequal discs, *J. Crystal Growth* **73**, 1985, 599-608.

[101] Bauer, H. F., Natural frequencies and stability of circular cylindrical imiscible liquid systems, *Appl. Microgravity Tech.* **2**, 1989, 27-44.

[102] Meseguer, J., Axisymmetric long liquid bridges in a time-dependent microgravity field, *Appl. Microgravity Tech.* **1**, 1988, 136-141.

[103] Meseguer, J., Perales, J. M. and Bezdenejnykh, N. A., Impulsive motion of viscous axisymmetric liquid bridges. *Presented at the International Symposium on Hydromechanics and Heat/Mass Transfer in Microgravity*, Perm, 1991.

[104] Gañán, A. and Barrero, A., Free oscillations of liquid captive drops, *Microgravity Sci. Technol. III*, 1990, 70-86.

[105] Meseguer, J., The breaking of axisymmetric slender liquid bridges, *J. Fluid Mech.* **130**, 1983, 123-151.

[106] Zhang, Y. and Alexander, J. I. D., Sensitivity of liquid bridges subject to axial residual acceleration, *Phys. Fluids A* **2**, 1990, 1966-1974.

[107] Rivas, D. and Meseguer, J., One-dimensional, self-similar solution of the dynamics of axisymmetric slender liquid bridges, *J. Fluid Mech.* **138**, 1984, 417-429.

[108] Da Riva, I. and Meseguer, J., On the structure of the floating zone in melting, *Acta Astronautica* **5**, 1978, 637-653.

[109] Da Riva, I. and Manzano, D. R., Impulsive motions of the floating zone, *Physico Chemical Hydrodynamics* **2**, 1981, 165-176,

[110] Harriot, G. M. and Brown, R. A., Flow in a differentially rotated cylindrical drop at low Reynolds number, *J. Fluid Mech.* **126**, 1983, 269-285.

[111] Harriot. G. M. and Brown, R. A., Flow in a differentially rotated cylindrical drop at moderate Reynolds number, *J. Fluid Mech.* **144**, 1984, 403-418.

[112] Meseguer, J. and Sanz, A., One-dimensional linear analysis of the liquid injection or removal in a liquid bridge, *Acta Astronautica* **15**, 1987, 573-576.

[113] Russo, M. J. and Steen, P. H., Shear stabilization of the capillary breakup of a cylindrical interface, *Phys. Fluids A* **1**, 1989, 1926-1937.

[114] Mollot, D. J., Tsamopolous, J., Chen, T. and Ashgriz, A., Nonlinear dynamics of capillary bridges: Experiments, *J. Fluid Mech.* **255**, 1993, 411-435.

[115] Bezdenejnykh, N. A. and Meseguer, J., Stability limits of minimum volume and breaking of axisymmetric liquid bridges between unequal disks, *Microgravity Sci. and Technol.* IV/4, 1991, 235-239.

[116] Lowry, B. J. and Steen, P., Stabilization of an axisymmetric liquid bridge by viscous flow, *Int. J. Multiphase flow* **20**, 1994, 439-443.

[117] Slobozhanin, L. A., Investigation of hydrostatic problems simulating the zone melting process, *Izv. Akad. Nauk SSSR,* Ser. Fiz. **49**, 652, 1985, (in Russian); English translation: *Bull. Acad. Sci. USSR*, Phys. Ser. **49**, No. 4, 1985.

[118] Slobozhanin, L. A. and Perales, J. M., Stability of liquid bridges between equal disks in a gravity field, *Phys. Fluids A* **5**, 1993, 1305-1314.

[120] Xu, S., Liquid bridges, stability and microgravity experiments analysis, *Microgr. Sci. Technol.* VI, 1993, 176-182.

[120] Chen, H. and Saghir, M. Z., Non-axisymmetric equilibrium shapes of the liquid bridge, *Microgr. Sci. Technol.* VII, 1994, 12.

[121] Alexander, J. I. D, Zhang, Y. and Delafontaine, S. Stability of bridges subject to nonaxial acceleration, to be published, 1995.

[122] Laveron-Simavilla, A. and Perales, J. M., Equilibrium shapes of non-axisymmetric liquid bridges of arbitrary volume in gravitation fields and their potential energy, *Phys. Fluids* **7**, 1994, 1204-1213.

[123] Gañán- Calvo, A.M., Oscillations of liquid captive rotating drops, *J. Fluid Mech.* **226**, 1991, 63-90.

[124] Nicolás, J., Frequency response of axisymmetric liquid bridges to an oscillatory microgravity field, *Microgr. Sci. Technol.* IV, 1991, 188-190.

[125] Meseguer, J. and Perales, J. M., A linear analysis of g-jitter effects on viscous cylindrical bridges, *Phys. Fluids A* **3**, 1991, 2332-2336.

[126] Nicolás, J. Hydrodynamic stability of high viscosity cylindrical liquid bridges, *Phys. Fluids A* **4**, 1992, 1620-1626.

[127] Meseguer, J. Gonzalez, M. A. and Alexander, J. I. D., Dynamic stability of long axisymmetric bridges, *Microgr. Sci. Technol.* VII, 1994, 234-242.

[129] Borkar, A. and Tsamopolous, J., Boundary layer analysis of the dynamics of axisymmetric capillary bridges, *Phys. Fluids A* **3**, 1991, 2866-2874.

[130] Alexander, J. I. D. and Zhang, Y., The sensitivity of a non-isothermal liquid bridge to residual acceleration, in *Microgravity Fluid Mechanics*, H. J. Rath, ed., IUTAM Symposium, Bremen, Germany, 1991.

[130] Chen, T. and Tsamopolous, J., Nonlinear dynamics of capillary bridges: Theory, *J. Fluid Mech.* **255**, 1993, 373-409.

[131] Bauer, H. and Eidel, W., Vibrations of a liquid column under the influence of a steady axial microgravity field, *Microgr. Sci. Technol.* **3**, 1991, 238-245.

[132] Perales, J. M. and Meseguer, J., Theoretical and experimental study of the vibration of axisymmetric liquid bridges, unpublished manuscript, 1992.

[133] Eidel, W., Weak nonlinear oscillations of an inviscid column with anchored free surface under zero gravity, *Microgr. Sci. Technol.* VII, 1994, 6-11.

[134] Shulkes, R. M. S. M., Nonlinear dynamics of liquid columns: A comparative study, *Phys. Fluids A* **5**, 1993, 2121-2130.

[135] Sanz, A., Static and dynamic response of liquid bridges, *Microgr. Sci. Technol. IV*, 1991, 138-139.

[136] Myshkis, A. D., Babskii, V. G, Kopachevskii, N. D. Slobozhanin, L. A. and Tyuptsov, A. D., *Low Gravity Fluid Mechanics,* Springer Verlag, Berlin, 1987.

[137] Strutt, J. W., (Lord Rayleigh) On the capillary phenomenon of jets, *Proc. Roy. Soc.* **29**, 1879, 71-97.

[138] J. Plateau, *Statique Experimentale et Theoretique des Liquides Soumis aux Seules Forces Moleculaires,* Gautier-Villars, Paris, 1873.

[139] W. Howe, Ph.D. Dissertation, Friedrich-Wilhelms Universität zu Berlin, 1887.

[140] R. D. Gillette and D. C. Dyson, Stability of axisymmetric liquid-fluid interfaces towards general disturbances, *Chem. Eng. J.* **3**, 1972, 196–199.

[141] B. J. Lowry and P. H. Steen, Capillary surfaces: stability from families of equilibria with application to the liquid bridge, *Proc. R. Soc. London A* **449**, 1995, 411-439.

[142] M. J. Russo and P. H. Steen, Instability of rotund capillary bridges to general disturbances: experiment and theory, *J. Colloid. Interface Sci.* **113**, 1986, 154–163.

[143] Slobozhanin, L. A., Some problems of equilibrium stability of zero-g liquid bridges, in *Hydromechanics and Heat/Mass Transfer in Microgravity*, Gordon and Breach, New York, 1992, 185.

[144] Brown, R. A. and Scriven, L. E., The shapes and stability of captive rotating drops, *Phil. Trans. R. Soc. London A* **297**, 1980, 51-79.

[145] Samsonov, V. A., Stability and bifurcation of the equilibrium of a liquid-filled solid. *Nauch. Tr. Inst. Mekh.*, MGU **16**, 1971, 3-54 (in Russian).

[146] Tsamopolous, J., Polinski, A. J. and Ryan, M. E., Equilibrium shapes and stability of captive annular menisci, *J. Fluid Mech.* **197**, 1988, 523-549.

[147] Tyuptsov, A. D., Myshkis, A. D. and Slobozhanin, L. A., General solution procedure for problems of small perturbations and bifurcations of equilibrium capillary liquid surfaces, *Microgr. Sci. Technol. VII/1* 1994, 24-30.

[148] Michael, D. H., Meniscus stability, *Ann. Rev. Fluid Mech* **13**, 1981, 189–215.

[149] Heywang, W., Zur stabilität senkrechter Schmelzzonen, *Z. Naturforsch.* **11**, 1956, 238-241.

[150] Resnick, A. and Alexander, J. I. D., unpublished research.

[151] Steen, P. H. Capillary containment and collapse in low gravity, dynamics of fluid bridges and columns, *Proc. 5th Int. Colloq. on Free Boundary Problems*, Montreal, Canada, June, 1990.

[152] Dijkstra, H. A. and Steen, P. H., Thermocapillary stabilization of the capillary breakup of an annular film of liquid, *J. Fluid Mech.* (in press).

[153] Lubyimov, D. and Cherepanov, A. A., Dynamic stabilization of capillary instability of a cylindrical liquid zone, *Int. Symp. on Hydromechanics and Heat Transfer*, (Abstracts), Perm-Moscow, July 1991, 31.

[154] Bezdenejnykh, N. A, personal communication

[155] Higueras, M., Nicolás, J. and Vega, J. M., Linear oscillations of weakly dissipative axisymmetric liquid bridges, *Phys. Fluids A* **6**, 1994, 438-450.

[156] Ahrens, S., Falk, F., Groβbach, R. and Langbein D., Experiments on oscillations of small liquid bridges, *Microgr. Sci. Tech.* VII, 1994, 2-5.

[157] Morse, S. F., Thiessen, D. B. and Marston, P. L., Capillary bridge modes driven with modulated ultrasonic radiation pressure, accepted for publication, *Physics of Fluids*.

[158] Nicolás, J. A. and Vega, J. M., Weakly nonlinear oscillations of nearly inviscid axisymmetric liquid bridges, *J. Fluid Mech.* **328**, 1996, 95 -128.

[159] Fowle, A. A, Wang, C. A. and Strong, P. F., *Experiments on the stability of conical and cylindrical columns at low Bond numbers*, Arthur D. Little Co, 1979

[160] Preziosi, L., Chen, K and Joseph, D. D., Lubricated pipelining,: Stability of core-annular flow, *J. Fluid Mech.* **201**, 1989, 323-356.

[161] Slobozhanin, L. A., On the stability of the cylindrical equilibrium state of a rotating liquid, in *Mathematical Physics and Functional Analysis*, Fiz. Tekh. Inst. Nizk. Temp. Akad. Nauk Ukr. SSR, Kharkov, 1971, Vol. **2**, 169-177 (in Russian).

[162] Hardy, S. and Coriell, S. R., Melt shape in weightless crystal growth, in *NBS Space Processing Research*, NBSIR 74-611, U.S. Department of Commerce, 1974.

[163] Fowle, A. A., Haggarty, J. S., Perron, R. R., Strong, P. F., and Swanson, J. R., Float-zone processing in a weightless environment, NASA CR-2768, Washington, DC, 1976.

[164] Slobozhanin, L. A., Hydrostatic problems arising during simulation of the process of materials purification and growth of single crystal by the floating zone method. Part 3: Equilibrium and stability of zone in gravitational field and the field of centrifugal forces, Preprint 25-84, *Fiz. Tekh. Inst. Nizk. Temp. Akad. Nauk Ukr. SSR*, Kharkov, 1984 (in Russian).

[165] Slobozhanin, L. A. and Alexander, J. I. D., Multiparametric liquid bridge stability problem, presented at the Joint Xth European and VIth Russian Symposium *Physical Sciences in Microgravity*, St. Petersburg, Russia, June 15-20, 1997.

[166] Martínez, I., Perales, J. M. and Gomez, M., Effect of axial and centrifugal forces on the stability of liquid bridges, in *ESA SP-333*, European Space Agency, Paris, 1992, 123.

[167] Svechkareva, M. A. and Slobozhanin, L. A., Stability of a rotating w-49eightless liquid phase in zone melting, *Prikl. Mekh. Tekh. Fiz.*, No. 6, 1992, 47, (in Russian); English translation: *J. Appl. Mech. Tech. Phys.* **33**, 1992, 811-813.

[168] Slobozhanin, L. A. and Perales, J. M., Stability of an isorotating liquid bridge between equal disks under zero-gravity conditions, *Phys. Fluids* **8**, 1996, 2307-2318.

[169] Ramos, A., Gonzáles, H. and Castellanos, A., Experiments on dielectric liquid bridges subjected to axial electric fields, *Phys. Fluids* **6**, 1994, 3206-3208.

[170] Gonzalez, H. and Castellanos, A., The effect of an axial electric field on the stability of a rotating dielectric cylindrical liquid bridge, *Phys. Fluids* **6**, 1994, 2676-2689.

[171] Gonzalez, H. and Castellanos, A., The effect of residual gravity on the stability of liquid columns subjected to electric fields, *J. Fluid Mech.* **249**, 1993, 185-205.

[172] Ramos, A. and Castellanos, A., Shapes and stability of liquid bridges subject to AC electric fields, *J. Electrostat. Soc.* **26**, 1991, 143-156.

[173] Ramos, A. and Castellanos, A., Bifurcation diagrams of axisymmetric liquid bridges subjected to electric fields, *Phys. Fluids* **6**, 1994, 3206-3208.

[174] Gurtin, M. E. and Murdoch, A. I., A continuum theory of elastic material surfaces, *Arch. Rat. Mech. Anal.* **57**, 1975, 291-323.

[175] Gurtin, M. E., Two-phase deformations of elastic solids, *Arch. Rat. Mech. Anal.* **84**, 1983, 1-29.

[176] Neumann, A. W., Contact angles and their temperature dependence: Thermodynamic status, measurement, interpretation and application, *Advances in Colloid and Interface Sci.* **4**, 1974, 105-191.

[177] Girifalco, L. A. and Good, R. J., A theory for the estimation of surface and interfacial energies. I. Derivation and application to interfacial tension, *J. Phys Chem.* **61**, 1957, 904-909.

[178] Girifalco, L. A. and Good, R. J., A theory for the estimation of surface and interfacial energies. III. Estimation of surface energies from contact angle data, *J. Phys Chem.* **64**, 1960, 561-565.

[179] Haye, M. J. and Bruin, C., Molecular dynamics study of the curvature correction to the surface tension, *J. Chem. Phys.* **100**, 1994, 556-559.

[180] Stoneham, A.M., Ramos, M. M. D. and Sutton, A. P. How do they stick together? The statics and dynamics of interfaces, *Phil. Mag. A* **67**, 1993, 797-811.

[181] Gibbs, J. W., *Collected works of J. W. Gibbs*, vol. 1, Yale University press, New Haven, Conn., 1928.

[182] Rusanov, A. I., *The Modern Theory of Capillarity*, F. C. Goodrich and A. I. Rusanov, eds., Akademie-Verlag, East Berlin, 1981.

[183] In *Applied Surface Thermodynamics*, A. W. Neumann and J. K. Spelt, eds., Marcel-Dekker, Inc, New York 1996.

[184] In *Contact angle, Wettability and Adhesion: Festschrift in honor of Professor Robert J. Good*, K. L. Mittal, ed, VSP, Utrecht, the Netherlands, 1993.

[185] Ishida, K., Kinoshita, S. and Mori, Y. H., Surface tensiometer utilizing laser-beam reflection at cylindrical liquid menisci, *Rev. Sci. Instrum.* **64**, 1993, 1324-1329.

[186] Fadda, E., Berenguer, M. and Clarisse, C., Characterization of latent image by surface energy determined by contact angle measurements, *J. Vac. Sci. Tech. B* **13**, 1995, 1055-1057.

[187] Neumann, A. W., Economopoulos, O., Boruvka, L. and Rapacchietta, A. V., Free energy analysis of heterogeneous cylindrical particles at fluid interfaces, *J. Colloid Interface Sci.* **71**, 1979, 293-300.

[188] Egry, I., Lohofer, G., Neuhaus, P, and Saurland, S., Surface tension measurements of liquid metals using levitation, microgravity, and image processing, *Inter. J. of Thermophys.* **13**, 1992, 65-70.

[189] Bayazitoglu, Y., Sathuvalli, U. B. R., Suryanarayana, P. V. R. and Mitchell, G. F., Determination of surface tension from the shape oscillations of an electromagnetically levitated droplet, *Phys. Fluids* **8**, 1996, 370-383.

[190] Bayazitoglu, Y. and Mitchell, G. F., Experiments in acoustic levitation: surface tension measurements of deformed droplets, *J. Thermophys. and Heat Trans.* **9**, 1995, 694-701.

[191] Henderson, D. C. and Micale, F. J., Dynamic surface tension measurement with the drop mass technique, *J. Colloid Interface Sci.* **158**, 1993, 289-294.

[192] Huh, C. and Reed, R. L., A method for estimating interfacial tensions and contact angles from sessile and pendant drop shapes, *J. Colloid Interface Sci.* **91**, 1983, 472-484.

[193] Padday, J. F., Sessile drop profiles: corrected methods for surface tension and spreading coefficients, *Proc. R. Soc. Lond. A.* **330**, 1972, 561-572.

[194] Girault, H. H. J., Schiffrin, D. J. and Smith, B. D. V., The measurement of interfacial tension of pendant drops using a video image profile digitizer, *J. Colloid Interface Sci.* **101**, 1984, 257-266.

[195] Lord Rayleigh, On the tension of water surfaces, clean and contaminated, investigated by the method of ripples, *Phil. Mag. Soc.* **30**, 1890, 386-400.

[196] Coucoulas, L. M. and Dawe, R. A. The calculation of interfacial tension from sessile drops, *J. Colloid Interface Sci.* **103**, 1985, 230-236.

[197] Wilkinson, M. C. and Aronson, M. P., Applicability of the drop-weight method technique to the determination of the surface tensions of liquid metals, J. Chem. Soc., *Faraday Trans. I* **69**, 1973, 474.

[198] Rotenburg, Y., Boruvka, L. and Neumann, A. W., Determination of surface tension and contact angle from the shapes of axisymmetric fluid interfaces, *J. Colloid Interface Sci.* **193**, 1983, 169-183.

[199 Andreas, J. M., Hauser, E. A. and Tucker, W. B., Boundary tension by pendant drops, *Presented at the Fifteenth Colloid Symposium* at Cambridge, Mass, June 9-11, 1938.

[200] Neumann, A. W. and Good, R. J., Techniques of measuring contact angles, in *Surface and Colloid Science*, vol. 2, experimental methods, R. J. Good and R. R. Stromberg, eds., Plenum press, New York, 1979 31-91.

[201] Hung, R. J., Tsao, Y. D., Hong, B. B. and Leslie, F. W., Dynamics of surface tension in microgravity environment, in *Space Commercialization: Platforms and Processing*, F. Shahrokhi, G. Hazelrigg, and R. Bayuzick, eds., vol. 127 of *Progress in Astronautics and Aeronautics*, AIAA, Washington, D. C. 1990

[202] Tsay, R.-Y. and Yan, S.-C., A video-enhanced plate method for simultaneous measurements of surface tension and contact angle, *Rev. Sci. Instrum.* **66**, 1995, 5065-5069.

[203] Anastasiadis, S. H., Gancarz, I. and Koberstein, J. T., Interfacial tension of imiscible polymer blends: temperature and molecular weight dependence, *Macromolecules* **21**, 1988, 2980-2987.

[204] Lu, P, Tcheng, S. C. and Wan, D. C., Surface tension of superfluid helium, *Il Nuovo Cimiento* **16,** 1994, 531-535.

[205] Stoebe, T., Mach, P., Grantz, S. and Huang, C. C., Surface tension of freestanding partially fluorinated liquid-crystal films, *Phys. Rev. E* **53**, 1996, 1662-1665.

[206] Csikor, F., Fodor, Z., Hein, J. and Heitger, J., Interface tension of the electroweak phase transition, *Phys. Lett. B* **357**, 1995, 156-162.

[207] Garoff, S., Chen, Q., Ramé, E. and Willson, K. R., Microscale hydrodynamics near moving contact lines (unpublished manuscript).

[208] Lambooy, P., Phelan, K. C., Haugg, O. and Krausch, G., Dewetting and the liquid-liquid interface, *Phys. Rev. Lett.* **76**, 1996, 1110-1113.

[209] Spaid, M. A. and Homsy, G. M., Stability of Newtonian and viscoelastic dynamic contact lines, *Phys Fluids* **8**, 1996, 460-478.

[210] Finlow, D. E., Kota, P. R. and Bose, A., Investigation of wetting hydrodynamics using numerical simulations, *Phys Fluids* **8**, 1996, 302-309.

[211] Galliccio, S. and Zhang, Y.-C., Driven interfaces in quenched disorder at critical depinning, *Phys. Rev. E* **51**, 1995, 1686-1689

[212] Marsh, J. A., Garoff, S. and Dussan V., E. B., Dynamic contact angles and hydrodynamics near a moving contact line, *Phys. Rev. Lett.* **70**, 1993, 2778-2781.

[213] Fukai, J., Shiiba, Y., Yamamoto, T., Miyatake, O., Poulikakos, D., Megaridis, C. M. and Zhao, Z., Wetting effects on the spreading of a liquid droplet colliding with a flat surface: experiment and modeling, *Phys Fluids* **7**, 1995, 236-247.

[214] Spaid, M. A. and Homsy, G. M., Viscoelastic free surface flows: spin coating and dynamic contact lines, *J. Non-Newtonian Fluid Mech.* **55,** 1994, 249-281.

[215] Weidner, D. E. and Schwartz, L. W., Contact-line motion of shear-thinning liquids, *Phys Fluids* **6**, 1994, 3535-3538.

[216] Dussan V., E. B., Ramé, E. and Garoff, S., On identifying the appropriate boundary conditions at a moving contact line: an experimental investigation, *J. Fluid Mech.* **230**, 1991, 97-116.

[217] Ngan, C. G. and Dussan V., E. B., On the dynamics of liquid spreading on solid surfaces, *J. Fluid Mech.* **209**, 1989, 191-226.

[218] Brøns, M., Topological fluid dynamics of interfacial flows, *Phys Fluids* **6**, 1994, 2730-2737.

[219] Jensen, O. E., Self-similar, surfactant-driven flows, *Phys Fluids* **6**, 1994, 1084-1094.

[220] Brochard-Wyart, F., de Gennes, P.-G., Hervert, H. and Redon, C., Wetting and slippage of polymer melts on semi-ideal surfaces, *Langmuir* **10**, 1994, 1566-1572.

[221] Koplik, J., Banavar, J. R. and Willemsen, J. F., Molecular dynamics of fluid flow at solid surfaces, *Phys Fluids A* **1**, 1989, 781-794.

[222] Koplik, J., Banavar, J. R. and Willemsen, J. F., Molecular dynamics of Poiseuille flow and moving contact lines, *Phys. Rev. Lett.* **60**, 1988, 1282-1285.

[223] Indekeu, J. O., Introduction to wetting phenomena, *Acta Physica Polonica B* **26**, 1995, 1065-1100.

[224] Korb, J.-P., Mailer, L., Cros, F., Xu, S. and Jonas, J., Surface dynamics of liquids in nanopores, *Phys. Rev. Lett.* **77**, 1996, 2312-2315.

[225] Miksis, M. J. and Davis, S. H., Slip over rough and coated surfaces, *J. Fluid Mech.* **273**, 1994, 125-139.

[226] de Gennes, P.-G., Wetting: statics and dynamics, *Rev. Modern Phys.* **57**, 1985, 827-864.

[227] Borgs, C., De Coninck, J., Koteck´y, R. and Zinque, M., Does the roughness of the substrate enhance wetting?, *Phys. Rev. Lett.* **74**, 1995, 2292-2294.

[228] Dussan V., E. B., The moving contact line: the slip boundary condition, *J. Fluid Mech.* **77**, 1976, 665-684.

[229] Dussan V., E. B., On the spreading of liquids on solid surfaces: Static and dynamic contact lines, *Ann. Rev. Fluid Mech.* **11**, 1979, 371-400.

[230] Dussan V., E. B. and Davis, S. H., On the motion of a fluid-fluid interface along a solid surface, *J. Fluid Mech.* **65**, 1974, 71-95.

[231] Hocking, L. M., A moving fluid on a rough surface, *J. Fluid Mech.* **76**, 1976, 801-817.

[232] Huh, C. and Mason, S. G., Effects of surface roughness on wetting, theoretical, *J. Colloid Interface Sci.* **60**, 1977, 11-38.

[233] Aristotle, *On the Heavens* (English translation by W. K. Guthrie), William Heinemann, Ltd., London, 1936.

[234] Galileo Galilei, *Bodies that Stay Atop Water, or Move In It,* 1612, (English translation by S. Drake), University of Chicago Press, Chicago, 1981.

[235] Young,T., An essay on the cohesion of fluids, *Trans. R. Soc. London* **95**, 1805, 65-87.

[236] Dupré, A., *Theorie Mechanique de la Chaleur*, Gauthier-Villars, Paris 1869.

[237] Bangham, D. H. and Razouk, R. I., Adsorption and the wettability of solid surfaces, *Trans. Faraday Soc.* **33**, 1937, 1459-1463.

[238] Fox, H. W. and Zisman, W.A., The spreading of liquids on low-energy surfaces. III. Hydrocarbon surfaces, *J. Colloid Interface Sci.* **7**, 1952, 428-442.

[239] van Oss, C. J., Chaudhury, M. K. and Good, R. J., Monopolar surfaces, *Adv. Colloid Interface. Sci.* **28**, 1987, 35-64.

[240] van Oss, C. J. and Good, R. J., On the mechanism of "hydrophobic" interactions, *J. Dispersion Sci. Technol.* **9**, 1988, 355-362.

[241] van Oss, C. J., Chaudhury, M. K. and Good, R. J., Polar interactions, hydration pressure and membrane fusion in: *Molecular Mechanisms of Membrane Fusion*, S. Ohki, D. Doyle, T. D. Flanagan and S. W. Hui, eds., Plenum Press, New York, 1988,

[242] Freundlich, H., *Colloid and Capillary Chemistry*, Dutton, New York, 1923.

[243] Wenzel, R. N., Resistance of solid surfaces to wetting by water, *Ind. and Eng. Chem.* **28**, 1936, 988-994.

[244] Good, R. J., A thermodynamic derivation of Wenzel's modification of Young's equation for contact angles; together with a theory of hysteresis, *J. Am. Chem. Soc.* **74**, 1953, 5041-5042.

[245] Cassie, A.B.D. , Contact angles, *Discuss. Faraday Soc.* **3**, 1948, 11-16.

[246] Adamson, A. W., *Physical Chemistry of Surfaces*, 5th ed., Wiley and Sons, 1990.

[247] Andreas, J. M., Hauser, E. A. and Tucker, W. B., Boundary tension by pendant drops, *J. Phys. Chem.* **42**, 1938, 1001.

[248] Plateau, J., Experimental and theoretical researches on the figures of equilibrium of a liquid mass withdrawn from the action of gravity. *A. Rep. Board Reg. Smithson. Inst.*, 1863, 207-285.

[249] Riemann, *Werke*, Leipzig, 1892, pp 301-337, 445-454; Weierstrass, *Werke*, Berlin, 1903, **3**, pp 39-52, 219-220, 221-238; Schwarz, *Gesammelte Mathematische Abhandlungen*, Berlin, 1890, **1**.

[250] Douglas, J., Solution to the Problem of Plateau, *Trans. Amer. Math. Soc.* **33**, 1931, 263-321.

[251] Radó, T., The problem of the least area and the problem of Plateau, *Math. Z.* **32**, 1930, 763-796.

[252] Courant, R. Plateau's problem and Dirichlet's principle, *Ann. Math.* **38**, 3, 1937, 679-724.

[253] Osserman, R. *A survey of minimal surfaces*, Dover, 1986.

[254] Wente, H. C., A general existence theorem for surfaces of constant mean curvature, *Math. Z.* **120**, 1971, 149-170.

[255] Steffen, K., Isometric inequalities and the problem of Plateau, *Math. Ann.* **222**, 1976, 97-144.

[256] Wente, H. C., Large solutions to the volume constrained problem, *Arch. Rational Mech. Anal.* **75**, 1980, 59-77.

[257] Ruh, A. E., Asymptotic behavior of non-parametric minimal hypersurfaces, *J. Differential Geom.* **4**, 1970, 509-513.

[258] Kenmotsu, K., Weierstrass formula for surfaces of prescribed mean curvature, *Math. Ann.* **245**, 1979, 89-99.

[259] Hoffman, D. and Osserman, R., The Gauss map of complete surfaces of constant mean curvature in $\Re^3$ and $\Re^4$, *Comment. Math. Helv.* **57**, 1982, 519-531.

[260] Wente, H. C., Counterexample to a conjecture of H. Hopf, *Pacific J. Math.* **121**, 1986, 193-243.

[261] Barbosa, J. L. M. and do Carmo, M., On the size of a stable minimal surface in $\Re^3$, *Amer. J. Math.* **98**, 1976, 515-528.

[262] Brakke, K., *Surface Evolver Manual*, ver. 2.00, The Geometry Center and Susquehanna University, Selinsgrove, PA, 1996

[263] Goodman, J., *Introduction to Fourier Optics*, McGraw-Hill, NY, 1968.

[264] Gaskill, J., *Linear Systems, Fourier Transforms, and Optics*, Wiley, NY, 1978.

[265] Slobozhanin, L. A., Alexander, J. I. D and Resnick, A., Stability of liquid bridges under reduced gravity, presented at the *Proceedings of the Second European Symposium "Fluids in Space"*, A. Viviani, Ed., 1996, 431-439.

[266] Tate, T., On the magnitude of a drop of liquid formed under different circumstances, *Phil. Mag.* **27**, 1864, 176.

[267] Slobozhanin, L. A., Alexander, J. I. D and Resnick, A., Bifurcation of the equilibrium states of a weightless liquid bridge, *Phys. Fluids* **9** (7), 1997, (in press).

[268] Iooss, G. and Joseph, D. D. *Elementary Stability and Bifurcation Theory*, Springer-Verlag, Berlin 1990.

[269] Cunningham, W. J., *Introduction to Nonlinear Analysis*, (McGraw-Hill, New York) 1958, pp. 171-221.

[270] Kuipers, L., Hoogeman, M. S. and Frenken, J. W. M., Jump to contact and neck formation between Pb surfaces and a STM tip, *Surface Science* **340**, 1995, 231-244.

[271] Misner, C. W., Thorne, K. S., and Wheeler, J. A., *Gravitation*, (W. H. Freeman and Company, New York) 1973.

[272] Synge, J. L. and Schild, A., *Tensor Calculus*, (Dover Publications, New York) 1949.

[273] Middleman, S., *Modeling Axisymmetric Flows.* Academic Press, 1995.

[274] Segel, L. A., *Mathematics Applied to Continuum Mechanics*, (Dover Press, New York) 1987.

[275] Chung, T. J., *Introduction to Continuum Mechanics*, UAH Bookstore, 1993.

[276] Rutherford, A., *Vectors, Tensors, and the Basic Equations of Fluid Mechanics*, (Dover Press, New York) 1962.

[277] Green, A. E., and Zerna, W., *Theoretical Elasticity*, (Oxford University Press, Oxford) 1968.

[278] Marsden, J. E., and Hughes, T. J. R., *Mathematical Foundations of Elasticity*, (Prentice-Hall Inc., Englewood, NJ) 1983.

[279] Stokes, G. G., On the theories of the internal friction of fluids in motion, and of the equilibrium and motion of elastic bodies, *Trans. of the Cambridge Phil. Soc.* **8**, 1845, 287-319.

[280] Struik, D., *Lectures on Classical Differential Geometry*, Dover, NY, 1961.

[281] Boruvka, L. and Neumann, A. W., Classical theory of capillarity, *J. Chem. Phys.* **66**, 1977, 5464-5476.